Patterns in and Kinetics of
Phase Separation in Binary Mixtures

A dissertation submitted in partial fulfillment of the requirements for the
degree of Doctor of Philosophy in Natural Sciences,
By

Ebie M. Sam

Max Planck Institute for Polymer Research, Mainz, Germany
And
Johannes Gutenberg University, Mainz, Germany.

December 2010

"To see a world in a grain of sand,
And a heaven in a wild flower,
Hold infinity in the palm of your hand
And eternity in an hour."

from "Auguries of Innocence"
by William Blake

MAX PLANCK INSTITUTE FOR POLYMER RESEARCH • ACKERMANNWEG 10 • 55128 • MAINZ
PHONE +4917662295303 • E - M A I L: E B I E M S A M @ G M A I L . C O M

E B I E M. S A M

EDUCATION

PhD (2010*)
Max Planck Institute for Polymer Research, Mainz, Germany.

MSc (2006)
Cochin University of Science and Technology, India
GPA of **7** out of **10**

BSc (2004)
Bishop Moore College, Mavelikara, Kerala University, India
Percentage of marks : **88.7 %**

Pre Degree (2001)
Bishop Moore College, Mavelikara , Kerala University, India
Percentage of marks : **72.6 %**

S.S.L.C (1999)
Seventh Day Adventists High School, Mavelikara, India
Percentage of marks : **85.2 %**

PHD THESIS TITLE AND ADVISOR

"Patterns in and kinetics of phase separation in binary mixtures", supervised by Dr. Doris Vollmer and Dr. Günter K. Auernhammer in the group of Prof. Hans Jürgen Butt, Max Planck Institute for Polymer Research, Mainz, Germany.

AWARDS

Best Poster Prize for the poster entitled *"Patterns in Phase Separating Binary Mixtures"*, at the 23rd conference of the European Colloid and Interface Society (ECIS) in Antalya, Turkey, September 2009

PUBLICATIONS AND PRESENTATIONS

"Pattern formation in phase separating binary mixtures", to be published,
Ebie M. Sam, Y. Hayase, Guenter K. Auernhammer and Doris Vollmer

"Cooling instability with latent heat effect", to be published,
Yumino Hayase, Ebie M. Sam, Guenter K. Auernhammer, Doris Vollmer

"Oscillations during phase separation of polystyrene/methylcyclohexane mixture under continuous cooling ", in preparation,
Ebie M. Sam, Guenter K. Auernhammer and Doris Vollmer

"Tracer colloids close to an isotropic-nematic domain interface with phase transition-induced solute transport", Colloids and Surfaces A: Physicochem. Eng. Aspects 354 (2010) 298-307,
Beate Ullrich, Guenter K. Auernhammer, Ebie M. Sam and Doris Vollmer

Oral presentation at the 6th Zsigmondy Colloquium, entitled *"Phase Separation Kinetics in PS/methylcyclohexane binary mixture"*, in Chemnitz, March 2010.

Poster presentation at the 23rd ECIS conference entitled *"Patterns in phase separating binary mixtures"* (best poster prize), Antalya, September 2009.

RESEARCH FELLOWSHIPS & SCHOOLS

Attended the 39th IFF Spring School on Soft Matter at Juelich, Germany, March 2008

Selected for Summer Research Fellowship at *Indian Institute of Science (IISc),* Bangalore by the Indian Academy of Sciences, May 2004

Selected by the *Indian Institute of Astrophysics,* to attend the Summer
School in Physics at IIA, Kodaikanal, June 2005

PROJECTS

"The Emergence of Chaos in a Logistic Map", BSc Project, supervised by Dr. Thomas Kuruvilla, Bishop Moore College, Mavelikara

 " EPR Paradox and its Resolution - A Study on some recent works", MSc project, supervised by Prof. M. Sabir, Cochin University

PERSONAL DETAILS

Nationality:	Indian
Date of Birth:	25-03-1983
Sex:	Male
Marital Status:	Single
Languages:	English (fluent in speaking, reading, writing)
	Malayalam (mother tongue)
	Hindi
Hobbies & Interests:	Music, Photography, Nature, Psychology,
	Travel, Conversations, Calligraphy.

INDEX

INTRODUCTION

Both thermodynamics and hydrodynamics have emerged as two important fields in both fundamental and applied physics. They both are quite broad fields in themselves, and they emerge in a wide variety of physical problems. Since it is the study of the exchange of heat, and their mechanisms, thermodynamics finds immense importance in everyday life; from the small scales like determining the workings of the proteins and cells, to the day to day practical needs of running automobiles and washing clothes, to the large scale workings of the Universe itself. Phase separation, which is commonly encountered in our lives, be it the butter formed from the milk, or the formation of clouds, forms an important part of thermodynamics. Intense studies have been going on to understand phase separation better.

Hydrodynamics on the other hand, dealing with the flow of fluids, also forms an important discipline in physics. From the complex mechanism of blood circulation to the flow of rivers, to the large convective motion of air due to gradients in temperature, to the large scale flows found in stars, hydrodynamics exhibits itself virtually at all length scales, similar to thermodynamics.

Due to this vast range of length and time scales accessible to both thermodynamics and hydrodynamics, numerous instances can be found where there is a complex interplay between them. One of the questions this work aims to understand is the kinetics of phase separation in a binary mixture of a polymer mixed in a solvent. Although much work has been done on binary mixtures quenched into the two phase region just below the binodal, studies on the kinetics by continuous temperature ramp is only relatively new. A bulk cell geometry chosen is with a relatively large height: diameter aspect ratio (2:1 or more), so as to minimize the effects of convection, and solely concentrate on the kinetics determined by temperature ramping. Another aim of this work is to understand explicitly the contribution of hydrodynamic instabilities on phase separation and vice versa. To this end, a laterally extended geometry is used which is a flat cell with diameter: height ratio of 14:1. Here we are aiming on explicitly understanding the hydrodynamic effects on phase separation. In this respect a couple of interesting questions arise, such as: 1) Can we have a geometry where the effects of thermodynamics and hydrodynamics are subtly interwoven, yet experimentally demonstrable and 2) Whether the effects of thermodynamics can initiate any hydrodynamic instabilities.

Chapter 1 gives an introduction to phase separation of single and multi-component systems, which serves as a background for the latter chapters. The cases of low molecular systems and polymer systems are described.

Chapter 2 outlines an account of hydrodynamic instabilities. In particular, two cases, the Rayleigh-Bénard and Marangoni instabilities are discussed in detail. This is in view of their importance in the discussion of results obtained in our experiments. Although this account does not involve phase separation effects, it serves as a platform to describe and compare our results.

Chapter 3 describes the experimental setup for the laterally extended geometry, and also discusses about the samples we used. Chapter 4 discusses the results, most notably demonstrating that patterns do emerge in phase separating systems. Furthermore, it is shown that the Rayleigh-Bénard type patterns are not due to classical convection, but rather initiated by the process of phase separation. Theoretical analysis is also done, which substantiate our results.

Typically when phase separation is brought about in a binary mixture by continuously changing the temperature, an interesting phenomenon is observed. The system, instead of fully phase separating just below the transition temperature, proceeds through a series of cycles characterizing material exchange. Chapter 5 gives a description of this oscillating phenomenon, and consequently arguing that such oscillations must exist in a continuously cooled phase separating mixture.

Chapter 6 introduces the experimental setup and the samples we used for this bulk-geometry case. The results are discussed in Chapter 7, where among other questions, we try to find out what determines the period of oscillations in our system. Questions such as, whether oscillations depend on the sample height, composition of the mixture or the applied cooling rate, are examined. The data then leads us to a better understanding of the nature of oscillations. An interesting case is presented, where we ask the question whether oscillations in a system can be suppressed at all.

The final chapter has a summary of the whole work.

Chapter 1

PHASE SEPARATION

The present work focuses on various aspects of kinetics of phase separation in binary (or pseudo-binary) mixtures. An overview of phase separation is a good starting point to understand the later chapters. This chapter outlines the basic concepts of phases, their separation, and the kinetics involved in phase separation etc.

In the realm of physical sciences, a phase can be defined as a region of space where all physical properties of a material are essentially uniform. A simpler definition would be that a phase is a region of material that is chemically uniform and physically distinct. A common example of a single phase would be an ice cube or a glass of water. Though chemically uniform, if we mix the ice cubes with some water, they are still physically distinct, and therefore form two phases. Depending on the state variables such as temperature, pressure, composition etc, the material in question can form a single phase or more phases. Thus one can construct a phase diagram for a material with its relation to the state variables.

Gibbs' Phase Rule:

All phase diagrams can be discussed in terms of a relationship, the phase rule, derived by J.W. Gibbs [1-2]. Let the number of phases in a system be denoted by P. Thus, ice for example is a single phase (P=1). A system of ice cubes in water is a 2 phase system (P=2). Although it is a 2 phase system, it constitutes only one component, i.e., H_2O. A component is defined as a chemically independent constituent of a system. The number of components, C, in a system is the minimum number of independent species necessary to define the composition of all the phases present in the system. Thus a system of ice cubes in water is a one component system (C=1), and a mixture of ethanol and water is a two component system (C=2).

We can define the degrees of freedom, F, as the number of state variables that can be changed independently without disturbing the number of phases in equilibrium. In a single component, single phase system (C=1, P=1), the pressure and temperature may be changed independently without changing the number of phases, so F=2. We say that the system has two degrees of freedom. On the other hand, if two phases are in equilibrium (for example, a liquid and its vapour) in a single component system (C=1, P=2), the temperature (or pressure) can be changed independently, but then this change demands an accompanying change in pressure (or temperature) to preserve the number of phases in equilibrium. Thus the degrees of freedom of the system has fallen to 1.

Gibbs' phase rule relates the degrees of freedom, F, the number of components, C, and the number of phases at equilibrium, P, for a system of any composition, in the following way:

$$F = C - P + 2$$

As an example, for a one component system like pure water, F=1-P+2 = 3-P. When only one phase is present, F=2 and both pressure and temperature can be varied independently without changing the number of phases. In other words, a single phase is represented by an area on a phase diagram. When two phases are in equilibrium, F=1, which implies that pressure is not freely variable if the temperature is set. Thus the equilibrium of two phases is represented by a line on the phase diagram. When three phases are in equilibrium, F=0 and the system is invariant. This special condition can be established only at a definite temperature and pressure that is characteristic of the substance and outside our control. The equilibrium of three phases is therefore represented by a point, the triple point, on the phase diagram.

One can extend the phase rule to a two component system. There, F=4-P. If the temperature (or pressure) is kept constant, then the remaining degrees of freedom is F'=3-P, which has a maximum value of 2. (F' is used instead of F to denote that one degree of freedom has been discarded). One of the two remaining degrees of freedom is the pressure (or temperature) and the composition (as expressed by the volume fraction of one component). A two component system is also called a binary mixture.

Many binary mixtures exist, and a common example would be a mixture of water and alkane. From common experience we know that oil and water dislike each other. In other words, they have poor solubility within each other, under normal conditions. Another two component system would be, for example, a mixture of methanol and hexane. Instead of taking temperature and pressure as variables, one can instead use temperature and composition, keeping the pressure constant to construct a phase diagram for this two component system [Fig. 1.1].
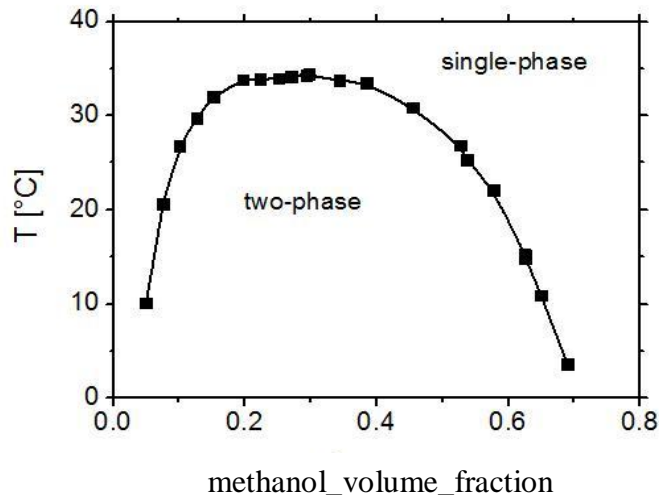

Fig. 1.1
Part of the phase diagram of a two component system; methanol+hexane (figure courtesy: [3]). The chosen degrees of freedom are the composition (given by the volume fraction of methanol), and temperature. The pressure is set constant.

We notice that at temperatures higher than 35°C, the system is in one phase, for any choice of relative compositions. Thus the components are fully miscible in each other. As we decrease the temperature below the line defining the boundary of phase separation, the system starts to phase separate into two phases with different compositions. We also find that the phase boundary (called the binodal curve) is not a straight line, but rather depends on the relative volume fractions of methanol and hexane in the one phase region. Thus for very small volume fractions of methanol or hexane, it is completely soluble in the majority component, and thus no value of temperature can induce a phase separation. As the volume fraction of methanol increases, consequently the temperature at which phase separation occurs also increases, reaching a maximum around 0.35 volume fraction of methanol, and then decreases. This maximum temperature, at which phase separation can occur, is called the critical temperature of the given sample. And the point on the phase diagram corresponding to this temperature and composition is called the critical point. This was a case where the sample phase separated under cooling. There are other two-component samples which can phase separate under heating. An example is a mixture of 2-butoxyethanol (also known as C4E1) and water. Part of the phase diagram of this system is given below [fig 1.2].
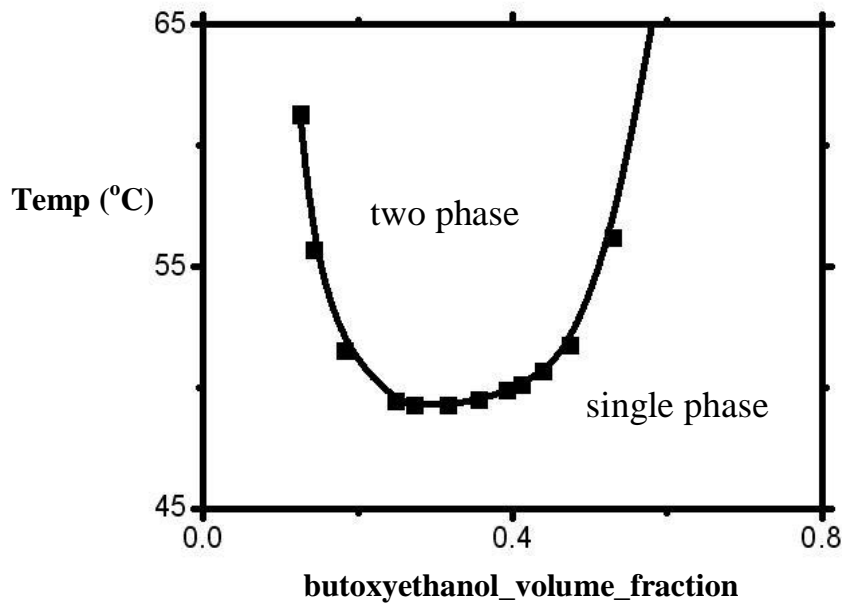

Fig, 1.2
Part of the phase diagram of a two component system; 2-butoxyethanol (C4E1)+water[4]. The chosen degrees of freedom are the composition (given by the volume fraction of butoxyethanol), and temperature.

Here the system remains in a one phase region below 49°C, and phase separation starts as the system is heated past the phase boundary.

Pathways to phase separation

Binary mixtures, can phase separate and form a macroscopic interface between the two final phases. The phase separation can proceed in essentially two different ways. a) Spinodal decomposition and b) Nucleation and growth of droplets.

a) Spinodal decomposition

When a binary mixture has a critical composition, ie, if its composition defines the highest (or lowest) temperature at which it phase separates under cooling (or heating), phase separation proceeds as follows. Any small fluctuations of concentration or density inside the system at the critical temperature are sufficient to grow in its amplitude. Since there is no thermodynamic barrier to the reaction inside of the spinodal region, the decomposition is determined solely by diffusion. Domains, which have a different composition from the equilibrium concentration, are formed spontaneously inside the sample. They then grow and coalesce [5-9].The decomposition proceeds through diffusion, and when the domains become sufficiently big, inertial and gravitational effects also contribute towards the phase separation. This type of phase separation happens in solids too. Extensive quantitative analysis on spinodal decomposition were done by Cahn and Hilliard [10].

In general, spinodal decomposition does not only happen at the critical point. It can take place whenever a system is brought to the so called spinodal region of the phase diagram. A general description can be given as follows, from the following sketch [fig. 1.3]:
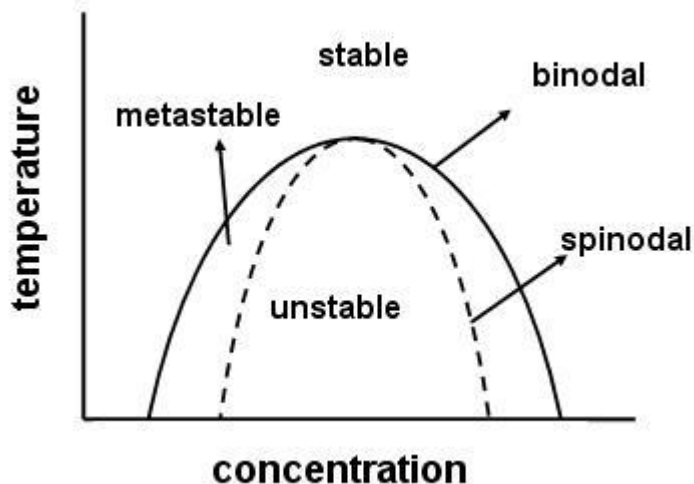

Fig. 1.3
Phase diagram of a two component system showing the binodal and spinodal, which divide the system into regions of different stabilities.

The phase diagram has a binodal line as previously discussed, below which phase separation occurs. Above the line, the system is stable forming a single homogenous phase. There is a also a spinodal line below which the system is unstable. Between the spinodal and the binodal lies a metastable state. At the critical point, the binodal meets the spinodal.

Thus if we can perform an experiment where a system is sufficiently quickly quenched to the spinodal region, spontaneous decomposition occurs for any small fluctuations in concentration with respect to the equilibrium concentration. In other words, even a tiny domain can grow regardless of where we are inside the spinodal region. For experimental easiness, one has the possibility to induce a spinodal decomposition if one prepares a sample with a concentration very close to the critical concentration. This means, a quick small jump in temperature would have a chance to land the system inside the spinodal region. Far away from the critical point, the temperature jump has to be very large and fast, so that it crosses the binodal and lands up in the spinodal region.

b) Nucleation and growth

Suppose there is a shallow temperature quench far away from the critical point. The system enters the metastable binodal region. As the system crosses the binodal, nucleation of droplets starts. But whether these nuclei grow further or die out depends on whether it has attained enough energy for the formation of a stable droplet. If the system is cooled very close to the spinodal, then it required less energy for the nuclei to grow further. Otherwise, the nuclei have to cross a higher energy barrier to form stable droplets of the new phase. Much research has gone into the understanding of nucleation and growth [11-16] and it has been used in modern technology [17-18]

The mechanism of nucleation can be understood as follows. It is energetically favourable for the nuclei to form a volume. On the other hand, a nucleating droplet has to form a surface, which costs energy. A nucleus can be stably formed only when the total energy of forming the volume exceeds that of the cost it has to pay to form the corresponding surface [Fig 1.4].
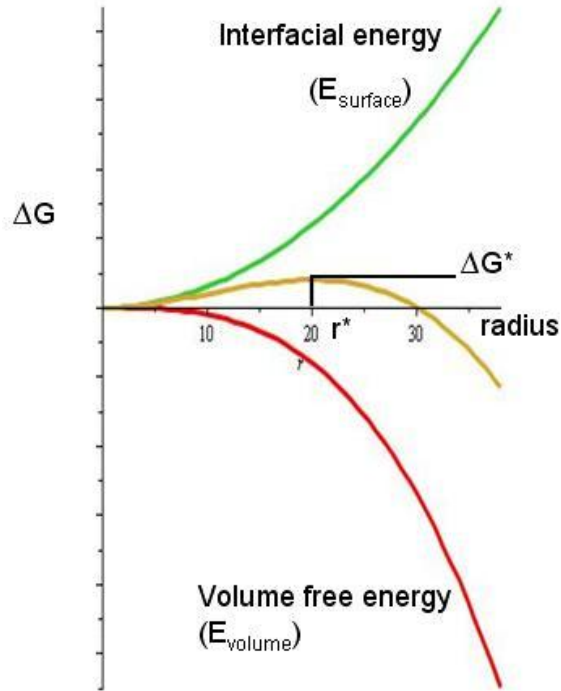
Fig. 1.4

Figure showing the relative strengths of the energies determining the growth of a nucleated droplet. For very small droplets the interfacial energy is higher than the corresponding energy liberated by forming a volume. Thus growth of the droplet is unfavourable. Beyond a critical radius of the droplet, the energy liberated by forming a volume is higher than the cost of forming the corresponding surface, thus favouring its growth

Consider a nucleated droplet with radius R. If Gv is the energy gained by the formation of a unit volume, then the total energy gained by the droplet is given by

$$E_{volume} = -\frac{4}{3}\pi R^3 G_v$$

But there is a cost of energy to form a new surface for this volume, on account of the surface tension. If σ is the energy cost per unit of the new surface, the total energy lost for the droplet is given by:

$$E_{surface} = +4\pi R^2 \sigma$$

The total change in energy is given by the sum of the above two energies,

$$\Delta G = -\frac{4}{3}\pi R^3 G_v + 4\pi R^2 \sigma$$

It can be noticed that for very small values of R, its square is larger than its cubed value, and therefore ΔG would be positive. This implies there should be a net energy cost to form a nucleus, and therefore it is improbable. Such nuclei would redissolve rather than grow [19-20]. For larger values of R, the situation is reversed, and now R^3 would be greater than R^2 and there is net gain of energy. Thus growth of new droplets is favourable. Thus there exists a critical value for the radius, above which the system has a very high probability for growth of droplets. This critical radius can be found from the following condition:

$$\frac{dG}{dR} = 0$$

This condition gives the critical radius R^* as:

$$R^* = \frac{2\sigma}{G_v}$$

Once the nuclear radius passes the critical value, addition of new molecules would release energy rather than cost it. The free energy corresponding to this critical radius is given by:

$$\Delta G^* = \frac{16\pi\sigma^3}{3G_v^{\,2}}$$

Once the nuclei pass this energy barrier, there is a high probability for the growth of the droplet. Their growth would then be hindered only by limitations arising from the kinetics of phase separation.

Phase separation in polymers

Polymer mixtures are model systems for studying fundamental aspects of equilibrium and non-equilibrium properties such as phase diagrams, thermal composition fluctuations in the disordered phase, kinetics of phase separation as well as details of the diffusion process [21-22]

In general, polymeric mixtures are far less miscible than mixtures of small molecule materials. This effect results from the fact that the driving force for mixing is usually entropy, not interaction energy. In other words, miscible materials usually form a solution not because their interaction with each other is more favorable than their self-interaction, but because of an increase in entropy and hence free energy associated with increasing the amount of volume available to each component. This increase in entropy scales with the number of particles (or moles) being mixed. Since polymeric molecules are much larger and hence generally have much higher specific volumes than small molecules, the number of molecules involved in a polymeric mixture is far smaller than the number in a small molecule mixture of equal volume. The solvation of mixing, on the other hand, is comparable on a per volume basis for polymeric and small molecule

mixtures. This tends to increase the free energy of mixing for polymer solutions and thus make solvation less favorable. Thus, concentrated solutions of polymers are far rarer than those of small molecules.

Polymer mixtures commonly exhibit a lower critical solution temperature phase transition, at which phase separation occurs with heating. In solution, the properties of the polymer are characterized by the interaction between the solvent and the polymer. In a good solvent, the polymer appears swollen and occupies a large volume. In this scenario, intermolecular forces between the solvent and monomer subunits dominate over intramolecular interactions. In a bad solvent or poor solvent, intramolecular forces dominate and the chain contracts. In the theta solvent, or the state of the polymer solution where the value of the second virial coefficient becomes 0, the intermolecular polymer-solvent repulsion balances exactly the intramolecular monomer-monomer attraction. Under the theta condition (also called the Flory condition), the polymer behaves like an ideal random coil. The transition between the states is known as a coil-globule transition.

Phase separation in such a polymer solution is more complex than that in polymer blends due to the big disparity between the size of polymer and the solvent molecules [23]. Furthermore there could be unusual effects of polymer-solvent interactions on chain conformation and dynamics. The viscosities of the components also differ significantly and therefore their diffusivities also are quite different. This reflects in the kinetics of phase separation of such a system. The phase diagram is usually asymmetric with regards to the left and right branches. As an example, Fig [1.5] shows phase diagram of a polymer-solvent binary mixture; polystyrene mixed with methylcyclohexane, which phase separates under cooling.
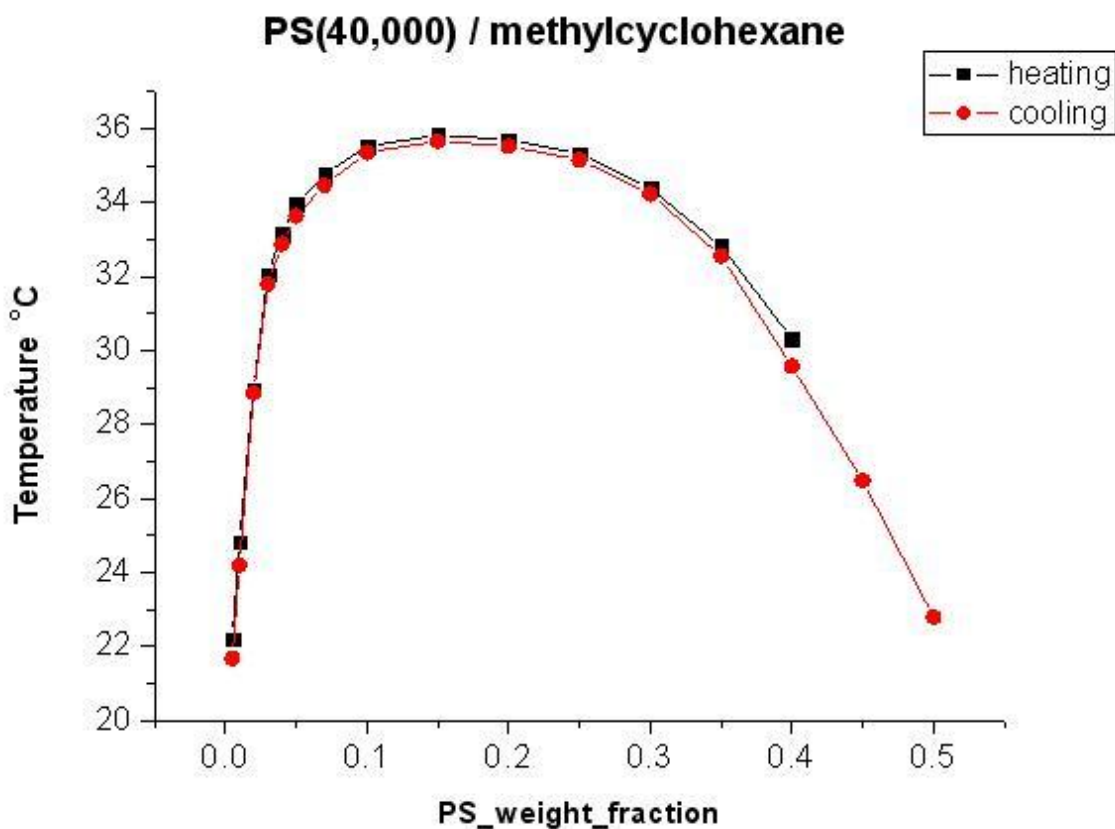
Fig 1.5

Part of the phase diagram of a polymer mixture: polystyrene of molecular weight 40,000g/mol mixed with methylcyclohexane. Squares denote the phase transition temperatures recorded during heating, and circles represent those recorded while cooling.

As seen from the figure, the left branch of the phase diagram is comparatively much steeper than the right branch. Whereas binodal is the theoretical curve on the phase diagram, in experiments the phase transition temperature is measured at the point where the mixtures turns turbid while cooling. This is called the cloud point, and hence the curve is called the cloud point curve. The mixture is heated with stirring, and the temperature at which the solution turns clear is noted down as the phase transition temperature while heating. The average of the heating and cooling curve is taken as the binodal.

Viscoelastic phase separation

Polymer solutions differ from both polymer mixtures and low molecular binary mixtures, in that it consists of components with two strongly pronounced different time- and length-scales of dynamics. In some conventional theories of critical phenomena and phase separation, the same dynamics for the two components of a binary mixture has

been implicitly assumed [24-26] Recent works of Tanaka [27] show that special scenarios may arise when considering dynamically asymmetric systems like polymer solutions. In particular viscoelastic effects can contribute to the kinetics of phase separation.

A viscoelastic substance has an elastic component and a viscous component. The viscosity gives the substance a strain rate dependent on time. Purely elastic materials do not dissipate energy (heat) when a load is applied, then removed. However, a viscoelastic substance loses energy when a load is applied, then removed. Hysteresis is observed in the stress-strain curve, with the area of the loop being equal to the energy lost during the loading cycle. Plastic deformation results in lost energy, which is uncharacteristic of a purely elastic material's reaction to a loading cycle.

Specifically, viscoelasticity is a partly irreversible molecular rearrangement. When a stress is applied to a viscoelastic material such as a polymer, parts of the long polymer chain irreversibly change position.

Viscoelastic effects coming from chain entanglements have so far been believed to be important only in the very early stage where the phase-separation time t is shorter than the characteristic viscoelastic time τ representing the disentanglement time of a chain. It has been widely believed that the topological characteristics of polymer do not cause any essential change in either the critical dynamics or the phase-separation kinetics and they simply slow down the dynamics due to the large viscosity. About 10 years ago, Tanaka showed a different phase separation behavior observed under deep quench in polymer solutions, which are intrinsically dynamic-asymmetric (consisting of long chainlike polymer mixed with simple liquid molecules). It turns out that the interplay between phase-separation dynamics and the slow dynamics of the material itself [28-30] plays an important role in the above type of phase separation. More explicitly, the slow fluid component (polymers) cannot catch up with the deformation rate of phase separation itself and starts to behave like a viscoelastic body. Since viscoelastic effects play a crucial role in this phase separation, it is called 'viscoelastic phase separation'.

A typical example of viscoelastic phase separation in a polymer solution is shown in figure [Fig 1.6]. Just after the temperature quench, the sample becomes cloudy; then after some incubation time (several seconds), small, but macroscopic solvent holes start to appear. This incubation period is called a 'frozen period'. The number and the size of solvent holes increases with time (see figures (b) and (c)). The matrix-polymer-rich phase becomes networklike with the growth of solvent holes. The thin parts of the networklike structure are elongated and eventually broken (see figures 3(d) and 3(e)). In this stage, the pattern is dominated by the elastic force-balance condition. In the final stage the networklike structure relaxes to a structure with a rounded shape and the domain shape starts to be dominated by the interface tension as in usual fluid–fluid phase separation (see figures (e) and (f)). It eventually becomes spherical droplets. During

the period of figures (b)–(e), the volume of the polymer-rich phase keeps decreasing with time and the contrast of that phase becomes more and more pronounced over time, reflecting the increase in the polymer composition of the polymer-rich phase. There occurs a clear phase inversion during phase separation.
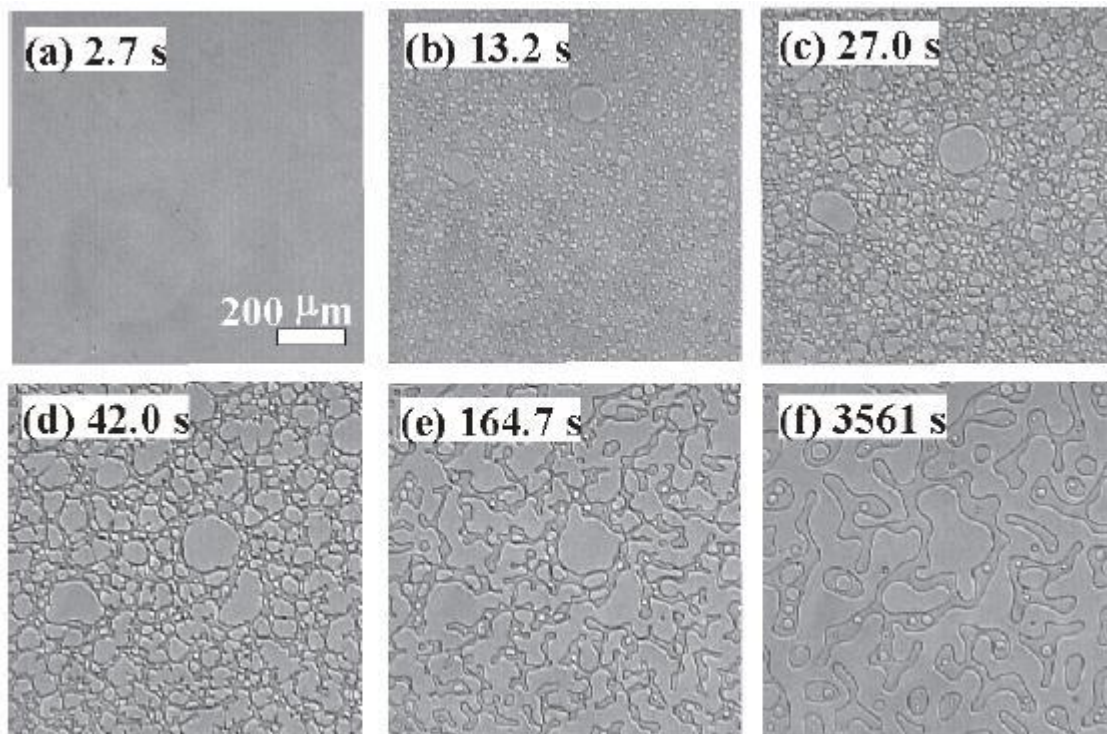
Fig 1.6 . A phase-separation process observed with phase-contrast microscopy in a polymer solution of PS (molecular weight: 3.55×10^5) and diethyl malonate (6.78 wt% PS) at 9.3 ∘C, which is 7.2 K below the phase-separation temperature 16.5 ∘C. The number in each figure indicates a phase-separation time [27].

Chapter 2

HYDRODYNAMIC INSTABILITIES

Hydrodynamic instabilities in various systems have been a focus of research for a long time. In general instability can be defined as the inability of a system to sustain themselves against small perturbations to which it is subject [31]. There are many parameters characterizing a system, such as the temperature, the dimensions of the system, the forces acting on it etc. The stability of the system can be determined by looking at the reaction of the system to small disturbances. Specifically, we look whether the disturbance dies down or the disturbance grows in amplitude in such a way that the system moves further and further away from the initial state. In the first case, we call the system to be stable and in the latter, we call it unstable. Thus it is clear that for a system to be considered stable, it must be stable against all individual disturbances of the parameters governing the system. There exists a threshold value above which the system becomes unstable. Often it is hard to approach these thresholds by the changing parameters such as density or pressure. A nice feature, as we shall see later, is that in most cases these thresholds can be represented just by a number, thus making it a generic feature. A normal method to study the stability or instability of a system would be to continuously change one parameter such as temperature, pressure, density, system dimensions, heat capacity etc while keeping the other parameters constant.

Although we have a wide range of parameters to choose from, in practice changing the temperature or the system dimensions are the easiest to achieve. We could study the stability of a system against temperature variations, for example. In such an experiment, all other parameters other than temperature could be kept constant while temperature could be changed continuously. A classic example of thermal instability is the 'Rayleigh-Bénard' instability [32]. Another example would be the Marangoni instability. Later we would see that in our experiments we encountered both these instabilities. We therefore give an introduction to these instabilities in particular, although other instabilities like Rayleigh-Taylor, Kelvin-Helmholtz, Taylor-Couette etc are found in other experimental setups.

Rayleigh-Bénard instability

Consider a fluid contained between two solid horizontal plates maintained at different temperatures [Fig. 2.1]. Let the temperature of the top plate be T1 and that of bottom plate be T2. We maintain a temperature difference of $\Delta T = T2-T1$, with T2>T1, implying a relatively warmer bottom plate compared to the top.
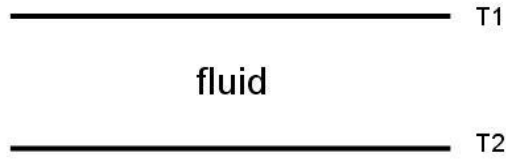
Fig. 2.1

Sketch of a fluid between plates at two temperatures T1 and T2 with T2 > T1

Experimentally, it has been seen that as long as the temperature difference ΔT = T2-T1 is lower than a critical value ΔT_c, the transfer of heat occurs exclusively through conduction. When ΔT reaches the value ΔT_c, incipient motion in the fluid is observed: a system of rolls, alternatively rotating in opposite directions, and of diameter very nearly equal to the distance separating the plates appears simultaneously throughout the cell. A schematic figure is shown below [Fig. 2.2]. Height is assumed to be small relative to the lateral dimensions.
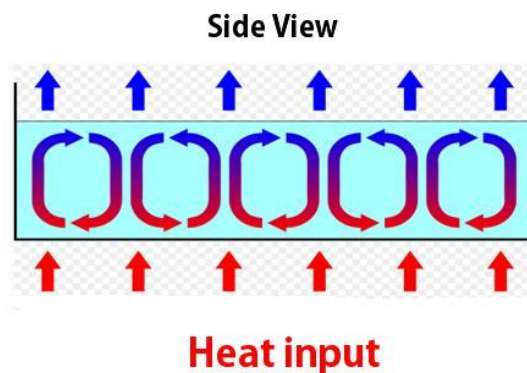
Fig. 2.2

Sketch of convection rolls in a fluid heated from below. Hotter fluid being relatively less dense, moves upwards and subsequently colder fluid is pushed down due to conservation of mass. If there is a continuous heat supply, the process can sustain and the fluid moves in such a rolling fashion. The size of the rolls is comparable to the sample height due to circular motion.

It is also observed that if the temperature difference is sufficiently higher than ΔT_c, other thresholds appear, leading to non-stationary phenomena. This could lead further into turbulent behaviour of the fluid flow.

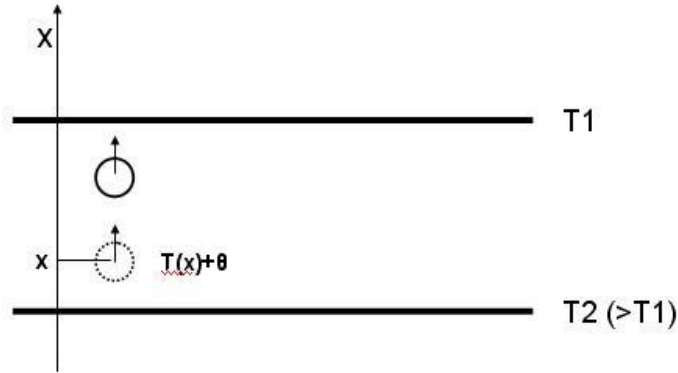The mechanism of the RB instability can be understood as follows [33]. Consider the following figure [Fig. 2.3]

Fig. 2.3

Sketch showing the mechanism of Rayleigh-Bénard instability. The vertical x axis is the spatial dimension, describing the height of the system. Since the upper and lower boundaries are kept at different temperatures, there is a gradient, and thus temperature becomes a function of this spatial dimension. Thus temperature also is depicted on the vertical axis.

Assume that for a small fluid element, the temperature is initially perturbed by a small amount θ relative to its equilibrium value $T(x)$. Vertical motion is then induced on the corresponding elements of fluid as a result of buoyancy. Thus if θ is positive, the local density of the element decreases and it moves upwards. There also results a local convective contribution due to the warmer fluid dragged along by this motion. It originates from warmer, lower layers, and it reinforces the initial temperature perturbation. Unless inhibited by heat conduction and viscous friction, this process becomes self sustaining.

The relevant physical quantities quantifying the mechanisms of heat conduction and viscous friction are thermal diffusivity κ, and kinematic viscosity ν, respectively. The conditions for the onset of instability depend closely on the relative values of the time constants for heat and momentum exchange that govern this situation. An important parameter is the Prandtl number, $\mathrm{Pr} = \dfrac{\nu}{\kappa}$, which characterizes the relative diffusivities of momentum and heat exchange. For most viscous oils, Pr>>1. This means that the velocity perturbations are quickly evened out. We could thus assume that it is the process of reaching thermal equilibrium, for fluids displaced from their normal positions that governs the vertical forces and, consequently, the amplification of the instability.

The physical criterion for the instability can be understood as follows. Consider specifically the motion of a spherical element of fluid of radius R. Assume that as a result of some fluctuation this element acquires a velocity v. Let δT be the temperature difference between this fluid element and its new surroundings. This difference is governed by thermal relaxation time τ_q, between the element and surrounding fluid.

$$\tau_q = A\frac{R^2}{\kappa} \qquad\qquad \text{...(2.1)}$$

Where A is a dimensionless constant. In this time interval, the fluid element has moved through a distance $\delta x = v.\tau_q$. Now the respective differences in density and temperature $\delta\rho_f$ and δT, relative to the surrounding fluid become,

$$\delta T = \delta x.\frac{\partial T}{\partial x} \approx Av\frac{R^2}{\kappa}.\frac{\Delta T}{d} \qquad\qquad \text{..............................(2.2)}$$

{For small temperature gradients $\dfrac{\partial T}{\partial x}$ is assumed to be a constant. So the ratio holds for any finite difference of the variables. Thus $\dfrac{\partial T}{\partial x} = \dfrac{\Delta T}{d}$, where d is the distance between the upper and lower boundaries containing the fluid.}

And

$$\delta\rho_f = -\rho_{f_0}\alpha.\delta T = -A\rho_{f_0}\alpha v.\frac{R^2}{\kappa}.\frac{\Delta T}{d} \qquad \text{..........................(2.3)}$$

where ρ_{f_0} is the density of the fluid and α the thermal expansion coefficient. The minus sign indicates that for an increase in temperature, there is a corresponding decrease in density.

A net driving force (in this case due to buoyancy) acts on the spherical fluid element:

$$F_m = -\frac{4}{3}\pi R^3.\delta\rho_f.g = \frac{4}{3}\pi A\rho_{f_0}\alpha g\frac{R^5}{\kappa}.\frac{\Delta T}{d}.v \qquad \text{.....................(2.4)}$$

The minus sign indicating that the net force is directed upwards. We use the convention of using '+' for forces directed downwards, and '-' for forces directed upwards.

The velocity v of the particle will be increased if this driving force exceeds the Stoke's viscous force, $F_{visc} = -6\pi\eta R v \qquad\qquad \text{..(2.5)}$
The instability criterion thus becomes:

$$|F_m| > |F_{visc}|$$

ie,

$$\frac{4}{3}\pi A\rho_{f_0}\alpha.gv.\frac{R^5}{\kappa}.\frac{\Delta T}{d} > 6\pi\eta R v \qquad \text{..............................(2.6)}$$

Defining $v = \dfrac{\eta}{\rho_{f_0}}$, we have the above condition as:

$$\frac{4}{3}\pi A\alpha g v \frac{R^5}{\kappa}.\frac{\Delta T}{d} > 6\pi v.R.v \qquad\qquad \ldots\ldots\ldots\ldots\ldots\ldots\ldots\ldots....(2.7)$$

Thus we see that the instability is a strongly increasing function of radius of perturbation. Taking the largest possible radius $R = d/2$, we obtain the criterion of instability as:

$$Ra \equiv \frac{\alpha.\Delta T.g d^3}{v.\kappa} > \frac{72}{A} \equiv Ra_c \qquad\qquad \ldots\ldots\ldots\ldots\ldots\ldots\ldots\ldots\ldots.(2.8)$$

where the ratio Ra is called the Rayleigh number. For the instability to be triggered, Ra must exceed a critical value Ra_c .

One can have a more rigorous mathematical analysis of the above problem. It has been found that such an analysis gives the value of Ra_c to be $\sim$ 1700 for the case of a fluid between two flat horizontal plates; $\sim$1100 that for a fluid between a rigid flat horizontal plate and an upper free surface, $\sim$650 that for a fluid whose both boundaries are free.

The beauty of such an analysis is in the fact that the instability can be characterized by the knowledge of a single number, Ra. Thus the problem becomes a system-independent one. In other words such an approach leads to a generic way of understanding the instability. Once the material parameters (α, v, κ), the sample thickness (d), the temperature difference (ΔT) and the boundary conditions are specified, one could calculate the Rayleigh number and predict whether the system is stable or not. Furthermore, the equation tells us that a change in one of the parameters can be compensated by a change in another, so as to again result an instability. It must also be noted that the material parameters can be experimentally determined.

Patterns arising from the instability

In Fig. 2.2 we sketched a convective instability which gives rise to a pattern of rolls alternatively rotating in opposite directions, when viewed from the side. In a 3 dimensional system though, when viewed from the top, how does the pattern look like? It turns out that although the mathematical analysis gives the value of the threshold value for instability, it is silent on the nature of patterns. A further analysis taking into considerations the symmetry of cell patterns suggests that the cell structures could be equilateral triangles, squares, regular hexagons or cylindrical rolls.

The following figure [Fig. 2.4] shows convective cylindrical rolls observed from above in a RB instability experiment carried out in a flat rectangular cell, filled with argon gas under pressure.
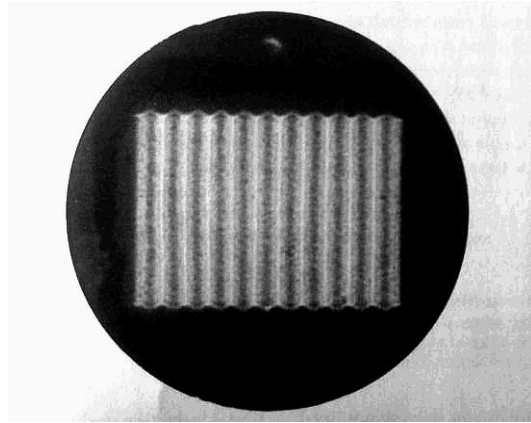
Fig. 2.4
Convective cylindrical rolls in argon gas under pressure, with $\Delta T > 2.\Delta T_c$,
where T_c is the threshold temperature for instability.
{Fig. courtesy: Reference [33], p445}

The following figure [Fig. 2.5] is the result of a molecular dynamics (MD) simulation of RB convection in a fluid. Darker streamlines indicate cooler portions inside the fluid whereas lighter rims forming the edges of the hexagons indicate warmer parts.
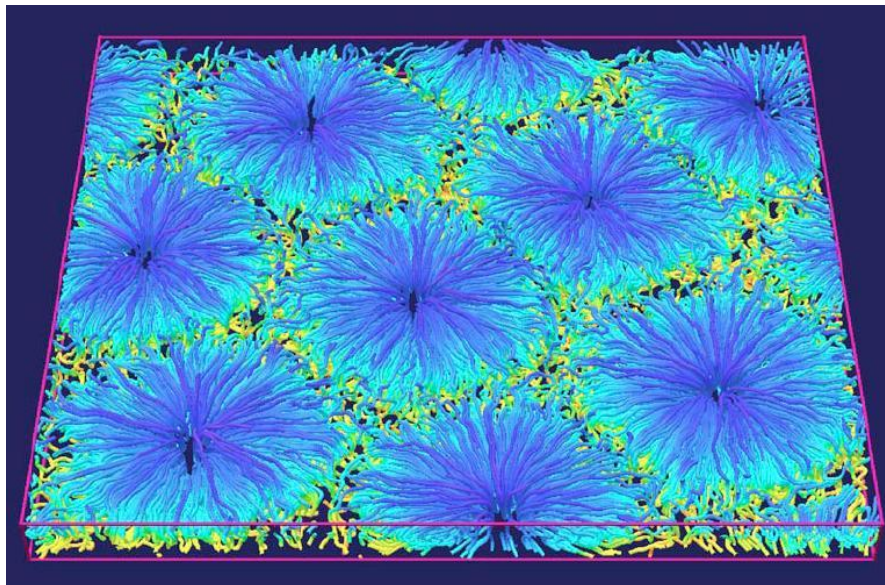

Fig 2.5
Hexagonal patterns in a molecular dynamics simulation of Rayleigh-Bénard instability
{Fig. courtesy: Reference [34]}

The Rayleigh number is defined as in eqn. (2.8)

For a given fluid, the material parameters α, ν, κ remain almost constant for small temperature changes. Thus by changing either the cell thickness d or the temperature difference ΔT, we can reach different values for Ra. A value of Ra just above the threshold value Ra_c starts the instability, whereas higher values of the same denotes the system moving further and further away from stability. Consequently we would expect the nature of patterns also to get affected by the value of Ra.

   The following figure [Fig. 2.6] shows the patterns for different values of Ra at 3 different cell thicknesses, for a single fluid. We see that, for a fixed cell thickness, the nature of patterns change as the Rayleigh number is increased. We see that the instability does not manifest as a unique pattern. The pattern depends also on how near or far the system is from the threshold value of the Rayleigh number. Just above the threshold value, patterns are simple, and they become increasingly complex as the Rayleigh number for the system increases.
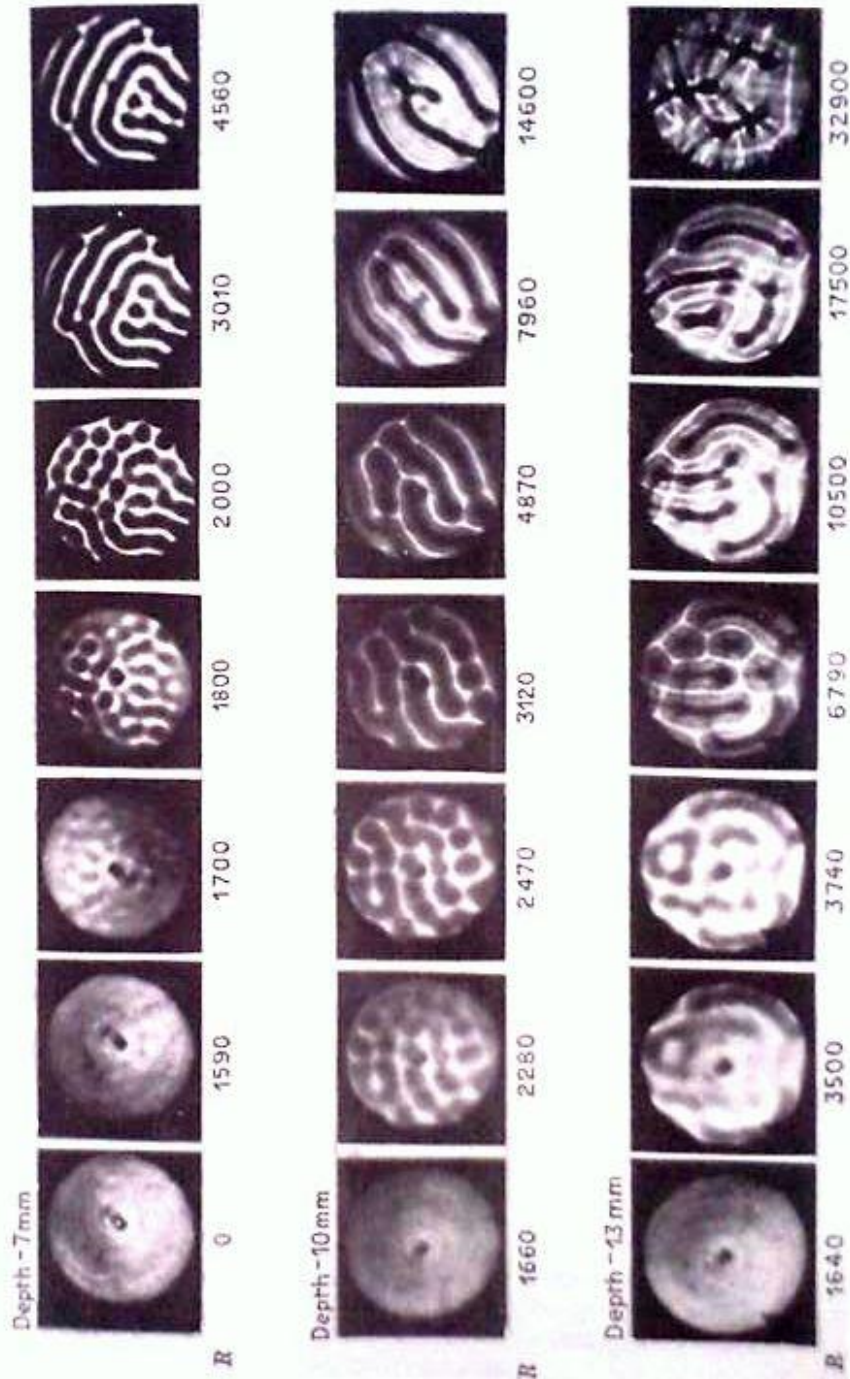
Fig. 2.6
Patterns at different Rayleigh numbers for three different cell depths. Simple patterns appear at the onset of instability, and they get increasingly complex with higher Rayleigh numbers. {Fig. courtesy: Reference [31], p71}

We now go on to a discussion of the Marangoni instability, which also features later in our experiments.

Bénard-Marangoni instability

It is well known that gradients in surface tension on a fluid surface, either due to gradients in temperature or due to concentration, causes fluid motion [33, 35]. The instability known as the Bénard-Marangoni instability (or simply Marangoni instability) occurs upon heating from the bottom of a thin layer of liquid, with a free upper surface. It results from forces induced at the free surface by surface tension gradients. These gradients can create surface stresses and cause fluid motion. The dependence of surface tension on temperature variations can be related in the form

$$\gamma(T) = \gamma(T_0)\{1 - b(T - T_0)\} \ \dots\dots\dots\dots\dots\dots\dots\dots\dots\dots \ (2.9)$$

Where $\gamma(T)$ and $\gamma(T_0)$ are surface tensions of the fluid at temperatures T and T_0, and b is a positive coefficient indicating that the cohesion of liquid decreases with increasing temperature.

A temperature gradient parallel to the surface of a liquid causes a tangential stress on it, as sketched in [Fig. 2.7].
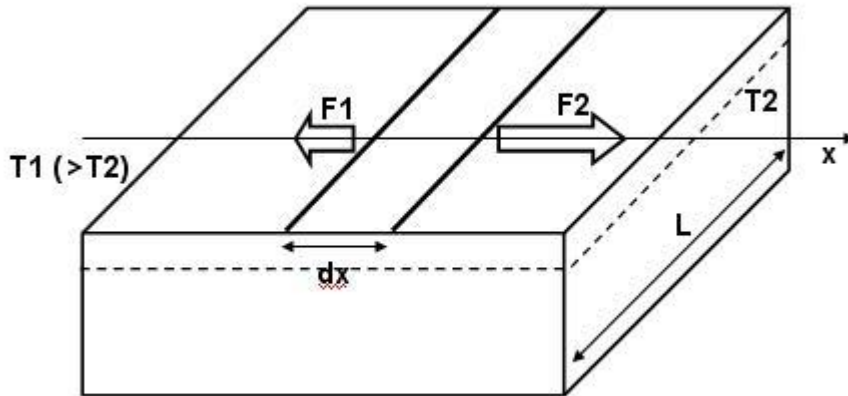
Fig. 2.7
Sketch showing tangential stress on a fluid surface due to temperature gradient

Along a strip of width *dx,* the surface tension forces are no longer in balance. The resultant force is directed towards the regions of lower temperature. Corresponding to a temperature gradient $\dfrac{dT}{dx}$, there is a gradient in surface tension given by

$$\frac{d\gamma}{dx} = \frac{d\gamma}{dT}.\frac{dT}{dx} = -b.\gamma(T_0)(\frac{dT}{dx}) \qquad\qquad \text{..............................} (2.10)$$

This gradient causes a stress $\sigma_{xy}^{(\gamma)}$, in the x direction, on the surface element *L.dx* where

$$\sigma_{xy}^{(\gamma)} = \frac{dF}{L.dx} = \frac{F_2 - F_1}{L.dx} = \frac{(\gamma_2 - \gamma_1).L}{L.dx} = \frac{d\gamma}{dx} = -b.\gamma(T_0)(\frac{dT}{dx}) \qquad \text{......}(2.11)$$

Where F1 and F2 are the forces acting towards the higher and lower temperature areas T1 and T2 respectively,

The negative sign appearing in $\sigma_{xy}^{(\gamma)}$ indicates the fact that the resultant tension acts in the direction where temperature is lower. This stress thus creates a flow parallel to the surface. This onset of fluid motion as a result of surface tension gradients is known as Marangoni effect.

It has been found that above a critical value of temperature difference ΔT_c between the bottom of a fluid layer and the free surface, there appears hexagonal cells of liquid flowing between these two boundaries [Fig. 2.8]. The appearance of these flow cells were visualized by means of a suspension of reflecting particles.
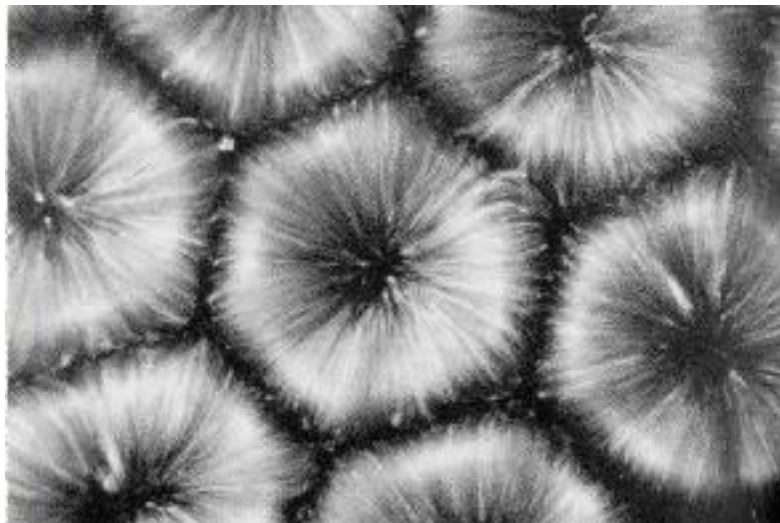

Fig. 2.8
Hexagonal patterns due to Marangoni convection. {Fig. courtesy: reference [33], p460}

The mechanism of the instability can be qualitatively understood as follows. Assume that at a certain given point on the free surface, the temperature rises slightly to a value $(T_1 + \theta)$. Because of the resulting change in surface tension, the fluid is driven radially from this warmer region to the outside. [Fig. 2.9]. Mass conservation then requires that more warm fluid from lower regions of the cell rises upwards, resulting in an increased perturbation because of further local addition of heat.
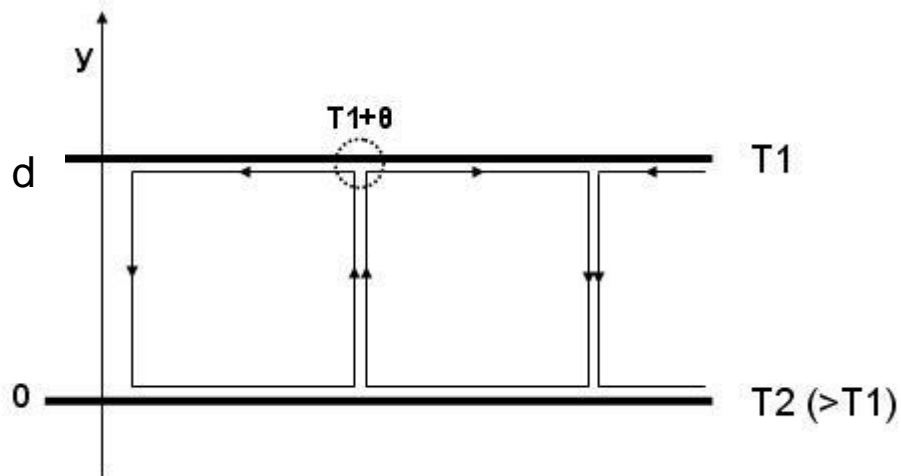
Fig. 2.9
Sketch showing the mechanism of Marangoni instability.
{Fig. redrawn from Reference [33], p460}

Thus the instability is driven by difference in surface tension between regions of the liquid surface at slightly different temperatures. The dimensionless parameter controlling this instability is the Marangoni number, defined as $Ma = \dfrac{\gamma'.\Delta T.d}{\eta.\kappa}$, where $\gamma' = \dfrac{d\gamma}{dT}$ represents the change of surface tension with temperature, d is the thickness of fluid layer, η is the viscosity, κ is the thermal diffusivity. Marangoni number, as in the case of Rayleigh number, is the ratio of a driving force and viscous force. The driving force here originating from the gradients in surface tension, which in turn is caused by temperature differences.

A comparison of Rayleigh-Bénard and Marangoni instabilities

Both in the case of Rayleigh-Bénard (RB) and Marangoni instabilities, the stabilizing mechanisms are the thermal conductivity and viscosity, which respectively tend to equalize the temperature distribution and to slow down the motion of the fluid. RB instability can show itself in cases where the boundary conditions are either free-

free, rigid-free, or rigid-rigid. Thus it does not necessarily need a free surface to set in. Marangoni instability on the other hand needs a free surface to set in.

Taking the ratios of the Rayleigh and Marangoni numbers gives:

$$\frac{Ra}{Ma} = \frac{(\alpha.g.\Delta T.d^3)/\nu.\kappa}{(\gamma'.\Delta T.d)/\eta.\kappa} = \frac{\alpha.\rho_f.g.d^2}{\gamma'} \qquad \ldots\ldots\ldots\ldots\ldots \quad (2.12)$$

Where we used $\nu = \dfrac{\eta}{\rho_f}$

For a given temperature difference, the ratio $\dfrac{Ra}{Ma}$ varies as d^2. Thus if $\dfrac{Ra}{Ma} > 1$, then Rayleigh-Benard instability dominates, whereas if $\dfrac{Ra}{Ma} < 1$, then Marangoni instability dominates.

Another interesting way to suppress the RB instability would be to reduce the gravitational effects of earth. Experiments have been done on space stations where the effects of acceleration due to earth's gravity is virtually absent, thus creating a situation where Marangoni instabilities completely dominate over RB instabilities.

Chapter 3

EXPERIMENTAL SETUP

Sample Cell

A photograph of top view of the sample cell is given below [Fig. 3.1]. The cell has an inner diameter of 13.7(± 0.1) cm and a height of 1.07(± 0.02) cm. It consists of two flat glass plates separated by a Teflon spacer. The glass plates are held together by screws connecting two flat aluminium rings. A thin Teflon sheet in between the aluminium ring and the glass plates reduces the pressure between them. Fig 3.2 shows a sketch of the components constituting the sample cell.
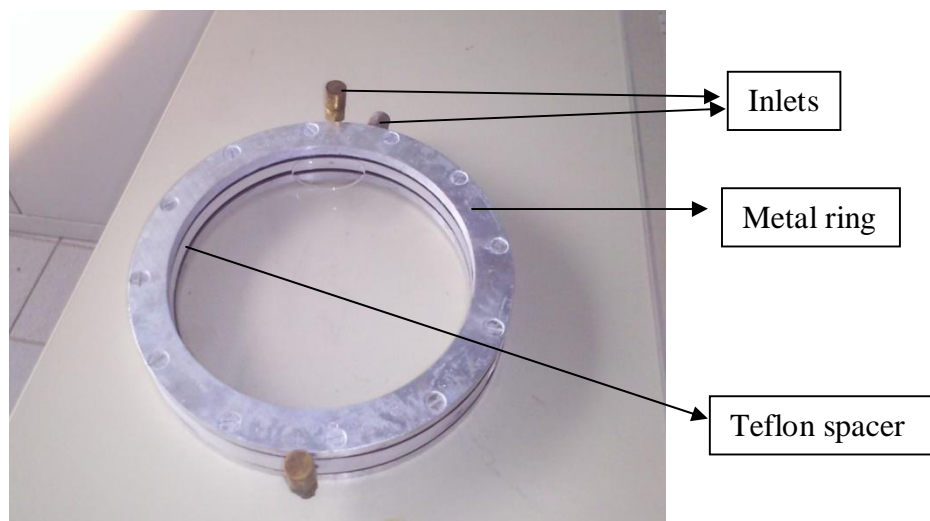
Fig. 3.1
Photograph of the top view of the sample cell. It has an inner diameter of 13.7(± 0.1) cm and a height of 1.07(± 0.02) cm. The constituent parts are labeled.
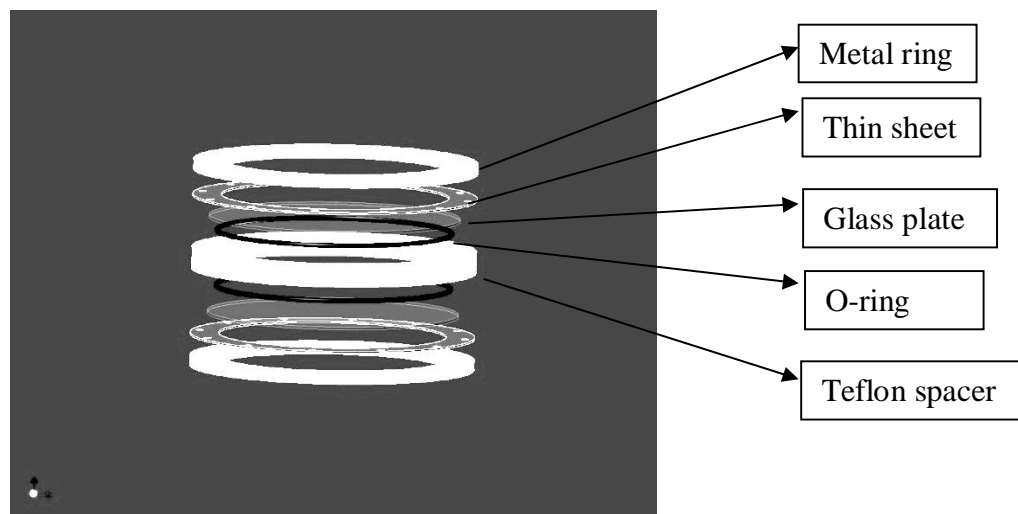
Fig. 3.2

Sketch of cell components. A Teflon spacer separates the glass plates which rest on O-rings. Direct contact of the glass plates with the aluminium ring is prevented by a thin teflon sheet

The glass plates rest on O-rings, above/below the Teflon spacer. The O-rings were of the material DT Viton with dimensions 140.0 x 3.0 mm. The use of NBR (nitrile butadiene rubber) O-rings had resulted in leakage of the sample. We then used Teflon coated O-rings, but they were relatively inflexible, and thus were not suitable for our use. Thus we decided on Viton O-rings. We found them to be both mechanically flexible and leak-proof against chemicals like methanol and hexane.

The construction of the cell is such that the borders of the Teflon spacer are raised a bit so that the glass plates and the Teflon borders are at the same height. This prevents the metal ring to put great pressure on the glass plate, yet not as loose as to let the glass plates move. The thin teflon sheet prevents direct contact of the metal ring with the glass plates. A sketch is shown in Fig. 3.3.
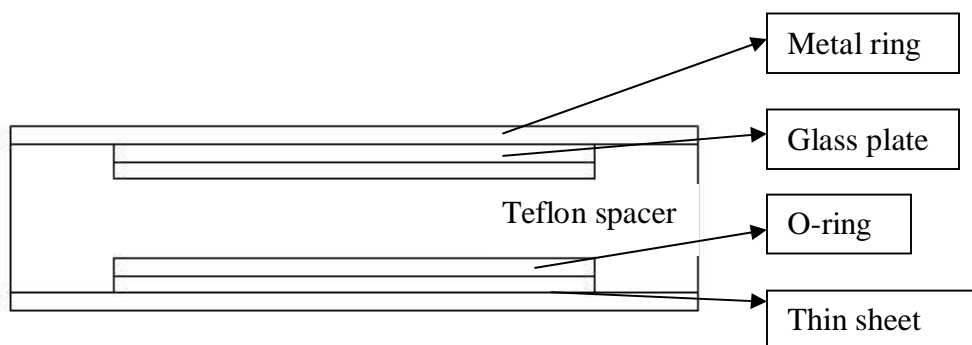

Fig. 3.3

Side view sketch of sample cell. Constituent parts are labeled.

The cell is provided with 3 inlets; 2 on one side and the third at a diametrically opposite spot. This is to facilitate easy loading and unloading of the cell.

The total volume of the cell is $158(\pm 1)$ ml.

Water bath and Thermostat

In order to control the temperature of the sample, a water bath in combination with a thermostat is used. The water bath was built in-house. The dimensions of the waterbath are 20 x 20 x 10 cm. It is made from Plexiglass. The sample cell is placed inside the water bath approximately equidistant from top and bottom of the water bath. A photograph of the setup is shown below [Fig. 3.4].
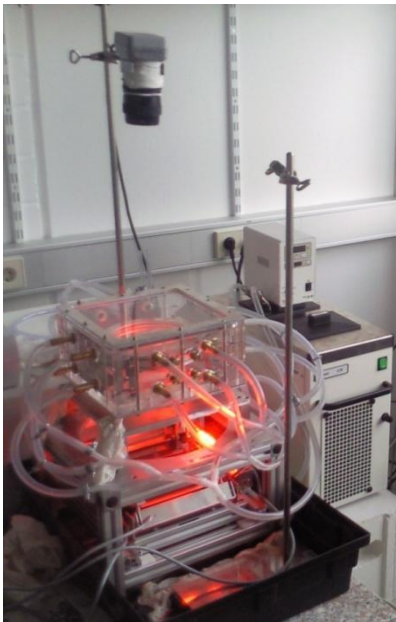
Fig. 3.4

Photograph of the experimental setup: Sample cell is sealed inside the waterbath(cannot be seen). The waterbath is provided with 8 inlets and 8 outlets, connected to the thermostat by pipes. The temperature inside the bath is controlled using a Haake K20 thermostat using a computer interface. The waterbath is illuminated by an array of LED's from below. Light scattering video microscopy is used.

The thermostat we use is Haake K20. It can cool or heat at various rates from below 0.1K/h to above 20K/h. The cooling rate is monitored using a computer interface. The main inlets and outlets from and to the thermostat is channeled further into 8 inlets and outlets when it reaches the water bath. The inlets and outlets are placed in a

symmetrical fashion. Two inlets on opposite sides are placed above the sample cell, and two of them below. Similar is the case with the outlets. This ensures a nearly uniform water flow inside the bath, which in turn ensures a nearly homogenous temperature. Additionally, the flow of water through the inlets can be independently controlled to achieve any temperature bias if needed. In fact, in our experiments we induce a temperature bias and keep the lower part of our sample colder than the upper part. A bias of a few millikelvins is achieved through controlled water flow through the inlets.

The total volume of water handled by the water bath and thermostat together is approx 10 litres. This is quite important because it helps in ensuring a well stabilized and homogenous temperature inside the bath. A very low volume of water would have made faster cooling rates meaningless, since it would be practically impossible to even out the temperature fluctuations by the small volume.

Setup Overview

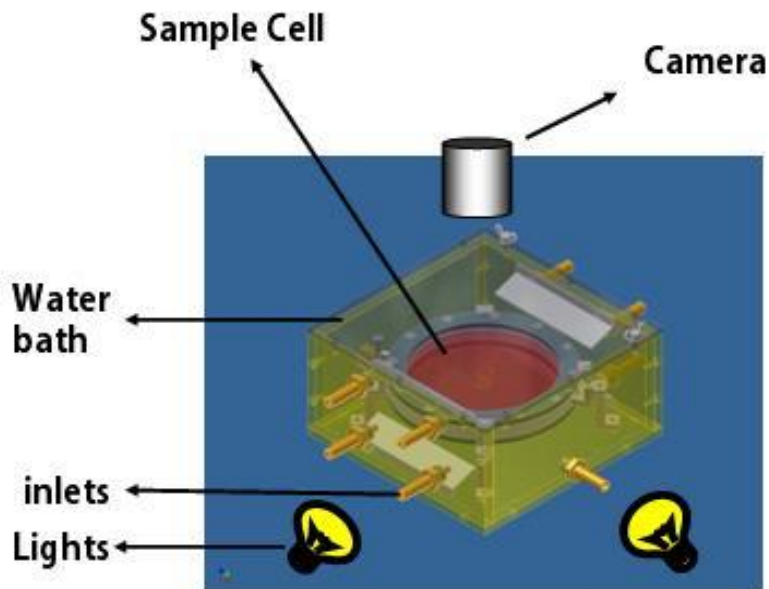A sketch of the experimental setup is given below [Fig. 3.5].

Fig. 3.5
Sketch of the experimental setup: sample cell is sealed inside the water bath. 8 inlets and 8 outlets keep a constant circulation of water, whose temperature is regulated by the thermostat.

The sample cell is placed approximately at equal distances from above and below the water bath. Below the water bath, we have 4 light sources. Each of them is an array of high intensity red LEDs. The array of LEDs was purchased from Weiss Imaging and Solutions GmbH. Each array consists of 10 LEDs, with a total output power of approx 50 watts. Depending on how to optimize the optics for the best results, we can choose between either using all 4 of the lights or just two of them.

A CCD camera placed above the water bath captures images at defined time intervals. We use Image Pro Plus software for data acquisition. Different acquisition speeds are possible. The maximum speed we got was approx. 2 frames per second

The basic method we employ in tracking the experiment is light scattering method. Light from the sources are pointed in such a way that no direct light enters the camera. When, for example droplets are formed within the sample, light gets scattered. This scattered light is then captured by the camera. Essentially, the optimal condition would be to have no direct light at all, and to have maximum intensity when scattering occurs.

Temperature Measurement

The temperature indicator on the Haake thermostat gives a fairly good idea of the temperature of the circulating water. But this is not necessarily the temperature inside the sample cell. A better scenario would be to have a possibility to measure temperatures inside the sample or at least very close to it. We use temperature probes, Pt100. They have the advantage that they are quite thin; they have a possibility to be moved around a bit inside the water bath. More importantly, they have a temperature resolution of $1/100^{th}$ of a degree Celsius, which is quite important in our experiments as we shall see later.

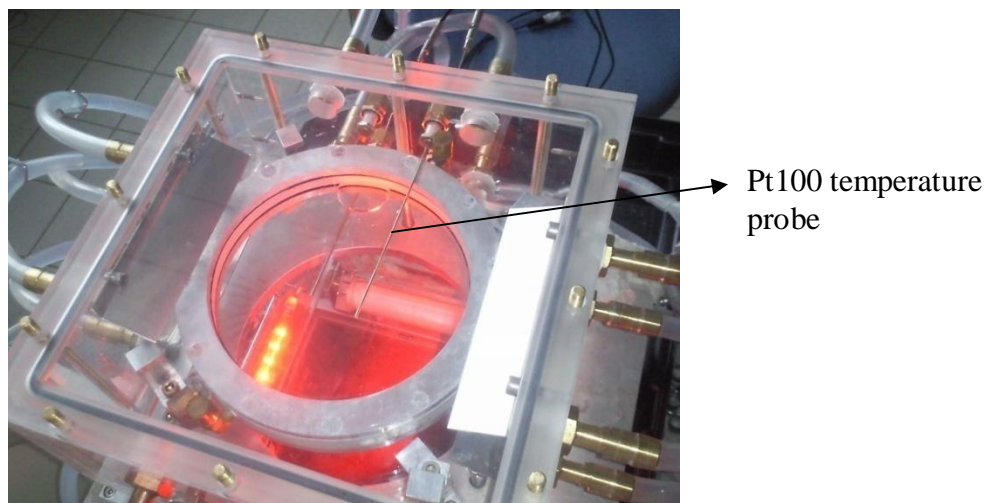A close-up figure of the temperature probes inside the water bath is given below [Fig 3.6].

Fig. 3.6

Pt100 temperature probes inside water bath. They are placed in through tiny holes drilled into the bath. They measure the temperature at different points, just above and below the sample cell with an accuracy of $1/100^{th}$ of a Kelvin.

We drilled 8 tiny holes for the temperature probes to enter. This allows us to measure the temperature at almost all positions close to the top and bottom of the sample cell.

To measure the actual temperature inside the sample cell directly is much trickier. This would mean to place some kind of a probe inside the sample. But then it is almost impossible to avoid the effects of the probe on the experiment itself. So we measure the temperature just above and below the cell and approximate the sample temperature to be the average of the two, which turns out to be a very good approximation at low cooling rates.

Microcalorimetry

The variation of specific heat relative to baseline was measured as function of temperature with a VP-DSC differential scanning microcalorimeter (MicroCal. Inc., Northampton, MA, USA). The microcalorimeter consists of coin shaped fixed-in-place twin cells of 0.518ml each, mounted in a cylindrical adiabatic chamber. The sample cell is filled with the mixture to be investigated while the reference cell is partially filled with water. The sample is exchanged for every scan. This is necessary because phase separation occurs after crossing the cloud point, and remixing by diffusion does not occur within an acceptable period of time.

The cells are heated at the whole top and bottom, while measurements are performed at the narrow sides. Both cells are heated with the same constant power. A thermoelectric device measures the temperature difference δT between the sample cell

and the reference cell. A cell feedback circuit drives δT to zero. Due to temperature scanning, exothermic (endothermic) reactions occur in the sample cell and less (more) power feedback is required to null δT. This power feedback is continuously monitored by a control unit. It determines the specific heat, $C_p(T)$, relative to a linear baseline $C_p^{base}(T)$. The remainder $C_p^{app}(T) = C_p(T) - C_p^{base}(T)$ yields the difference of specific heat of the mixture and reference solution.

SAMPLES

a) Requirements

In deciding the samples to use, we had to consider a few requirements. Firstly, the phase transition temperature of the binary mixture should be just below or above room temperature, depending on whether phase separation happens under heating or cooling. This is considerably helpful in preparing the sample and loading it optimally into the sample cell. In our setup, the sample cell is fixed inside a water bath, and homogenization of the sample would imply shaking of the whole water bath back and forth. This hardly ensures a complete homogenization of the sample. By bringing the phase transition temperature below room temperature, the sample can be first homogenized separately and then fixed inside the water bath. There is another reason why a low phase transition temperature is advantageous. Some of the components of the mixture we chose were highly volatile and had a relatively high thermal expansion coefficient. If we first load the sample in the two phase state and then heat it for homogenization, the pressure inside the cell increases. We found that this leads to leakage of sample through the outlets. High pressures inside the cell also pose a danger for the glass plates to break, thus exploding the cell.

Secondly, we had to choose a mixture which phase separated on reasonable time scales. For example, a phase-separation time scale of a few minutes would be ideal to track the events at a good time resolution, whereas a time scale of hours or days would make it hard to do the same. If we used mixtures with large phase separation times, only a few experiments could be done with a certain batch of samples. Thus we decided in favour of simple mixtures over polymer mixtures.

A third important requirement was for the mixture to have a good optical contrast at phase separation. Since the method we used was light scattering microscopy techniques, it was important that the droplets had sufficient contrast with respect to its surroundings to image them. This meant that the mixtures need a sufficient difference in their refractive indices.

b) The Samples

Keeping in mind the above requirements we experimented with different samples and finally decided on two mixtures, which fit closest to the requirements

1)Methanol+Hexane+Ethanol
2)Butoxyethanol+Water+Decane

The mixtures, quite evidently are not purely binary mixtures. A third component was doped into the binary mixtures, to lower the phase transition temperatures.
At first we had experimented with the following mixtures:

1)Methanol+Hexane
2)Butoxyethanol+Water

The phase diagram of methanol-hexane mixture is shown in [Fig.1.1]. Our first experiments, using a volume ratio of methanol: hexane=25:75, showed that the initial clouding and its subsidence took only some minutes, which was advantageous. The optical contrast of the droplets with respect to its surrounding was also good. The phase transition temperature was still above room temperature. The problems arising from this high phase transition temperature became apparent soon. The phase transition temperature increased for each subsequent experiment when the same sample was used. We understood that the high temperatures were causing the components to vapourise and leak out from the cell. This in turn allows water to enter the cell. Impurities such as water shifts the phase transition temperature of the methanol/hexane system upwards.
Thus we tried to search for a way to reduce the phase transition temperature below room temperature, of this sample, which otherwise was a good mixture for our experiments. We found out that doping this mixture with few percentages of alcohol shifted the phase transition temperature down. We tried to dope this mixture with three different alcohols: ethanol, pentanol and decanol. We found that for equal amount of the doping alcohol, decanol had the strongest effect of reducing the phase transition temperature followed by pentanol and then ethanol. Considering the relative toxicities and also the easy availability, we decided to choose ethanol as our doping agent, and thus we measured the phase diagram of this pseudo-binary mixture. The phase diagram of methanol-hexane-ethanol mixture is given below [Fig. 3.7] for a fixed ethanol volume fraction of 5% ethanol.
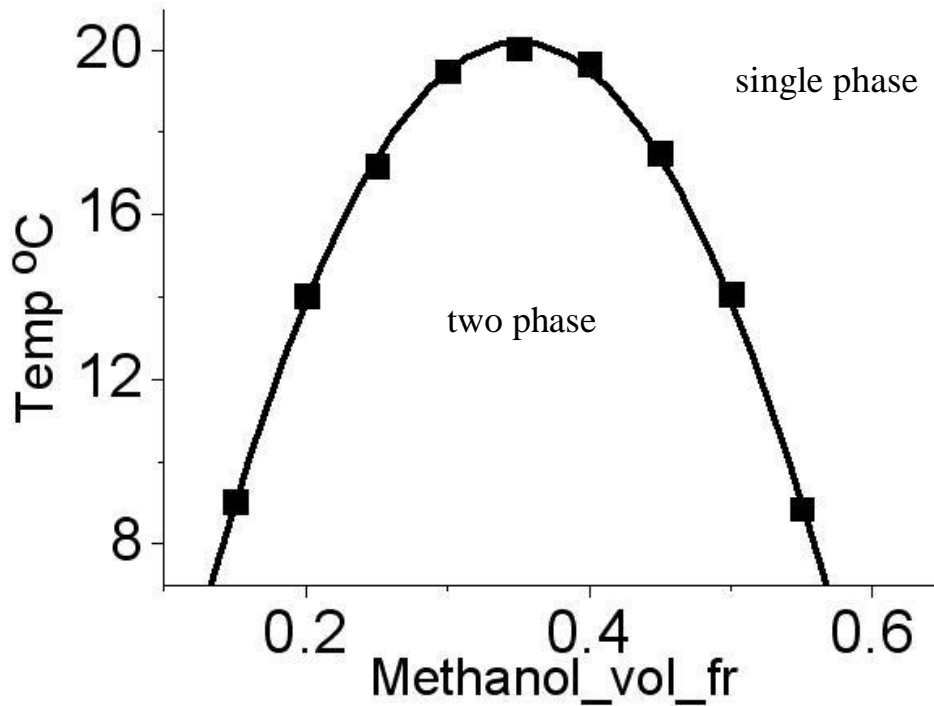
Fig. 3.7

Phase diagram of methanol/hexane/ethanol mixture. The squares indicate the measured data points. A parabolic fit function $T = -280\phi^2 + 196\phi - 14$ is added as a guide to the eye, where T is the temperature and ϕ is the volume fraction of methanol. The volume fraction of ethanol was kept fixed at 5%.

The phase diagram looks very symmetric. The data points are marked in the squares, and a parabolic fit is added to the data. The volume fraction of ethanol is kept constant at 5%, and the relative volume fractions of methanol and hexane are changed for the rest 95%. This mixture has the advantage that for all concentrations of methanol and hexane, it phase separates below room temperature (20°C).

A comparison of the methanol-hexane system and the ethanol doped system is given below [Fig. 3.8]:
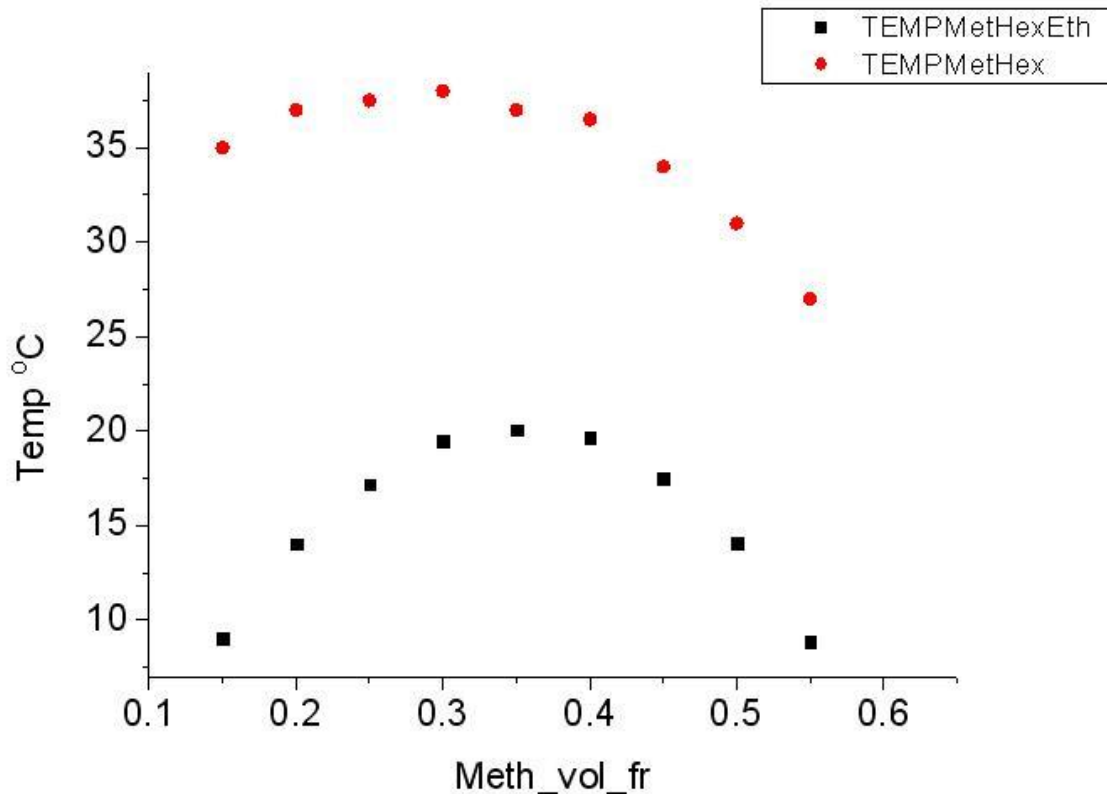
Fig. 3.8

Comparison of phase diagrams of methanol-hexane (circles) with that of methanol-hexane-ethanol (squares) system. The phase transition temperature has a shift of approximately 20 degrees. The phase diagrams look similar, but the latter is more symmetric.

The circles denote the data points of the methanol/hexane system, and the square data points denote that of the methanol/hexane/ethanol system.

We see that the slopes change, with the methanol/hexane/ethanol system having a more symmetric curve. The critical point also shifts towards higher methanol concentration, relative to the methanol/hexane system.

We wanted to compare the above system which phase separated under cooling, with another system which phase separated under heating. We wanted to know if the results depended on whether a system phase separated under heating or cooling.

So we used was a mixture of 2-butoxyethanol (also called C4E1) and water. Part of the phase diagram of a mixture of butoxyethanol and water is given in [Fig 1.2].

This system too phase separates in minutes and also has reasonable optical contrast. The only disadvantage being the high phase transition temperature, around 50 degrees. We doped this system with a few percent of decane, and we found that the phase transition temperature could be lowered. At low concentrations of C4E1, the system turned out to become three phases [36]. A phase diagram of the C4E1+water+decane system is given below [Fig. 3.9]. We kept the volume fraction of decane constant at 2%.
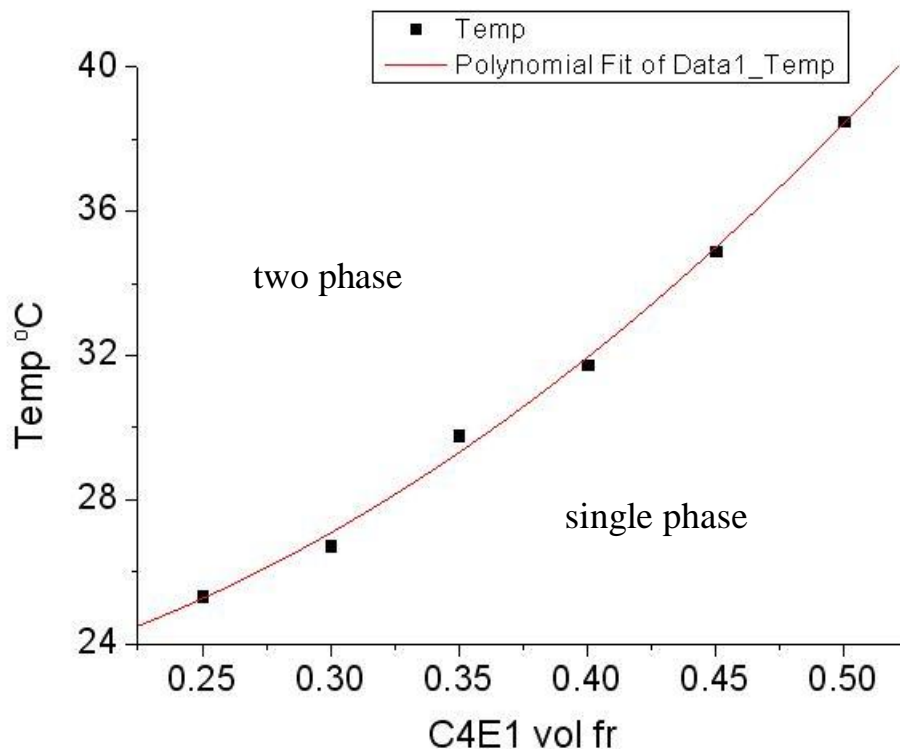
47

Fig. 3.9

Phase diagram of C4E1/water/decane. The squares indicate the measured data points. A parabolic fit function $T = 80\phi^2 - 9\phi + 22$ is added as a guide to the eye. T is the temperature and ϕ is the volume fraction of C4E1. The volume fraction of decane was kept at a fixed volume fraction of 2%

The square data points are the experimentally observed values, and a polynomial fit has been added onto it. We could not determine the left branch of this phase diagram. It has been known from literature [36] that a three component system of water-alkane-surfactant system forms a phase diagram exhibiting all three phase regions: namely, one phase two phase and three phase regions. We are not yet sure whether the data points we experimentally observed here forms a part of the more complete phase diagram for the system. But for the concentrations used in our experiments, starting from C4E1: water: decane = 0.25:0.73:0.02 to 0.50:0.48:0.02, we couldn't see three phases coexisting. Thus the area above the phase boundary in the figure represents a two phase region, and that below the boundary represents a one phase region.

Chapter 4

RESULTS AND DISCUSSION

Patterns: An overview

We started our experiments trying to find if thermodynamics of phase separation would have coupled to any hydrodynamic instabilities. If it would, then at right conditions, we expected to find some sort of patterns emerging within the system. In fact we actually found patterns appearing at the very beginning of phase separation, and also during the subsequent oscillations. The patterns at the beginning seemed to be more clear and pronounced. The patterns in the oscillations, on the other hand were faint and disordered. A better understanding of the pattern at the initial phase separation seemed useful for two reasons. First, due to its relative simplicity. Secondly, we hoped that a better understanding of these patterns would pave a way to the understanding of the more complex patterns appearing in the later stages of phase separation; the oscillations. We first study the case of methanol+hexane+ethanol system. Fig. 4.1 shows an image of the patterns appearing at the initial phase separation, and Fig 4.2 shows a typical pattern appearing in the oscillations.
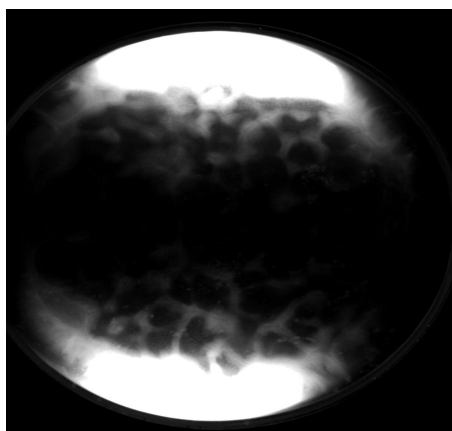

Fig. 4.1
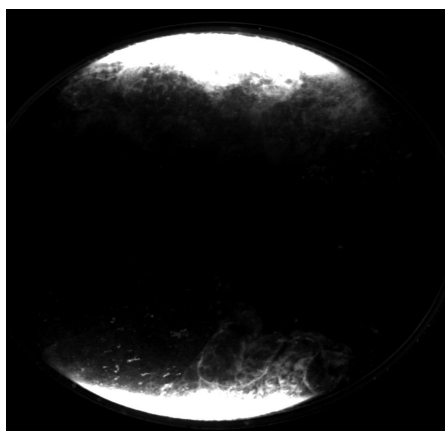*Typical patterns appearing at the initial phase separation.*

Fig. 4.2
Typical patterns appearing in the oscillations.

As we can see there is a gradient in illumination from two opposite sides to the middle of the sample cell. This is due to the position of the light sources. The two LED sources are on the two sides of the sample and, thus the stongest intensity lies on those sides, and gradually diminishes towards the middle. In reality, the whole sample phase separates together at a single time, although this gradient in illumination might wrongly suggest otherwise.

Patterns at different cooling rates.

We wanted to know whether the patterns in the initial phase separation depended on the cooling rates. We conducted experiments at various cooling rates such as 0.5 K/h, 1K/h, 2K/h, 5K/h and some even higher cooling rates. We took the composition of methanol:hexane:ethanol in the volume ratio 25:70:5. The samples were homegenised in the one phase region at room temperature. Then the homeogenous sample was loaded into the cell. The cell was then placed in the temperature regulated waterbath. Then it was cooled from a starting temperature of 21°C to 18°C, at the 4 different cooling rates. The figures below [Fig. 4.3] are typical images for the different cooling rates. The white dots appearing in the images are either air bubbles or impurities sticking at the surfaces of the waterbath. We took care to clean the sample cell with ethanol and acetone before each experiment. The air bubbles sticking on the outer surfaces, once the cell was sealed inside the waterbath were hard to remove. This does not in any way change the purity of the sample itself, although its absence would have been better for optical reasons.
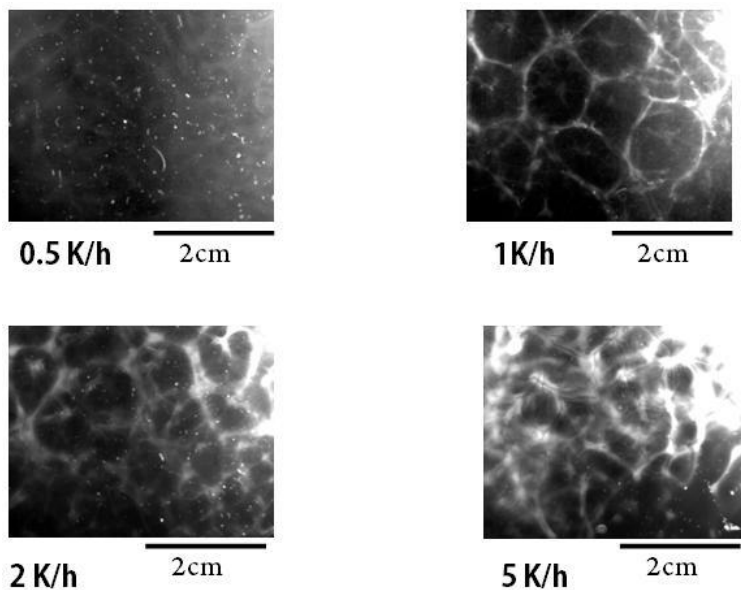

Fig. 4.3 *Figure showing the patterns at different cooling rates. At low cooling rates such as 0.5K/h, no patterns are seen. Cell like structures appear at 1K/h. Patterns at higher cooling rates of 2K/h and 5K/h become increasingly complex.*

It was seen that at cooling rates close to 1K/h, there were hexagonal shaped patterns appearing at the onset of phase separation [37]. The dark areas represent regions of no droplets and bright areas represent those of droplet rich areas. The patterns appeared simultaneously with the first turbidity. There was no time lag between the first signs of clouding and the appearance of patterns.

At 2K/h, the patterns resembled the above case a bit, although it was less persistent and ordered. At 5K/h, the patterns became even more disordered and less stable. A definite pattern size couldn't be attributed to them.

We tried very low cooling rates such as 0.5K/h to see the nature of patterns. We didn't find any patterns. The system tried to form very faint patterns at the onset of clouding, but never reached significance. The system became uniformly turbid thereafter, similar to the case seen in regular rectangular cuvettes.

Images were recorded as soon as the first patterns/turbidity is visible to the camera. This corresponds to time t=0. The evolution of the pattern for the different cooling rates can be seen from the following time series [Fig. 4.4]:
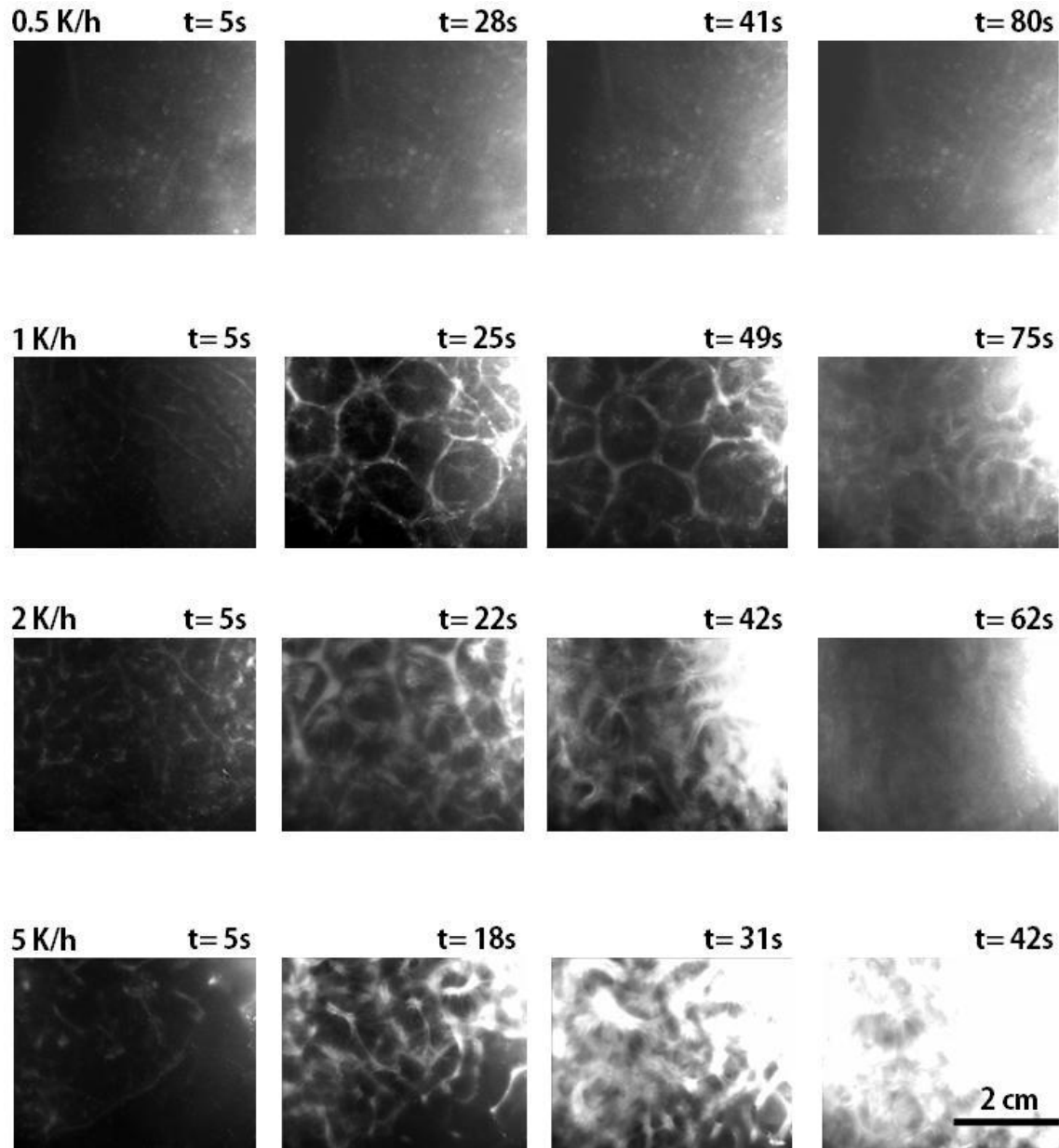
Fig. 4.4

Time series of evolution of patterns at different cooling rates. Patterns evolve slowly at 1K/h, and evolve faster in 2K/h and even faster in 5K/h.

Analysis

a) Pattern Size

It is reasonable to choose the patterns at 1K/h to determine their sizes, since they have the maximum symmetry in their shape, and thus are a good indicator of the general size of the pattern. They are also more stable than the patterns at higher cooling rates, thus allowing us to define a typical pattern size. The following graph gives a distribution of diameters done for 50 measurements [Fig. 4.6]. The measurements were done such that a line drawn from a border of a pattern to the approximate opposite spot defined a diameter. [Fig. 4.5]
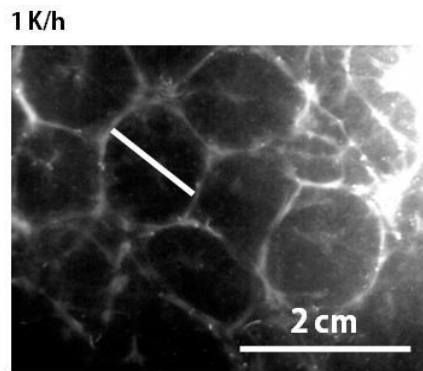

Fig. 4.5

Figure showing how a typical diameter of the cell is measured. A line joining a point on the edge of a cell with another point opposite to it was approximated as the diameter.
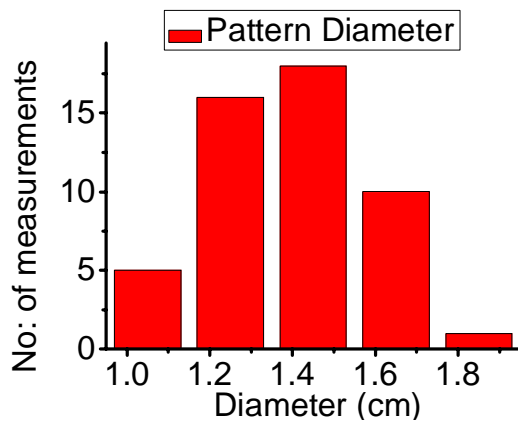

Fig. 4.6

Figure showing the size distribution of the cell structures. Approximately 90% of the cells have a diameter between 1.2 and 1.8 cm. This size is comparable to the height of the sample cell (1.1cm).

It can be seen that 88% of the measurements give a diameter value between 1.2 and 1.8 cm. This value of diameter becomes significant when we consider the height of our sample cell itself, which is 1.1cm. For convection patterns their sizes should be of the order of the system height, since these patterns are rolls spanning the system (see Fig.2.2). More exactly, the size of the patterns must be twice the height of the cell. This is because when we look from the top, the edge of the patterns is constituted by a locus of rolls (see for example Fig.2.5). Our patterns are a bit less than twice the height of the cell. This would suggest that the rolls in our system do not fully span the system, although quite close to it. We will analyze the possible reasons for this result shortly. The observations strongly suggest that the patterns are in some way originated from convection inside the system.

b) Correlation plots

Correlating images in a video sequence can be a good tool to understand how the patterns evolve with time. Here we use a method where each image in the sequence is correlated with its preceding image. If Im1 denotes the first image, and Im2 denotes the second image, then one can correlate these two images by means of a correlation coefficient R_{corr}, given by:

$$R_{corr} = \frac{\sum_{i=1}^{n}[(Im1_i - \overline{Im1})(Im2_i - \overline{Im2})]}{\sqrt{\sum_{i=1}^{n}(Im1_i - \overline{Im1})^2}\sqrt{\sum_{i=1}^{n}(Im2_i - \overline{Im2})^2}}$$

Where $Im1_i$ and $Im2_i$ are the intensities of ith pixel of Image 1 and 2 respectively, and $\overline{Im1}$ and $\overline{Im2}$ are the average intensities of Image 1and 2 respectively.

If the images are identical, it results in a correlation coefficient (R_{corr}) of 1. Any value lower than 1 indicates a difference between the images. Below [Fig.4.7], the first pair of images (Image1 and Image 2) is identical. The correlation coefficient R_{corr} is therefore equal to 1. (The seemingly different darkness between these images is just an optical illusion). The second pair of images (Image 3 and Image 4) have a correlation coefficient of 0.89, and apparently there is a difference between the images.
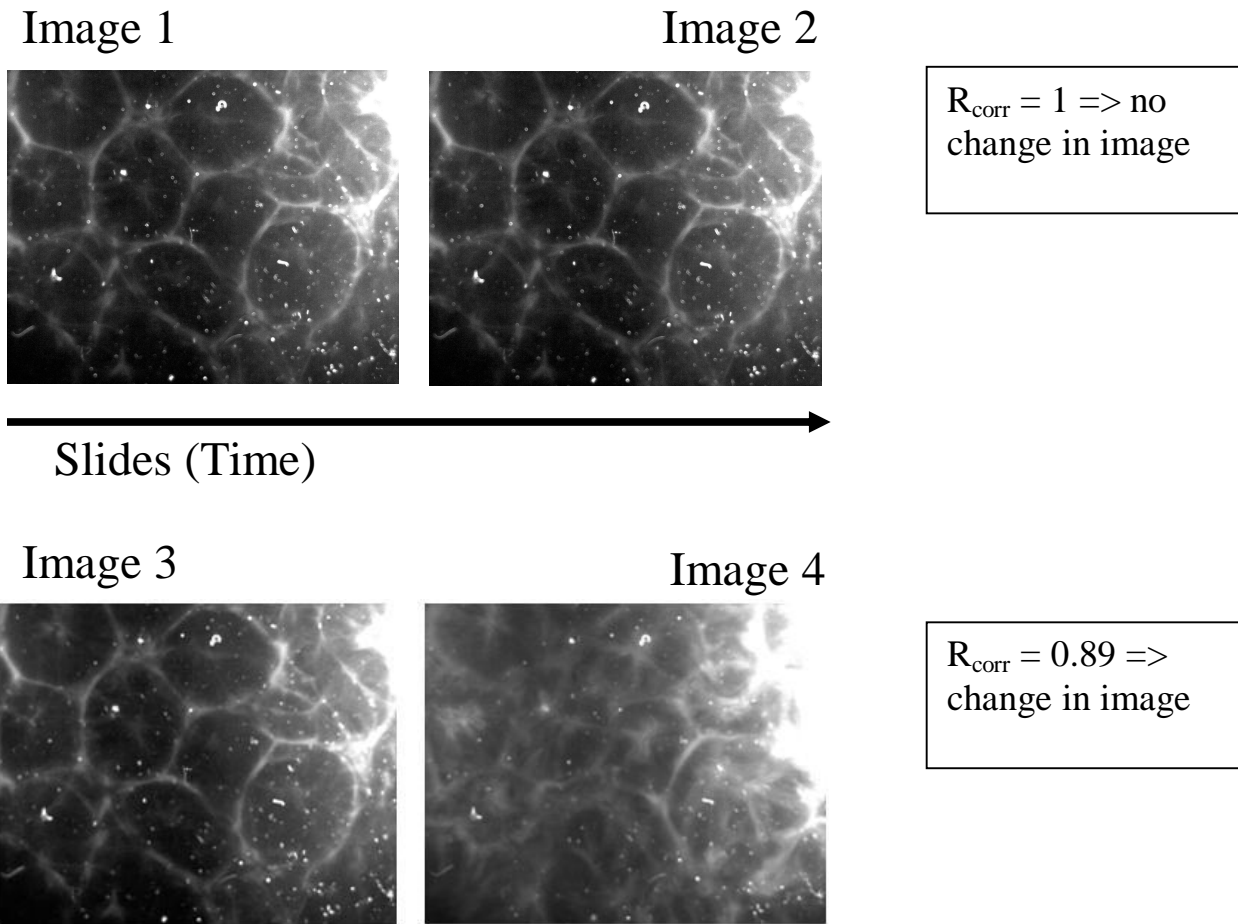
Image 1

Image 2

$R_{corr} = 1 \Rightarrow$ no change in image

Slides (Time)

Image 3

Image 4

$R_{corr} = 0.89 \Rightarrow$ change in image

Fig. 4.7

Figure demonstrating the relation between evolution of an image and the correlation coefficient. The first two images are identical, and it has a correlation coefficient $R_{corr}=1$. The latter two images are different. Their difference is reflected in the lower correlation coefficient, $R_{corr}=0.89$.

The following graph [Fig. 4.8] shows the value of R_{corr} plotted against time, for different cooling rates.
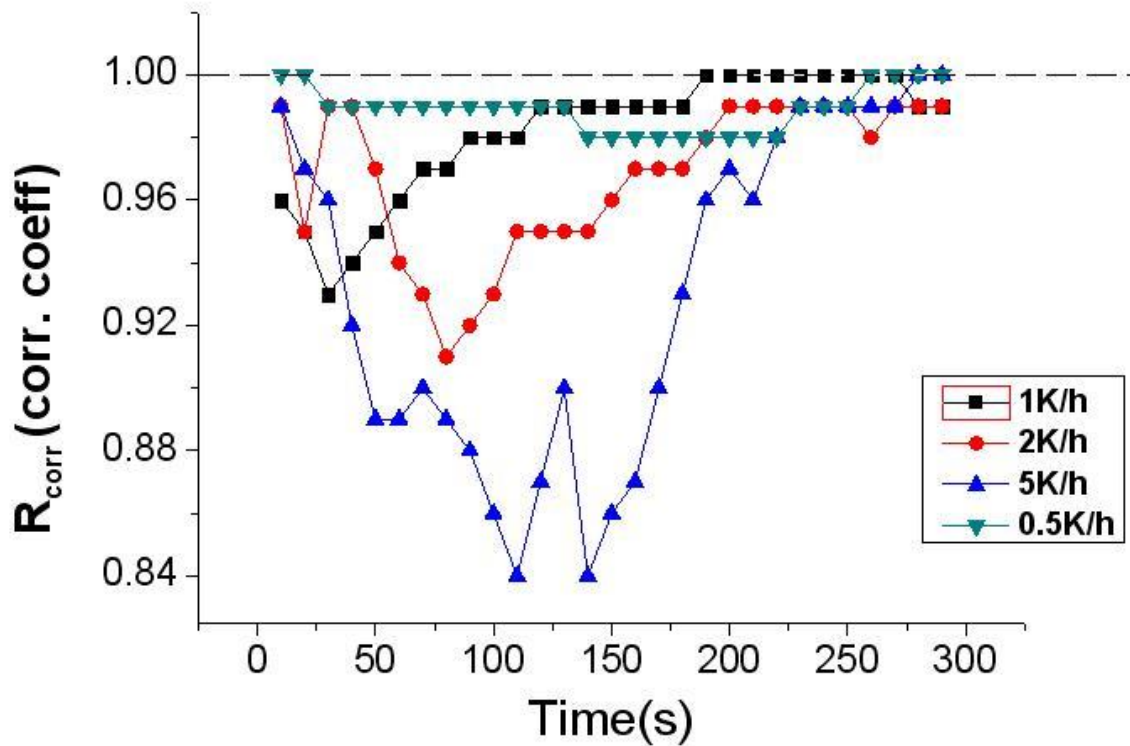
Fig. 4.8

Correlation coefficients (R_{corr}) between successive images for 4 different cooling rates are plotted. Higher value of R_{corr} implies slower evolution of the patterns and vice versa. R_{corr} values for 1K/h are plotted in squares, that for 2K/h in circle, in triangles for 5K/h, and inverted triangles for 0.5K/h. Patterns evolve slower at lower cooling rates, and increase subsequently for higher cooling rates. No patterns are seen for 0.5K/h

Each point on the graph is the correlation coefficient of an image with respect to its previous image in the sequence. It can be seen that for 0.5K/h, the value of the correlation coefficient hits the lowest value of 0.98, indicating that there is not much change between successive images. In fact the value dips below 1 mostly because of the overall change in turbidity, since no patterns are observed. For 1K/h, in the initial stages, the value of R dips slightly below 1, which indicates slight evolution of the pattern. The lowest value being around 0.92, this indicates that the pattern evolves only slightly. In the later stages, the value of R tends to approach 1, which indicates that the images barely change in time.

For 2K/h, the graph gives a slightly different plot in comparison to the 1K/h case. The R value tends to dip a bit more than the previous case, indicating a slightly faster evolving pattern than 1K/h, although not by too much.

For the 5K/h, the graph clearly indicates that the evolution of pattern is much faster than above two cooling rates. The R value tends to dip continuously with each subsequent image till it reaches a lower value of 0.84. Thereafter it starts to rise, and finally approaching 1. It should be noted that a final value of 1 does not necessarily imply that the patterns have stopped evolving. This is because during the phase separation, in

addition to the evolution of the patterns, the system as a whole is getting increasingly turbid. And in time, the turbidity is so large as to hide the patterns themselves. And thus the end images which are correlated are pure bright images (due to total turbidity).

Thus the initial values of R for different cooling rates are a good indicator to the evolution of patterns. Thus it is clear that the patterns evolve faster at higher cooling rates (5K/h or higher) than at lower ones (1 or 2 K/h).

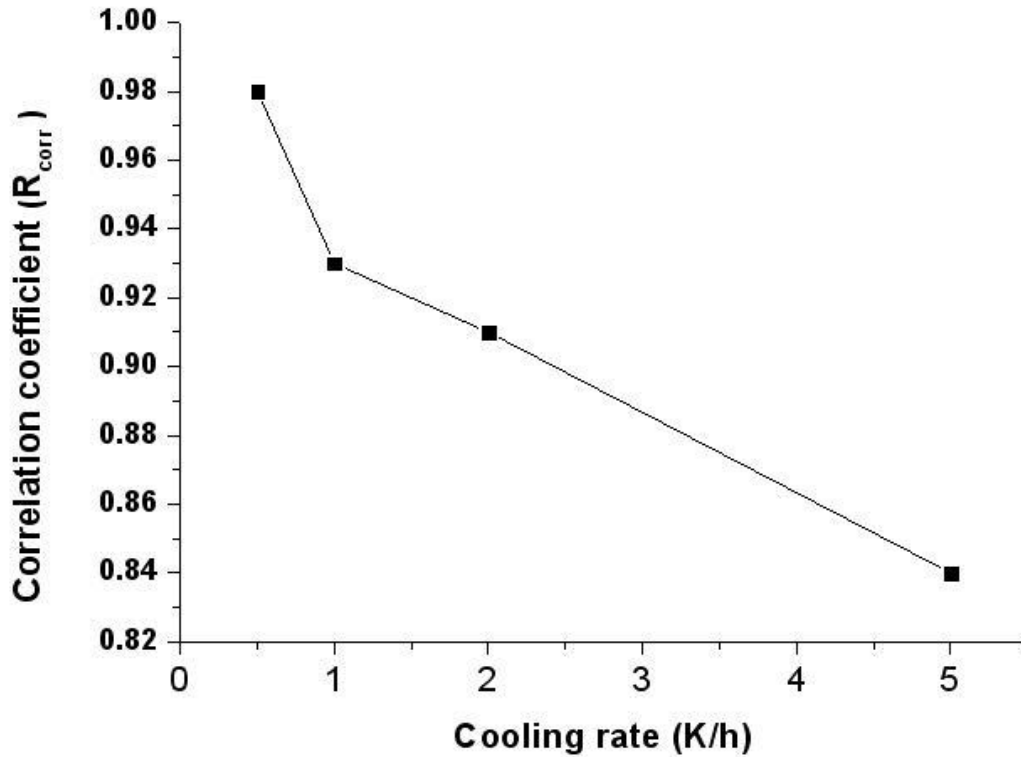The graph below [Fig 4.9] shows minimum values of R for the different cooling rates.

Fig. 4.9
Plot of the minimum values of correlation coefficient R_{corr}, for 3 different cooling rates. The points are joined by lines. The plot suggests a linear dependence of rate of pattern evolution with cooling rate.

Interpretation of patterns

Although the patterns we saw above closely resemble Rayleigh-Bénard convection patterns, it should be noted that we had already imposed an inverse temperature gradient. Thus with the upper side being warmer than bottom, the patterns cannot be directly attributed to RB type. Thus it suggests that the origin of the patterns should be within the sample itself. Or more precisely, it could be due to phase separation itself. We develop plausibility arguments for the emergence of our patterns and estimate

the critical numbers involved in the instability later (see: Plausibility argument for the patterns. p 62)

The process of phase separation in a binary mixture can be understood as follows. When the mixture in one-phase region is cooled continuously to below binodal, nucleation occurs, and droplets are formed. These droplets grow and move in the direction of gravity or against it, depending on their relative density. At the end, when this process continues and comes to a stop, a meniscus would be clearly formed separating the two phases.

The formation of droplets during phase separation produces a latent heat. This is because some degrees of freedom of the molecules are frozen and the corresponding energy is liberated as heat inside the system. We could estimate this latent heat produced for the methanol-hexane system from its DSC graph (see: Microcalorimetry p 59).

butoxyethanol-water-decane system

We did similar experiments on the butoxyethanol-water-decane system. Part of the phase diagram of this system is shown in Fig 3.9. The composition of butoxyethanol:water:decane was in the volume ratio 40:58:2. The system was in single-phase at room temperature. After mixing the sample thoroughly, it was loaded into the sample cell. We observed patterns at specific heating rates.

At a heating rate of 0.2K/h, the system became homogenously turbid, indicating the onset of phase separation. It remained turbid for a few minutes without any patterns appearing. Gradually the turbidity faded and the system became clear.

At 0.5K/h, patterns similar to the ones seen in methanol/hexane system emerged. The system first became homogenously turbid. The turbidity persisted for a few minutes, and the patterns appeared afterwards. This is different to the methanol/hexane case where the patterns appeared simultaneously with the first turbidity. Because we see an initial homogenous turbidity, and then the appearance of patterns after the turbidity has weakened in intensity, this suggests that the droplets formed at the initial phase separation have sedimented, and a meniscus has formed separating two liquid phases. At 5 K/h the patterns became complex.

The evolution of patterns for different heating rates can be seen from the following time series [Fig. 4.10].
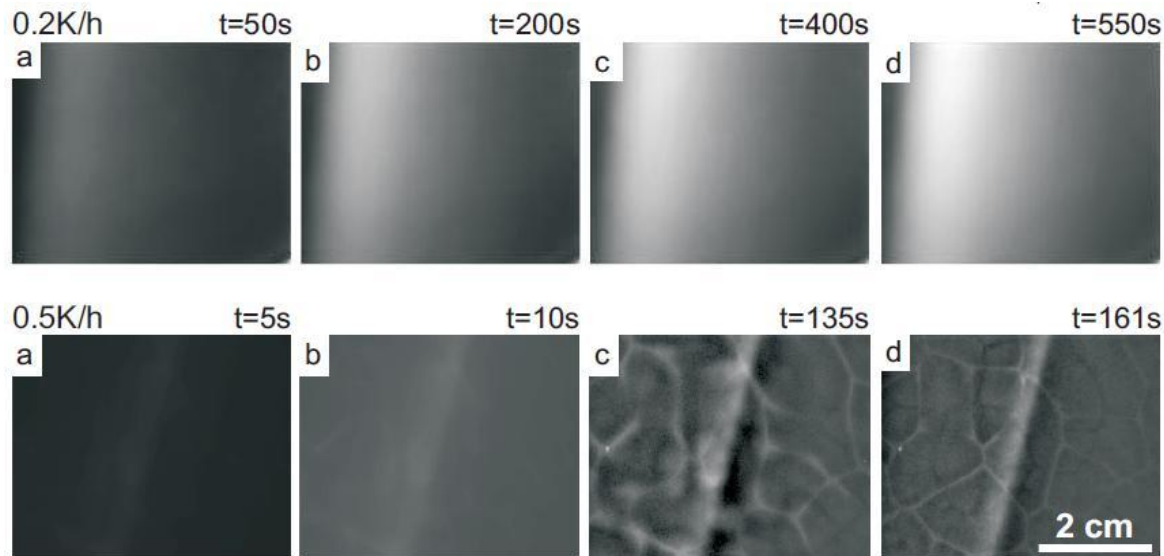
Fig. 4.10

Time series of images taken for different heating rates of butoxyethanol-water-decane system.

Typical images taken at different heating rates are given below [Fig. 4.11].
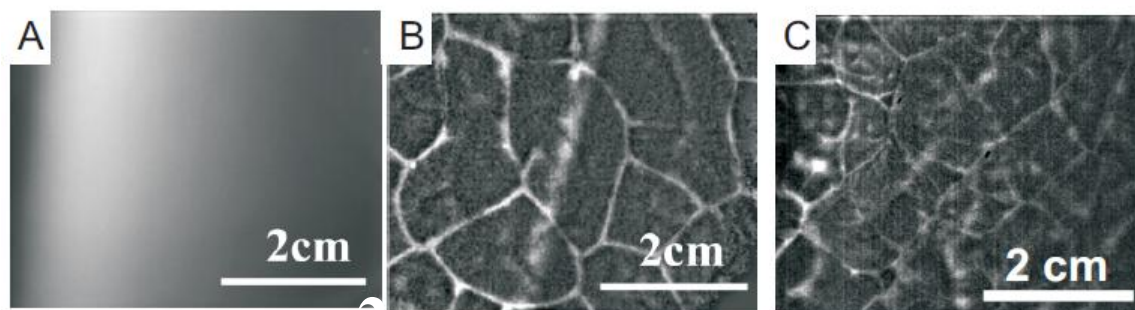

Fig. 4.11

Typical images at various heating rates for the butoxyethanol-water-decane system. (A) No patterns were seen for 0.2K/h. (B) Clear stable patterns emerged for 0.5K/h, and (C) patterns became complex for 5K/h.

Pattern size

The best stable patterns were observed at a heating rate of 0.5K/h. Diameters were measured for the various cells in the patterns. The size distribution for 50 measurements, done in the same way as in the methanol-hexane case [Fig. 4.5], is given below. [Fig. 4.12]
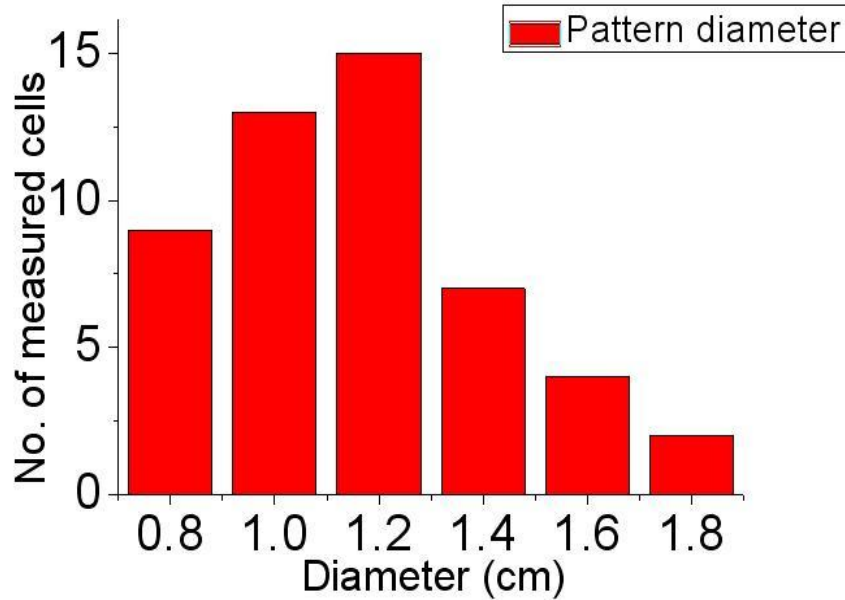
Fig. 4.12

Figure showing the size distribution of the cell structures. Approximately 80% of the cells have a diameter between 1.0 and 1.6 cm. This size is comparable to the height of the sample cell (1.1cm).

It can be seen that 80% of the cells have a diameter in the range 1.0 cm to 1.6 cm. This again is in the order of the height of our sample cell. This suggests that the patterns are a manifestation of some sort of convective motion of the fluid.

Microcalorimetry

(a) Methanol-hexane mixture

When a mixture enters the two-phase region nucleation of droplets give rise to a latent heat, reflected in a change of the specific heat. If the phase transition is accompanied with phase separation the composition of the coexisting phases change. This brings about a change of the absolute value of $C_p(T)$ after phase transition (see Fig. 4.13). $C_p^{app}(T)$ almost remains constant as long as the mixture is still single-phase. Passing the cloud point causes that $C_p^{app}(T)$ first increases, passes a maximum, decreases and levels off if heated/cooled deep into the two phase region. About 0.5 K after passing the cloud point the signal $C_p^{app}(T)$ starts to oscillate (inset in Fig. 4.13). These oscillations are caused by the repeated cycles of nucleation growth and coarsening as discussed previously [11, 14]. Because we focus on the interplay between thermodynamics and hydrodynamics just after passing the cloud point $(|T - T_c| \ll 0.5K)$ the oscillations can be ignored here.
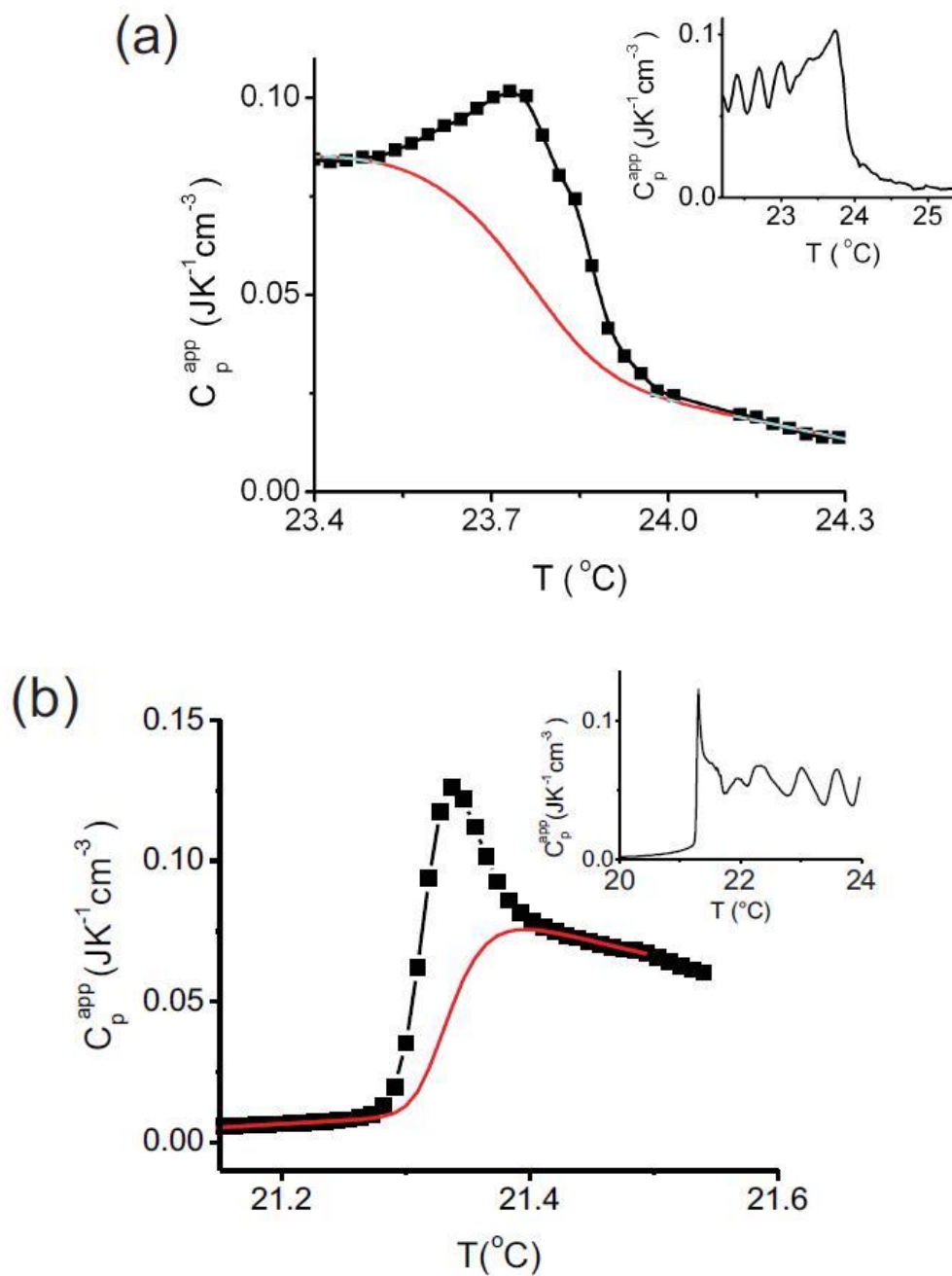
Fig 4.13

DSC thermogram showing the onset of phase separation, denoted by the first peak. The mixtures are (a) methanol+hexane+ethanol and (b) butoxyethanol+water+decane. The area between the curves depicts the latent heat set free during phase separation. Subsequent peaks depict the oscillations during phase separation. Sample composition in volume ratio methanol: hexane: ethanol 25:70:5. The composition of butoxyethanol: water: decane in the volume ratio 40 : 58 : 2

The latent heat is given by the area under the first peak. It can be estimated from the area between $C_p^{app}(T)$ and the baseline (smooth curve). For the quasibinary mixtures of methanol and hexane the phase transition gives rise to a latent heat of $W_{MH} = 0.015 \pm 0.005$ J/ml. This exceeds the latent heat set free for the mixtures of C_4E_1 - water doped with decane $W_{C4E1/H2O} = (5.5 \pm 1)\ 10^{-3}$ J/ml.

The latent heat can be regarded as an internal heat source giving rise to an increase of temperature. Latter depends on the heat capacity of the solution.

$$\Delta T = \frac{W}{\Sigma_i(C_p^i \cdot m_i)}$$

Where W is the latent heat, $m_i = \Phi_i \rho_i$ stands for the mass of component i, and C_p^i the specific heat capacity of component i. The components taking the values of i are M: methanol, H: hexane, E: ethanol, C4E1: butoxyethanol, H2O: water and D: decane.

Here we assume that the specific heat capacities as well as the masses are additive. Inserting the thermodynamic parameters listed in literature (see Table 4.1) [4, 22] gives rise to the following increases of temperature ΔT:

$$\Delta T_{MH} = \frac{W_{M_H}}{\left(\Phi_M \rho_M c_p^M + \Phi_H \rho_H c_p^H + \Phi_E \rho_E c_p^E\right)}$$

$$\approx \frac{0.015\,\frac{J}{cm^3}}{\left(0.25 * \frac{0.79\,g}{cm^3} * 1.6\,\frac{J}{gK} + 0.70 * 0.65\,\frac{g}{cm^3} * 2.3\,\frac{J}{gK} + 0.05 * \frac{0.79g}{cm^3} * \right.}$$

$$\approx 0.01\,K$$

$$\Delta T_{C_4E_1H_{2O}} = \frac{W_{C4E1_{H_{2O}}}}{\left(\Phi_{C4E1}\rho_{C4E1}c_p^{C4E1} + \Phi_{H2O}\rho_{H2O}c_p^{H2O} + \Phi_D \rho_D c_p^D\right)}$$

$$\approx \frac{0.005 \, \frac{J}{cm^3}}{\left(0.4 * \frac{0.90g}{cm^3} * 2.1 \frac{J}{gK} + 0.58 * 1 \frac{g}{cm^3} * 4.2 \frac{J}{gK} + 0.02 * \frac{0.73g}{cm^3} * 2.2 \frac{J}{gK}\right)}$$

$$\approx 0.002 \, K$$

	C_p [J/gK]	P $\frac{g}{[cm^3]}$
methanol (M)	1.6	0.79
hexane (H)	2.3	0.65
ethanol (E)	2.5	0.79
butoxyethanol (C4E1)	2.1	0.90
water (H2O)	4.2	1.00
decane (D)	2.2	0.73

Table 4.1

In both mixtures the latent heat increases the temperature of the mixture. The temperature bias is such that the lower plate is 0:01 K colder than the upper one. Therefore, in mixtures of methanol, hexane and ethanol the first nuclei appear near the bottom plate. This leads to a slight rise of the temperature, reducing the temperature bias. How strongly the latent heat changes the temperature profile depends not only on sample composition and geometry
but also on the cooling rate. In mixtures of C_4E_1/water the latent heat induced increase
of temperature is much less than the applied temperature bias. Therefore, it is unlikely to influence pattern formation.

Plausibility argument for patterns:

Estimation of the modified Rayleigh number.

As we already saw in Chapter 2, for the Rayleigh-Bénard instability, the Rayleigh number determines whether or not the system will exhibit a convective instability. Our system most closely resembles a rigid-free boundary problem, since the patterns originate somewhere above the bottom plate and extend to the upper glass plate. The critical Rayleigh number for such a system is 1100. Thus the determination of whether convective instability arises or not in our system boils down to the determination of the Rayleigh number, and its proximity to the critical value. In the following analysis we estimate the Rayleigh number for our system starting from the heat diffusion equation. We can write the one dimensional heat equation as:

$$\frac{\partial T(x,t)}{\partial t} = \kappa \frac{\partial^2 T(x,t)}{\partial x^2}$$ …………………………………. (4.1)

Where T is the temperature in Kelvin at any position x and time t, and κ is the thermal diffusivity with the units m^2 / s.

Consider a vertical cross section of our sample cell, as shown in the Fig.4.14. Let d denote its thickness. We take the middle of the cell to be the origin, and the system extends to $+\frac{d}{2}$ and to $-\frac{d}{2}$ from the origin, on the vertical x axis.
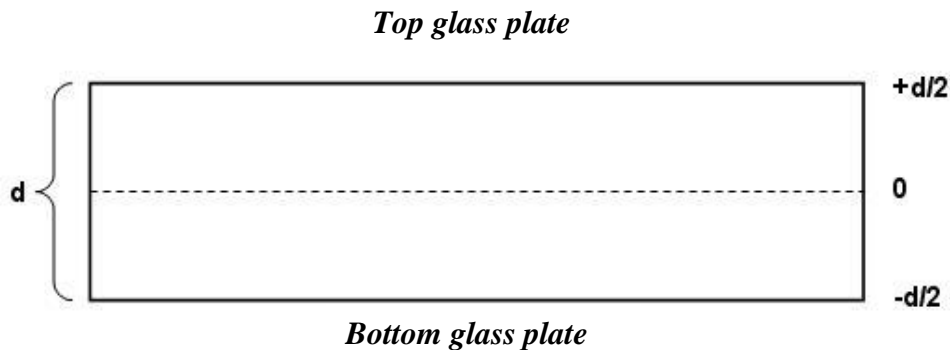
Top glass plate

Bottom glass plate

Fig. 4.14
Vertical cross section of sample cell. The vertical axis is x, where the height of the system extends from –d/2 to +d/2.

We cool our system from above and below at a constant cooling rate of γ. Assuming the same temperature on both sides of the cell, we can write the following boundary conditions:

$$T(x,0) = 0$$

$$T(\tfrac{1}{2}d,t) = -t.\gamma$$

$$T(-\tfrac{1}{2}d,t) = -t.\gamma$$

……………………………………..(4.2)

We can find the stationary solution (i.e., the solution after an initial transient time) to the heat equation analytically as follows. The stationary solution must follow the continuous cooling of the cell. For this reason, we can assume the temperature at any point to be a function separable into space and time dependent parts. We could write:

$$T(x,t) = \tau(x) + (-t.\gamma)$$

……………………………………..…(4.3)

where $\tau(x)$ denotes the space dependence of the temperature and $(-t.\gamma)$ gives its time dependence, as given by the continuous cooling at the rate γ. Using this expression in the heat diffusion equation yields:

$$-\gamma = \kappa \frac{\partial^2 \tau(x)}{\partial x^2}$$

………………………………………….....(4.4)

The second derivative of $\tau(x)$ equals a constant. This implies that $\tau(x)$ should be a parabolic function of the general form:

$$\tau(x) = ax^2 + bx + c$$

………………………………………….(4.5)

In our case, we apply a constant temperature bias, $Tb \sim 0.01$K, keeping the upper glass plate warmer than the lower. At constant cooling rates, we have measured that this bias remains a constant (for 80% of the measured time, using Pt 100 probes). Thus we can assume a linear function describing this bias.

$$Tbias(x) = kx + l$$

………………………………………..(4.6)

where k and l are constants.

When the relative temperature of bottom glass plate $\left(\dfrac{-d}{2}\right)$ is at 0, the same of the upper glass plate $\left(+\dfrac{d}{2}\right)$ would be Tb

$$Tbias\left(\frac{-d}{2}\right) = 0$$

$$Tbias\left(\frac{+d}{2}\right) = Tb$$

Using these boundary conditions in eqn. (4.6), we have

$$-k\frac{d}{2}+l=0$$

$$+k\frac{d}{2}+l=Tb$$

solving these equations, we get the values of k and l as

$$k=\frac{Tb}{d}, \quad l=\frac{Tb}{2} \qquad \ldots\ldots\ldots\ldots\ldots\ldots\ldots\ldots\ldots\ldots\ldots\ldots\ldots (4.7)$$

Thus we can write the position dependent bias temperature as

$$Tbias(x)=\frac{Tb}{d}.x+\frac{Tb}{2} \qquad \ldots\ldots\ldots\ldots\ldots\ldots\ldots\ldots\ldots\ldots..\ldots.(4.8)$$

If we add this bias to the symmetric solution of the space dependent temperature function eqn. (4.5), we have,

$$\tau(x)=ax^2+bx+c+Tbias(x)$$

or

$$\tau(x)=ax^2+bx+c+\frac{Tb}{d}x+\frac{Tb}{2} \qquad \ldots\ldots\ldots\ldots\ldots\ldots..\ldots.(4.9)$$

.
Using this value of $\tau(x)$ in eqn. (4.4) gives:
$$-\gamma=2.\kappa.a$$
Thus:
$$a=-\frac{\gamma}{2\kappa} \qquad \ldots\ldots\ldots\ldots\ldots\ldots\ldots\ldots.(4.10)$$

We have the boundary condition: $T(x,0)=0$, for symmetric cooling. On applying the bias, we have the following boundary conditions:
$$T\left(\frac{-d}{2}\right)=0, \quad T\left(\frac{d}{2}\right)=Tb.$$ Since this bias is space dependent, with no temporal dependence, we can write

$$\tau(-\frac{d}{2})=0$$

$$\tau(+\frac{d}{2})=Tb$$

This implies:

$$a\frac{d^2}{4} - b\frac{d}{2} + c + \frac{Tb}{d}\left(\frac{-d}{2}\right) + \frac{Tb}{2} = 0$$

and

$$a\frac{d^2}{4} + b\frac{d}{2} + c + \frac{Tb}{d}\left(\frac{d}{2}\right) + \frac{Tb}{2} = Tb$$

Solving the above two equations give:

$$c = -a\frac{d^2}{4}, \quad b = 0$$

Substituting the value of a yields the value of c to be:

$$c = \frac{\gamma.d^2}{8.\kappa}$$

Thus we can write the stationary analytical solution as:

$$T(x,t) = -\frac{\gamma}{2\kappa}x^2 + \frac{\gamma.d^2}{8\kappa} + \frac{Tb}{d}x + \frac{Tb}{2} - t.\gamma \qquad \dots\dots\dots\dots\dots\dots\dots(4.11)$$

In turn, we used Maple to calculate numerical solutions to full problem.

The typical heat diffusion time Δt can be estimated as follows. Consider the diffusion equation (4.1). If we take finite differences for the variables, we can write:

$$\frac{\Delta T}{\Delta t} \approx \kappa\frac{\Delta T}{(\Delta x)^2} \qquad \dots\dots\dots\dots\dots\dots\dots\dots\dots\dots\dots\dots(4.12)$$

Which gives:

$$\Delta t \approx \frac{(\Delta x)^2}{\kappa} \qquad \dots\dots\dots\dots\dots\dots\dots\dots\dots\dots\dots\dots(4.13)$$

Here Δx denotes the typical distance through which heat diffuses, and Δt, the typical time for heat to diffuse through that distance. This gives us the typical time scales involved in heat-diffusion. For our system, $\Delta x = d$.

Thus, $\quad \Delta t \approx \frac{d^2}{\kappa}$

Comparing the stationary analytic solution with the numerical time-dependent solution allows us to estimate after what portion of this time, the time dependent solution converges towards the stationary solution.

The following plot [Fig. 4.15] shows comparison between the analytic solution of the heat equation with the numerical solution for 5 different times. We see that after 50% of the heat diffusion time, the system almost reaches the stationary temperature profile.
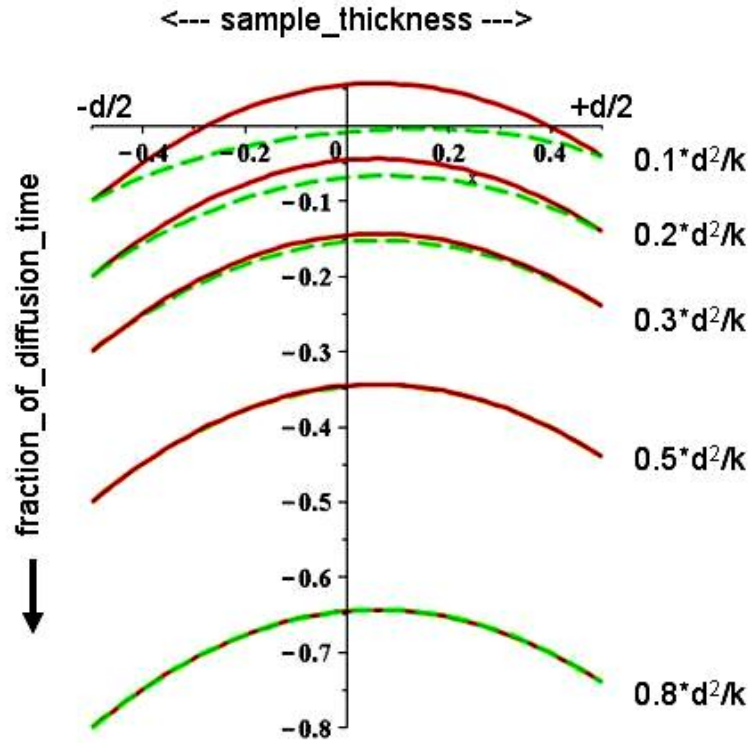
Fig. 4.15
Plot showing the comparison between the analytic solution of the heat equation with the numerical solution for 5 different times. The horizontal axis represents the sample thickness (from –d/2 to +d/2), and the vertical axis the fraction of the typical diffusion time. The dashed curve shows the numerical solution and the solid curve shows the analytic stationary solution. The system takes time to replicate the heat profile given by the analytic solution. After a fraction of almost 0.5 times the typical diffusion time, the numerical solution fairly coincides with the stationary temperature profile given by the analytic solution.

The dashed curves show the numerical solution and the solid curves show the analytic stationary solution to the diffusion equation.

The temperature difference ΔT between the centre of the sample and the boundaries can be estimated as follows:
The temperature after the transient time at any point x inside the cell is given by eqn. (4.11).
In particular, the temperature at the origin is given by:

$$T(0,t) = \frac{\gamma \cdot d^2}{8\kappa} + \frac{Tb}{2} - t \cdot \gamma$$

The position of temperature-maximum inside the cell can be found by equating the gradient of eqn. (4.11) with respect to x, to zero.

$$\frac{dT(x,t)}{dx} = 0$$

$$\Rightarrow \frac{-\gamma}{\kappa}x + \frac{Tb}{d} = 0$$

Solving for x, we get

$$x = \frac{\kappa.Tb}{\gamma.d} \qquad \dots\dots\dots\dots\dots\dots\dots\dots\dots\dots\dots\dots(4.14)$$

We see that the position of the maximum temperature depends on the cooling rate, thermal diffusivity of the sample, sample thickness and the temperature bias we apply.

The difference in temperature between the position of maximum temperature and the upper plate is given by:

$$\Delta T = T\left(\frac{\kappa.Tb}{\gamma.d}\right) - T\left(+\frac{d}{2}\right) = -\frac{Tb}{2} + \frac{Tb^2\kappa}{2.\gamma.d^2} + \frac{\gamma.d^2}{8.\kappa} \qquad \dots\dots\dots\dots\dots(4.15)$$

We have seen that the classical Rayleigh number is given by eqn. (2.8).
For our case, substituting the fluid thickness as the distance between the top plate and the position with maximum temperature inside the cell, we can write the modified Rayleigh number $Ra*$ as

$$Ra* = \frac{g\alpha.\Delta T.(\frac{d}{2} - \frac{\kappa.Tb}{\gamma.d})^3}{\nu.\kappa} \qquad \dots\dots\dots\dots\dots\dots\dots\dots\dots\dots\dots (4.16)$$

where g is the acceleration due to gravity, α is the thermal expansion coefficient, ν is the kinematic viscosity and κ the thermal diffusivity.

methanol/hexane/ethanol system:
The estimated values for the above quantities for the methanol/hexane/ethanol mixture are as follows [38-39]. Values of α, ν and κ were taken as the weighted average of the components.

$$\alpha = 1.3 \cdot 10^{-3} K^{-1}$$

$$\nu = 5.3 \cdot 10^{-7} m^2/s$$

$$\kappa = 8.7 \cdot 10^{-8} m^2/s$$

For a cooling rate of 1K/h, taking the value of g to be $9.81 m/s^2$, and taking our cell height d= (1.07 ± 0.02) cm, we get the modified Rayleigh number for the methanol/hexane system to be:

$$Ra^* \approx 1400(\pm 200)$$

This is above the critical value for convective instability, 1100. The latent heat due to phase separation would drive the instability further, but the exact amount of the influence cannot be known from this analysis. This can be understood only from detailed simulations. One of the problems is that we cannot know the exact thickness through which the instability is driven. Work done by Dr. Hayase show that even without the temperature bias or the contribution from latent heat, the convective patterns are not system spanning. The height of these patterns is less than the sample cell thickness. Our experiments also show that the patterns are not system spanning. The above values are calculated assuming the thickness to be that between the top plate and the plane of maximum temperature inside the sample. The error range in the modified Rayleigh number shown above comes from the strong fifth power dependence of the Rayleigh number on the cell thickness, which will be briefly discussed later. We have a cell whose thickness is $1.07(\pm 0.02)$ cm. The other uncertainties come from the actual values of the material parameters of the constituents in the mixed state. Although a weighted average of the individual components are taken, changes in temperature, and also the equilibrium composition of the mixture can affect the values.

For a lower cooling rate of 0.5K/h, we get the value to be

$$Ra^* \approx 600(\pm 100)$$

This is lower than the critical value for convection. The error in the modified Rayleigh number is lower in this case because of the lower cooling rate used.

Thus for a fixed sample thickness d, depending on the cooling rate γ, there can be scenarios where convective instability is present or absent. This predicts that in an experiment with varying cooling rates, at least two different scenarios would be evident: a regime where patterns are present, and one without them. This is consistent with our experimental findings that at lower cooling rates of approx. 0.5K/h, we observe no patterns but at higher cooling rates of 1K/h and above, patterns emerge in our system.
The dependence of Rayleigh number on the cooling rate for a fixed sample thickness of 1.07cm can be visualized from the following plot [Fig. 4.16].
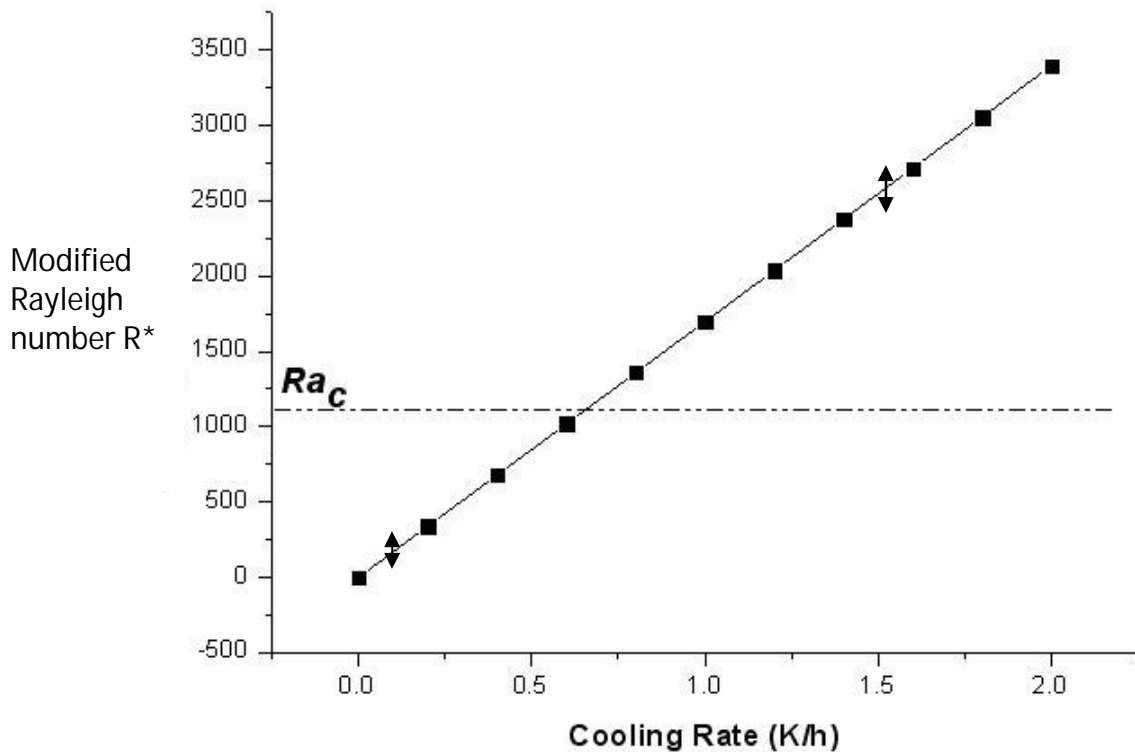
Fig. 4.16

Plot showing the dependence of modified Rayleigh number R* on the cooling rate for the methanol-hexane-ethanol system, for a sample thickness of $1.07(\pm 0.02)$ *cm. The error is approx* ± 100 *for very low cooling rates, and approx.* ± 200 *for higher cooling rates.*

The dimensionless modified Rayleigh number is plotted against the cooling rates in K/h. The critical Rayleigh number Ra_c (1100) is also shown.

Based on these parameters, we can see that the minimum cooling rate for the instability to set in is lies in the order of 1K/h, which is consistent with our experimental results.

Recently, Dr. Hayase performed detailed numerical study of the problem [40]. She found in her simulations that convective instability can occur even in the absence of latent heat or a temperature bias. The simulations were done assuming identical cooling from both top and bottom of the cell. When the cooling rate is sufficient, the middle of the sample would be relatively hotter than either top or bottom. She found three scenarios in her simulations. First, if the cooling rates are relatively very low, no patterns are seen. For intermediate cooling rates, convective instability is seen with regular patterns. For higher cooling rates, complex patterns emerge. The patterns are not system spanning. The simulations with latent heat contribution also show similar convective patterns. The simulation results are consistent and in good agreement with our experimental results. The

2-butoxyethanol/water/decane system:

For the 2-butoxyethanol/water/decane system we can again compute the Rayleigh number with the following estimated values. The values of α, κ and v are the weighted averages of that of the components.

$\alpha = 9.1 \cdot 10^{-4} K^{-1}$

$v = 2.4 \cdot 10^{-6} m^2 / s$

$\kappa = 1.1 \cdot 10^{-7} m^2 / s$

For a heating rate of 1K/h, taking the value of g to be $9.8 m / s^2$, and taking our cell height d=1.1cm, we get the modified Rayleigh number for the butoxyethanol/water system to be:

$Ra* = 200 \ (\pm 100)$

This is far less than the critical value of 1100. Infact the the value of d should be smaller than 1.1 cm, since we see patterns after a meniscus is formed. This would further lower the modified Rayleigh number. This low value can be understood from the values of α and v in comparison with those of the methanol/hexane system. In this system, α is comparatively smaller and v is comparatively greater than those in the methanol/hexane system.

The dependence of Rayleigh number on the heating rate for this system can be seen from following plot [Fig. 4.17].
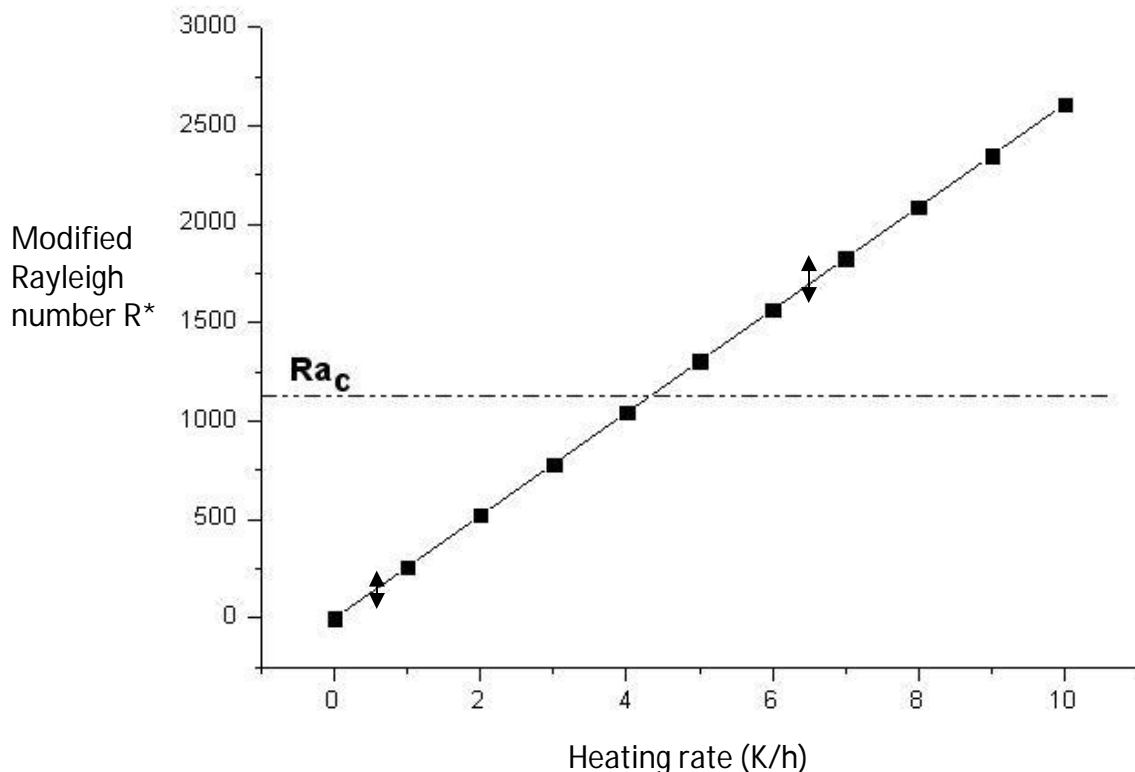
Fig. 4.17

Plot showing the dependence of modified Rayleigh number on the heating rate for the butoxyethanol-water-decane system, for a sample thickness of 1.07($\pm$0.02) *cm. The error is approx* $\pm$ *100 for very low heating rates, and approx.* $\pm$ *200 for higher heating rates.*

Based on these parameters, we can see that the minimum heating rate for the RB instability to set in is around a few K/h.

But we see patterns in this system at approx: 0.5K/h.. This is almost an order of magnitude less than the critical heating rate for the RB instability. This means that the reasons for these patterns should be different than the RB instability. The fact that we see a lengthened turbid period before the patterns emerge suggests that there is already a meniscus formed separating two phases, differing in their relative compositions of butoxyethanol and water. And surface tension differences at this liquid-liquid interface is known to produce Marangoni convection, which also show similar patterns.

As a comparison, while a convective instability similar to RB convection can easily set in the methanol/hexane system, it is almost impossible for that to happen in the butoxyethanol/water system in our experimental setup. This marks a decisive indication that although patterns appear in both systems, their origins must be attributed to different causes.

OUTLOOK
Dependence of Rayleigh number on the cell thickness

Although in our experimental setup, we had a fixed cell thickness, we know that the modified Rayleigh number depends on this thickness. The modified Rayleigh number is given by eqn. (4.16) and we have ΔT given by eqn. (4.15).

Combining these two equations results in:

$$Ra^* := \frac{g\alpha\gamma}{64.\nu\kappa^2}d^5 - \frac{5}{32}\frac{g\alpha.Tb.}{\nu\kappa}d^3 + \frac{5}{8}\frac{g\alpha.Tb^2}{\nu\gamma}d - \frac{5}{4}\frac{g\alpha\kappa.Tb^3}{\nu\gamma^2 d} + \frac{5}{4}\frac{g\alpha\kappa^2 Tb^4}{\nu\gamma^3 d^3} - \frac{1}{2}\frac{g\alpha\kappa^3 Tb^5}{\nu\gamma^4 d^5}$$

Thus, *Ra** depends on the fifth power of the cell thickness. This strong dependence can be visualized from the following plot [Fig.4.18], for the methanol/hexane system, at a cooling rate of 1K/h:
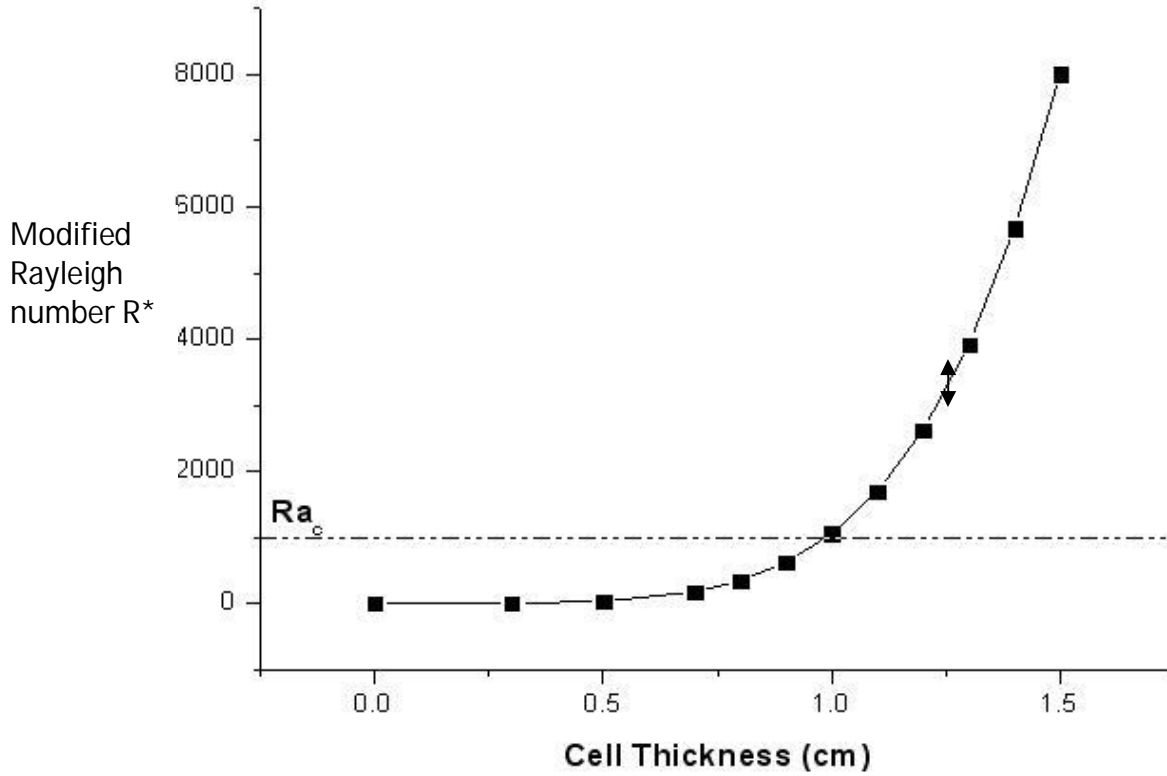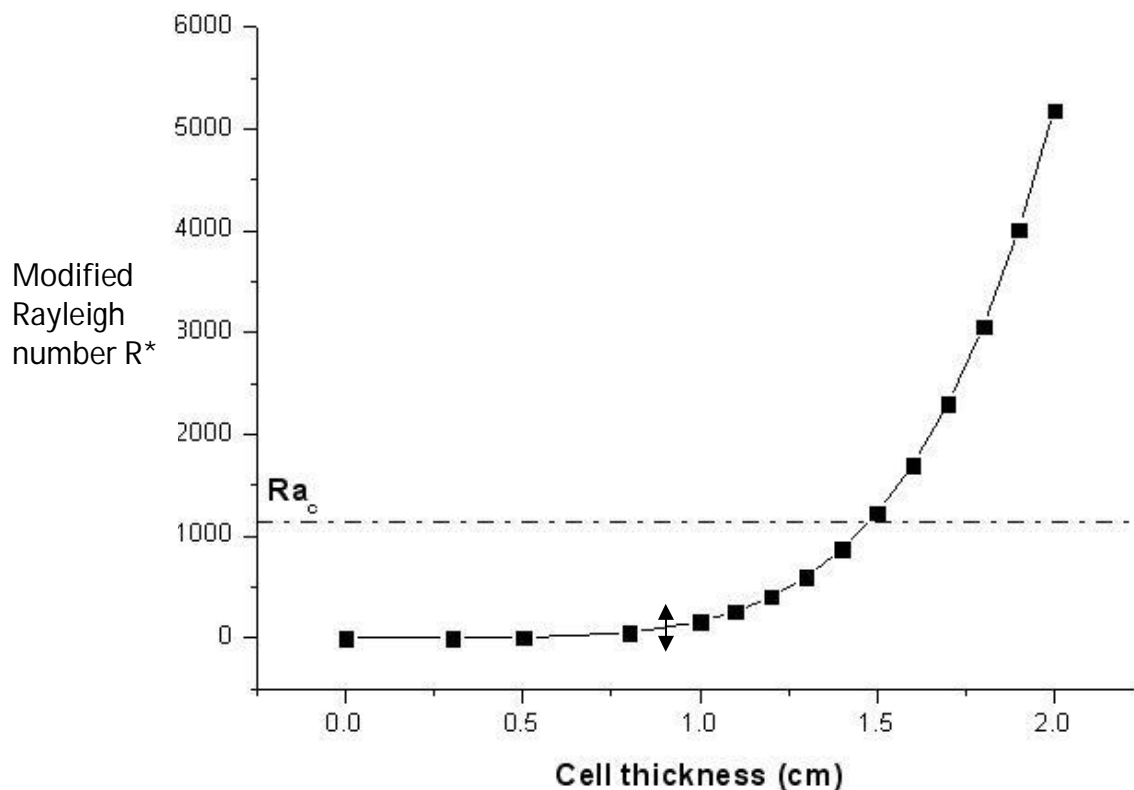
Fig. 4.18

Dependence of modified Rayleigh number on the thickness of the sample cell, for a cooling rate of 1K/h in the methanol-hexane-ethanol system. Our sample cell has a thickness greater than what is necessary for Rayleigh-Bénard instability, for the above set of parameters. The plot predicts that RB instability can be suppressed in this system, for a smaller sample cell thickness than the present setup.

A similar plot can be done for the butoxyethanol/water system at a heating rate of 1K/h, as seen in Fig. 4.19.

Fig. 4.19
Dependence of modified Rayleigh number on the thickness of the sample cell, for a heating rate of 1K/h in the butoxyethanol-water-decane system. The plot predicts a Rayleigh-Bénard instability for this system, for a larger sample cell thickness than the present setup.

We have a cell thickness of 1.07cm ($\pm\,0.02$ cm). It can be seen from the figure that Rayleigh numbers at this thickness for the 2-butoxyethanol/water system, for this cooling rate of 1K/h (where we actually see patterns already), are quite lower than the critical Rayleigh number. But it is interesting to note that there is a possibility of RB instability in this system at higher cell thickness, $\approx > 1.5$ cm. Presently, we have not verified these estimations, since in our present setup we can work only at a fixed cell thickness. Different setups employing different cell thicknesses should give more insight into how close the experiments match with the predictions made here.

Chapter 5

OSCILLATIONS DURING PHASE SEPARATION

The kinetics of phase separation is a topic of continuous experimental and theoretical interest [15, 27, 41-51]. In binary liquids, it strongly depends on the values of diffusion coefficient, surface tension and viscosity. The dynamics of phase separation depends also on the thermal protocol used, whether phase separation is induced by a temperature quench or by slow continuous ramping. Although many studies were done on systems quenched rapidly from one phase to two phase region, studies concerning systems ramped slowly in temperature were relatively few. Considering the fact that in many industrial and natural processes, temperature changes are gradual and slow rather than being quenches, studies using such a protocol assumes significance.

Oscillatory phase separation in binary liquids

It was observed by Vollmer et.al [4, 43, 52-56] that in binary liquids where phase separation was induced by slowly ramping the temperature, there were oscillations in turbidity and apparent heat capacity. These were not limited to a particular mixture, but found in a variety of them, for example in methanol/hexane mixture, polystyrene/cyclohexane mixture etc.

The binary mixture (for example, methanol/hexane mixture) was prepared by adding appropriate amounts of the components. The mixture was homogenized in the one phase region. The phase diagram of the methanol/hexane system is shown in Fig.1.1

The mixture was then slowly cooled down into the two phase region by continuous ramping, keeping the pressure constant. The sample was placed in a transparent water bath. The water temperature was controlled by a Haake thermostat to an accuracy better than 0.1K. The detailed temperature protocol was followed automatically and the temperature setting was recorded together with optical data. The mixtures were loaded into teflon-sealed fluorescence cuvettes, and homogenized prior to every experiment[1]. Thereafter the turbidity of the sample was observed, by capturing the scattered light from the sample using video microscopy.

When the sample was in the one phase region, the setup was adjusted such that no light entered the camera. At the onset of phase separation, droplets were formed, which scattered the light into the camera. Thus turbidity denoted the presence of droplets inside the sample whereas a clear image indicated their absence.

To analyse the videos obtained during the experiment, space-time plots were constructed as in Fig. 5.1. The horizontal turbidity of each video image was averaged onto one line along the height of the sample. This line of pixels represents the vertical distribution of a horizontal average of the turbidity at a given instant of time. Thereafter, these turbidity distributions were written into a new image such that the experimental time increased from the left to the right. The dark areas correspond to periods in which the sample was transparent and bright areas to turbid periods.
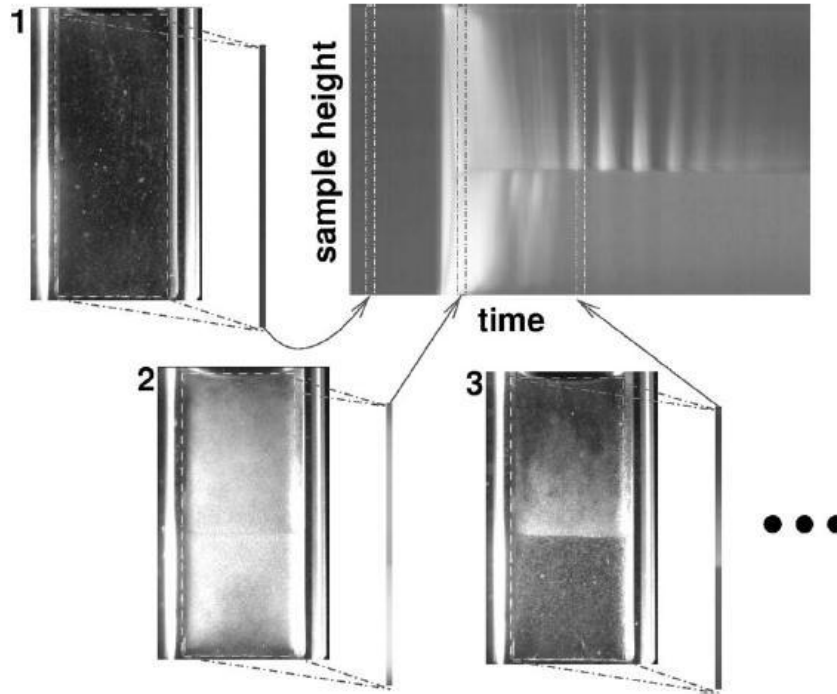
Fig. 5.1

Space-time plot of methanol-hexane mixture ($\varphi_{meth} \cong 30\%$) under continuous cooling rate of 10 K/h. They are constructed by determining the average gray scale in horizontal direction for each single picture of the video. The space-time plot is then obtained by assembling these vertical lines of pixels to one new picture. The frames numbered 1,2 and 3 are used to show schematically the construction of space-time plot. The dark part in the beginning of the experiment represents the cooling of the homogenous sample until phase separation sets in. {Fig. courtesy: Reference [52]}

From the space time plot, one can see an initial dark area, which indicates that the system was in the one phase region. As time proceeded, with cooling, the plot shows the first turbid areas, which indicate the onset of phase separation. Furthermore, we can see subsequent turbid and clear periods in the plot.

Mechanism of oscillations

The densities of methanol and hexane (at 20°C) are respectively 0.787 gm/cm^3 and 0.656 gm/cm^3. When the system is in one phase region, the average density of the binary mixture remains a constant at constant temperature. As the cloud point curve is crossed, droplets, relatively rich in either methanol or hexane, are formed throughout the sample. The equilibrium concentration is given by the phase diagram. These nuclei of droplets grow in size, merge and when they are sufficiently large, gravity affects them. Hexane-rich droplets being relatively less dense move upwards and methanol-rich droplets being relatively denser move downwards, due to gravity. This forms the sedimentation process. The growth of the droplets and their sedimentation is reflected in

the scattered light as a turbidity. When the droplets have sedimented, and a meniscus formed, turbidity ceases, and there is little scattered light. This marks the initial cycle of phase separation. The equilibrated phases have a relative concentration of methanol and hexane which can be calculated from the phase diagram, once we know the temperature of the sample. A sketch of a phase diagram with two components A and B is shown below. [Fig. 5.2].
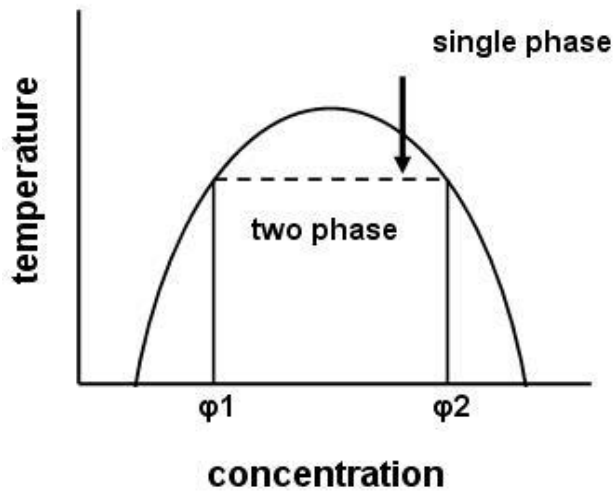

Fig. 5.2
Plot showing the relative concentrations in the two phases at a given temperature. The equilibrium concentration of component A in the phase where it's in minority is φ1 and that in the A-rich phase is φ2. Corresponding concentrations of B in those phases would be (1- φ1) and (1- φ2) respectively.

After the initial tubidity (corresponding to the formation and growth of droplets), and clearing of the turbidity (sedimentation of droplets), the two phases would differ in their relative concentrations. The hexane rich phase would have a methanol concentration of φ1 whereas the methanol rich phase would have a methanol concentration of φ2.

If we further cool down, hardly any formation of droplets takes place until the energy barrier for their formation is crossed. Once the temperature corresponding to the energy of nucleation is reached again, new droplets are formed in both phases. They grow, coalesce and when they are large enough for gravity to take effect, they sediment. Thus the next cycle of turbidity is exhibited. Upon continuous cooling, this oscillation in turbidity continues.

Complimentarily, differential scanning calorimetric (DSC) measurements were also used to study the kinetics of phase separation in the same system. The system is cooled at a constant rate. In each small time interval the temperature of the sample is

changed by the same, typically small amount. The resulting thermogram for (a) methanol/hexane mixture and (b) polystyrene/cyclohexane mixture are shown in Fig. 5.3
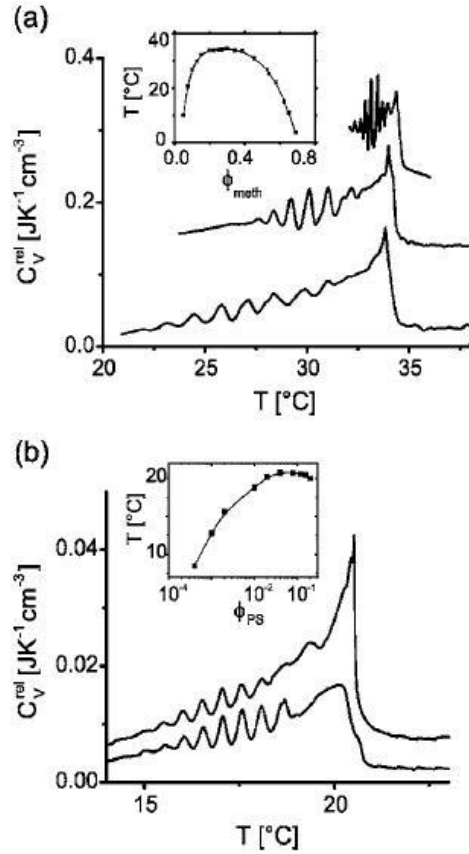

Fig. 5.3
Thermograms of (a)methanol/hexane and (b)polystyrene/cyclohexane system. The first peak in the thermogram denotes the onset of phase separation. Subsequent peaks denote the oscillatory instability.
{Fig. courtesy: Reference [52]}

The shapes of the thermograms strongly resemble each other. In the single phase region $C_v^{rel}(T)$ is almost constant as a function of temperature. Passing the phase boundary between single phase and the two phase region causes a pronounced step in the thermogram. It reflects the heat involved in the formation of the coexisting phases. Further cooling leads to an oscillatory change in the signal. This is similar to the observation of oscillations in turbidity in the optical setup. Typically five to seven oscillations could be discerned from the thermogram signals. Eventually, fluctuations in $C_v^{rel}(T)$ leveled out.

From Fig. 5.1, one can define a period for the oscillations of turbidity as the time between two successive peaks in turbidity. This coexists with the time interval between successive peaks in the $C_v^{rel}(T)$ also. It was found that the period does not depend on the

relative concentration of the components of the binary mixture. Fig. 5.4 shows the dependence of period on the concentration of the sample.
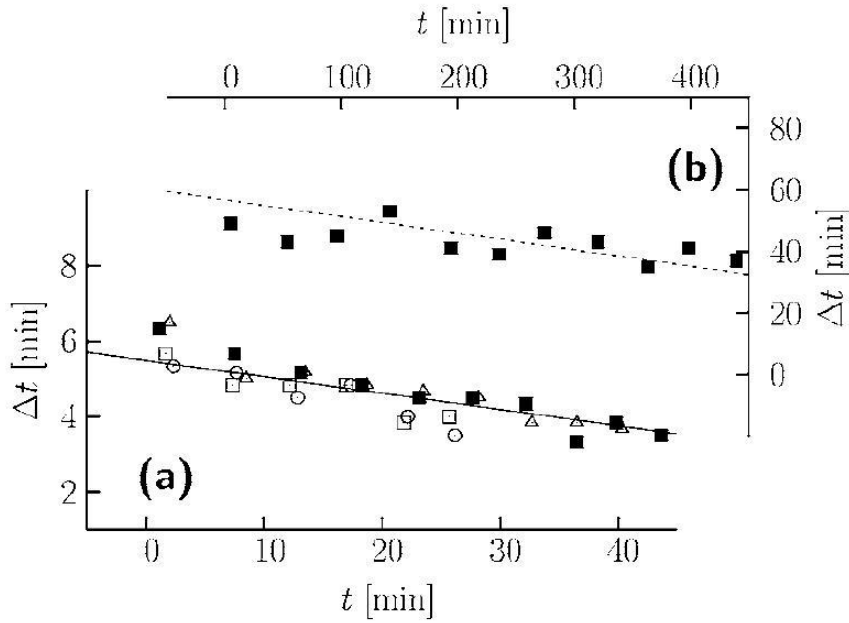

Fig. 5.4
Plot showing the concentration dependence of period.
{Fig. courtesy: Reference [52]}

Fig 5.4(a) shows the plot of period against time for 3 different methanol concentrations: 0.221, 0.245, 0.270 and 0.304, in the methanol/hexane binary mixture. Fig 5.4(b) shows the plot of period vs temperature for the polystyrene/cyclohexane mixture with polystyrene concentration: 0.04, with molecular weight $Mw = 100,000 \ g / mol$.

In short, we see that when a binary mixture is subject to a temperature change from a homogenous state beyond the binodal, it phase separates into two phases. On further change of temperature in a slow and steady manner, oscillations occur, denoting the exchange of material between the two phases. The oscillations are almost periodic, and we can ascribe a characteristic period for definite experimental conditions. Theoretical works, understanding the oscillatory phenomenon has also been done [3, 43]. We saw that three mechanisms are to be considered in the process. (a) Nucleation of minority phase droplets in the majority phase (b) growth and coalescence of these droplets and (c) their subsequent sedimentation. The period of oscillations, therefore, must be connected to the time scales associated with these three processes. Earlier work on low molecular mixtures like methanol/hexane had assumed that the time scales of sedimentation were negligible compared to that of nucleation and growth [43]. Our aim is to study how the time scale of sedimentation matches against that of nucleation and

growth in polymer mixtures. If the time scales associated with sedimentation are important relative to that of nucleation and growth, then a carefully designed experiment should show it. One method to test this is by taking similar samples of a definite composition of a mixture with different sample heights. Since gravity determines droplet sedimentation, similar samples at different heights must have different times for the droplets to sediment. Thus, one would expect to see different periods of turbidity in samples at different heights.

Chapter 6

EXPERIMENTAL SETUP

Sample Cell

A photograph of a typical sample cell is given below [Fig. 6.1a]. The cell has an inner diameter of 1.6($\pm$0.1) cm. The shorter cells have a height of 9cm, and the longer cells go up to 18cm. The height of the sample taken differs depending upon the experimental needs.

Water bath and Thermostat

In order to control the temperature of the sample, a water bath and a combination of a heating and cooling device is used. The dimensions of the water bath are 40 x 16 x 14 cm. It is made from Plexiglass. The sample cells are placed closely in parallel inside the water bath, ensuring a homogenous temperature (or similar changes) for them. A photograph of the setup is shown below [Fig. 6.1b].
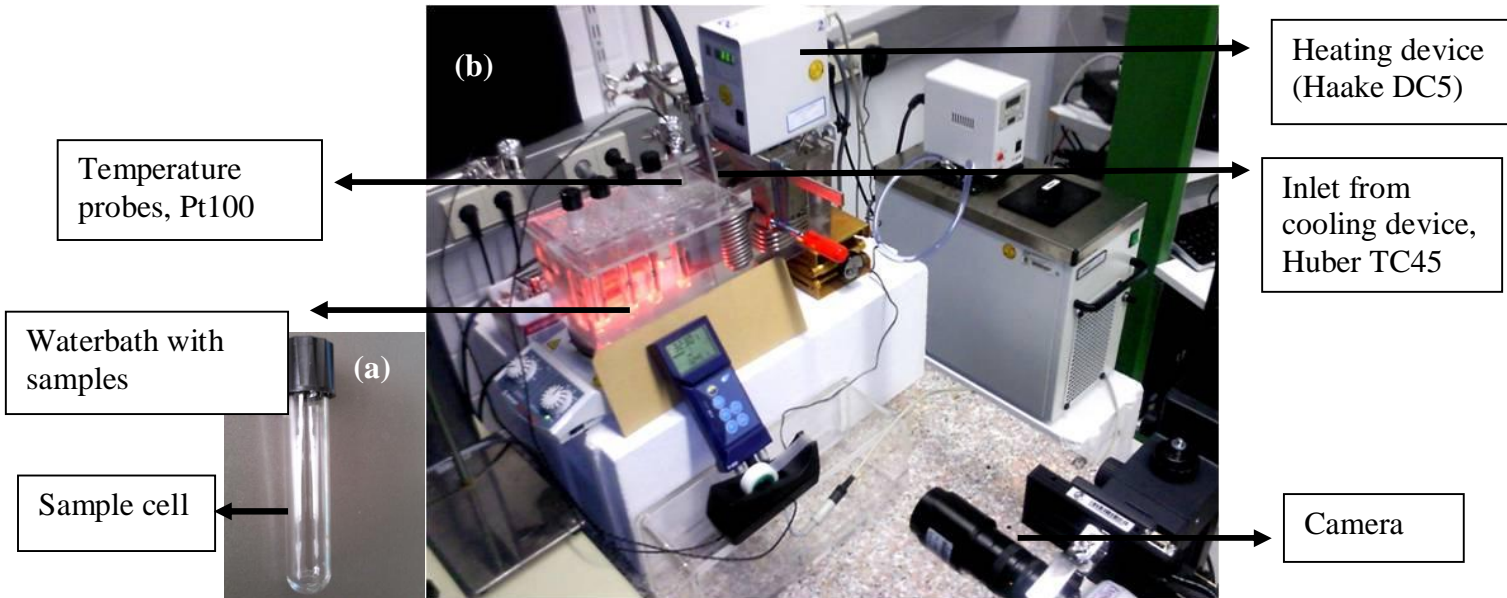
Fig. 6.1

Photograph of the experimental setup: Sample cells are placed in parallel inside the waterbath. The temperature inside the bath is controlled using a heating device Haake DC5 and a cooling device Huber TC45 using a computer interface. The waterbath is illuminated by an array of LED's from behind. Light scattering video microscopy is used.

The heating device we use is Haake DC5, and Huber TC45 is the cooling device. The combination can cool or heat at various rates from below 0.1K/h to above 20K/h.

The cooling rate is monitored using a computer interface. The temperature is measured using two Pt100 probes. The experiment is recorded using a CCD camera at definite time intervals. We use Image Pro Plus software for data acquisition and subsequent analysis.

The basic idea we employ in tracking the experiment is light scattering method. Light from the sources are pointed in such a way that no direct light enters the camera. When, for example droplets are formed within the sample, light gets scattered. This scattered light is then captured by the camera. Essentially, the optimal condition would be to have no direct light at all, and to have maximum intensity when scattering occurs.

Each of light sources is an array of high intensity red LEDs. The array of LEDs were purchased from Weiss Imaging and Solutions GmbH. Each array consists of 10 LEDs, with a total output power of approx 50 watts

SAMPLES

In deciding which mixture to use, we had a few considerations. Firstly, the phase transition temperature would be desirable around room temperature (between 20˚C and 50˚C). This is practically advantageous, since a very high transition temperature would imply heating the water bath to a high temperature, thus involving problems of water evaporation etc. A very low transition temperature is also not recommended since for the experiments involving oscillations, we need to continuously cool the sample down by 15 or 20 K. Again, if the end temperature is below 10˚C, we observed that water droplets begin to condense on the waterbath, thus resulting obscure images.

Secondly, the sample should have a reasonable optical contrast to infer any useful data from the video microscopy. This led us to choose a mixture of polystyrene (molecular weight 40,000g/mol) + methylcyclohexane.

The phase diagram of PS(40,000)/methylcyclohexane mixture is shown in [Fig.6.2].
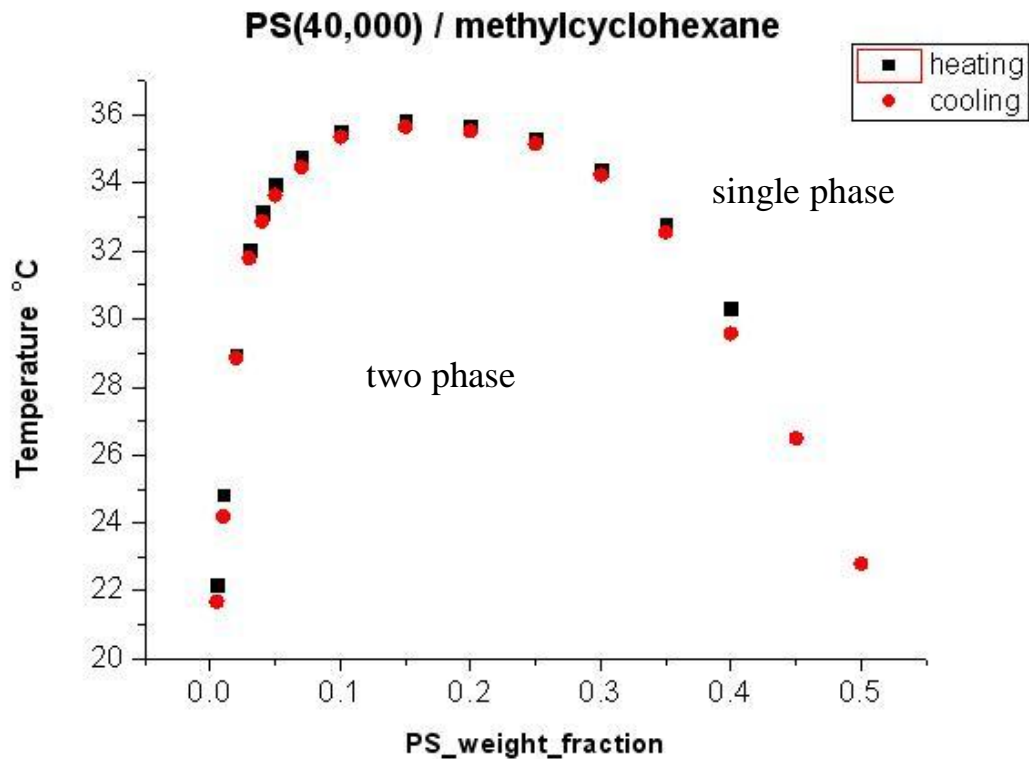
Fig 6.2

Phase diagram of PS(40K)/methylcyclohexane mixture. The squares indicate the measured data points on heating, and the circles that on cooling. The errors are within the square and circle sizes.

The phase diagram was obtained as follows. Defined amounts of polystyrene were mixed with methylcyclohexane in the sample cell. 16 samples were prepared with varying mass ratio of PS:methylcyclohexane, ranging from 1:99 to 50:50. Each cell was provided with a magnetic stirrer, to help homogenize the sample during the experiment. The samples were continuosly cooled from temperature corresponding to a homogenous state to below the point where they became turbid. This point of first turbid appearance was taken as the phase transition temperature on cooling. These correspond to the circles on the graph. Once the sample was allowed to be in the demixed state for a long period, a meniscus appeared thereby separating the two phases.

To measure the phase transition temperature on heating, all samples were heated with stirring from the two phase region. Due to continuous stirring, the sample remained turbid throughout, until the phase transition temperature was reached. The temperature corresponding to the clearing of the sample was taken as the phase transition temperature on heating.

Chapter 7

DISCUSSION & RESULTS

The binary mixture we took for our investigation is polystyrene (molecular weight 40,000g/mol) mixed with methylcyclohexane. The phase diagram for this mixture is shown in [Fig 6.3]. We decided on a relative composition of PS:C_7H_{14} = 8:92 (mass ratio) for our first experiments. The mixture was prepared as a homogenized stock, and then distributed into three equivalent sample cells, in varying heights of 1.8cm, 3.1cm, and 8.1cm. [Fig 7.1] shows the sample cells with the mixture.
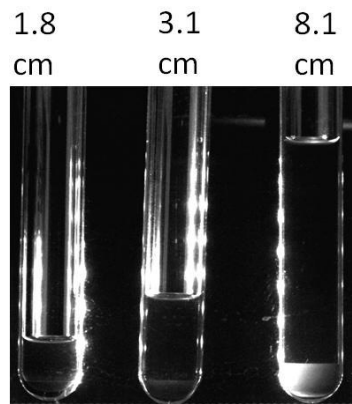

Fig 7.1
*A mixture of polystyrene (8% wt) mixed with
Methylcyclohexane taken in three sample heights of
1.8cm, 3.1cm and 8.1cm.*

The sample was pre-cooled to just below the phase transition temperature (~0.5^{o}C below). We did not start the experiment straight away from the one-phase region, since we didn't want any sedimentation time scales of the first phase separation to mix with that of the oscillations. Also, viscoelastic phase separation [see Ch.1], has a chance to occur only just below the binodal. Viscoelastic phase separation needs the polymer chains to entangle, and in our system the polymer concentration for entanglement, if any, will only be for the first phase separation, where the overall polymer weight fraction is not negligibly small. Once the system phase separates, the polymer concentration in the upper part of the meniscus has relatively small fraction of polystyrene, which will not be sufficient for any entanglement. The polymer concentration at a particular temperature can be found from the phase diagram. The following [Fig 7.2] shows that all the three samples turn turbid at the same temperature of 34.21 (±0.02) ^{o}C.
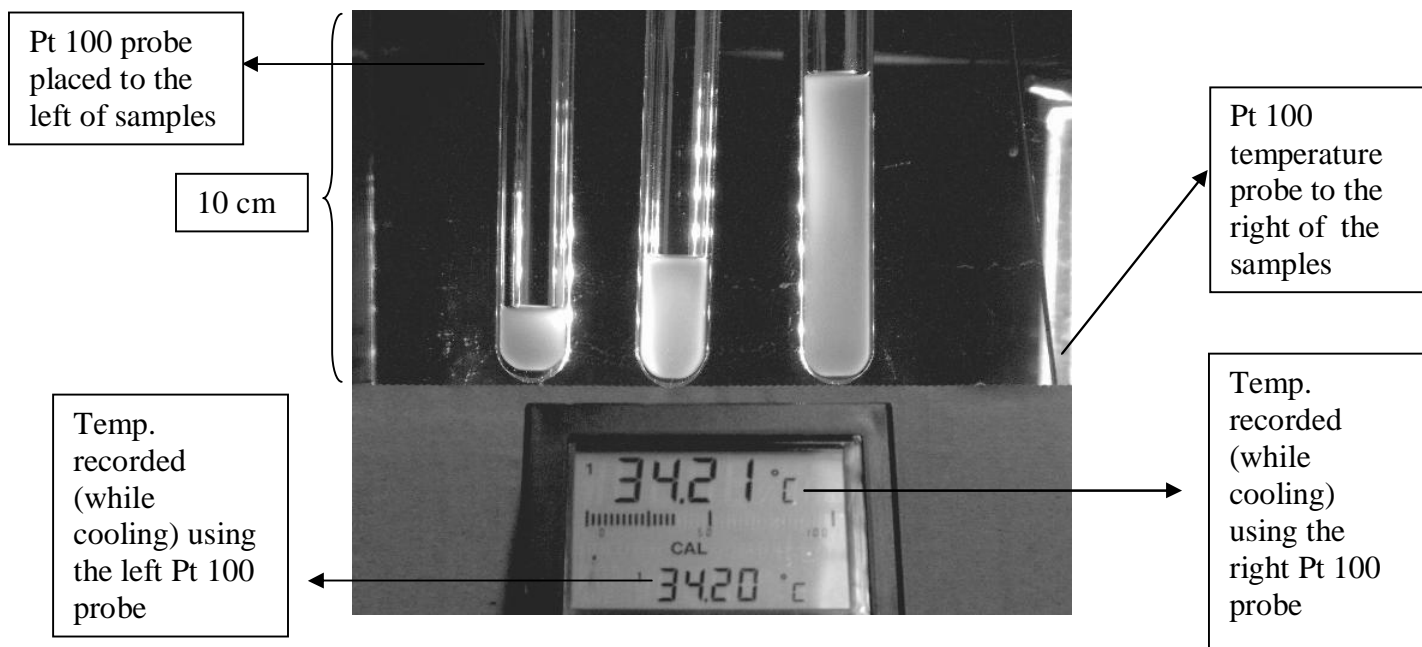
Fig 7.2

All three samples become turbid simultaneously, showing that they are identical in composition. The temperature is measured by two Pt100 probes kept on either sides of the samples. The water bath is homogenous in temperature within 10 to 20 millikelvins.

The fact that all three samples phase separate at the same temperature shows that the relative composition of the constituents is the same in all three samples. Any experimental result should thus be independent of composition of the mixture. The two temperatures shown are those measured by two Pt100 sensors placed at two ends, and at two different heights, one near the bottom of the rightmost cell, and one near the top of the leftmost cell. The samples are being cooled continuously at a rate of 4K/h. We see that the temperature inside the water bath is homogenous to a few hundredths of a Kelvin. This should be sufficient to disregard any artifacts arising due to temperature differences inside the bath.

The setup uses two arrays of LED light sources, aligned vertically, that illuminate the setup from two sides, from behind. They are arranged to illuminate the three cells from either side, and such that no direct light falls into the camera. This resulted in slight inhomogenity of the incident light on the three sample cells. The resulting horizontal gradient in illumination is what is seen in the figure.

Once the samples are pre-cooled to half a degree below the phase transition temperature, they are allowed to sediment fully. We give a waiting time of about 3 hours. After that, the two phases can be seen separated by a macroscopic interface. Polystyrene being denser forms the lower phase and methylcyclohexane, the upper. Meniscus in the samples can be seen in fig [7.1]

After this waiting time for sedimentation, we cooled the sample continuously. We saw oscillations in the samples as expected, but the oscillations were not simultaneous. Each sample oscillated at different times, thus being out of phase with each other.

The following sequence [Fig 7.3] shows some of the frames of an experiment with a cooling rate of 4K/h.
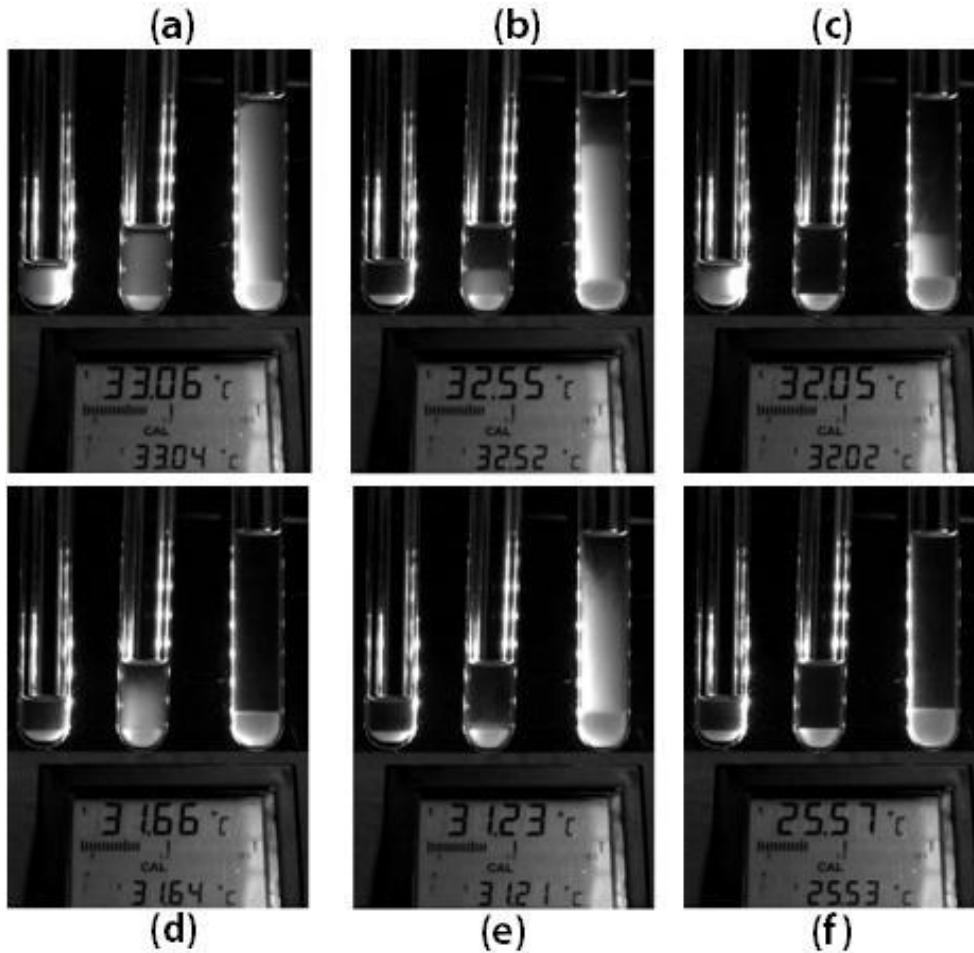

Fig 7.3
This sequence of images shows oscillations in turbidity in the samples; PS(8%wt) mixed with methylcyclohexane, cooled at 4K/h. These images are taken at the start of cooling after a waiting time of 3 hours, when the system was left to equilibrate after the first phase transition. All three samples oscillate out of phase.

For analysis of such an experiment, we construct a space-time plot from the captured sequence of images. See {Fig 7.4}

Moving horizontally across the time axis is equivalent to continuous cooling in the real experiment. We thus see on the plot that the sample goes through successive clear and turbid periods throughout the experiment. On the lower side of the plot we also see the meniscus separating the two phases. The lower phase seems to be always bright. This is because it comprises of the dense polystyrene which scatters light intensely. Of course this lower phase also should have oscillations, but it is hard to analyze since the contrasts in scattering is so poor between the "clear" and "turbid" times. We therefore focus our analysis on the oscillations in the upper phase. The lower phase oscillations do not coincide with those of the upper phase [3]. This is because the viscosities of the two phases are different; lower phase being more viscous. The polystyrene rich phase will contain micrometer sized droplets rich in methylcyclohexane, but the viscosity of this lower (gel) phase is relatively large. It makes the diffusion of droplets slow, compared to the time scales of our experiments.

The period of oscillations can be determined from the space time plot. The following figure, [Fig 7.4] demonstrates the link between images showing successive turbid periods and the bright areas of the space-time plot.
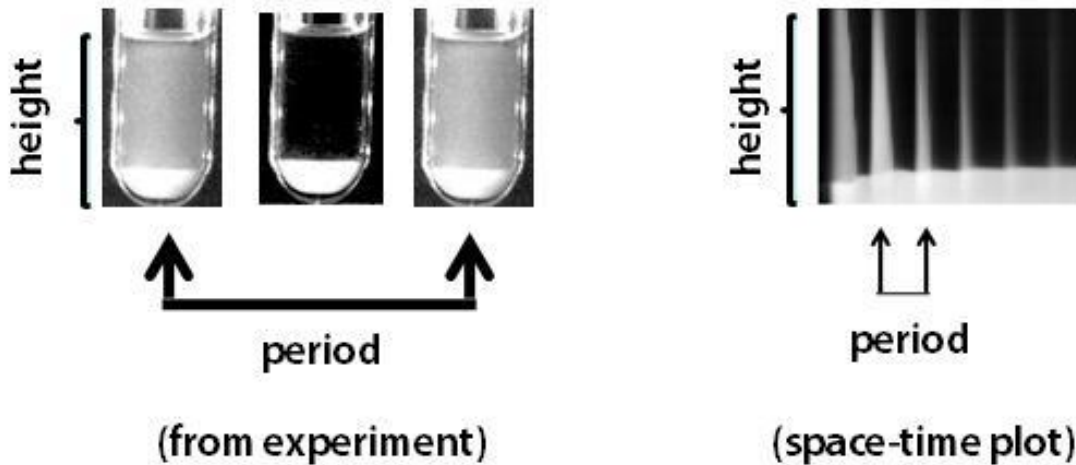
Fig 7.4
This figure shows the link between a space-time plot and the images captured during experiment.

Another way to visualize the period is by constructing an intensity graph from the space time plot. We can focus on one horizontal line spanning across the space time plot, and record the variations of intensity. A typical graph thus obtained is shown below in Fig 7.5.
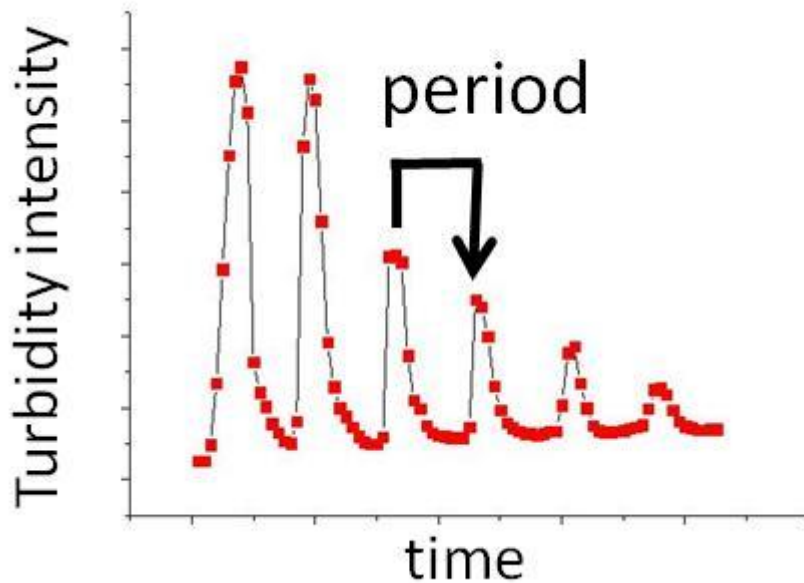

Fig 7.5
Intensity plot is another way of visualizing oscillation. The plot is done by taking the intensity values from the space-time data at any particular height in a sample.

From the graph we can measure the period between the oscillations by taking the successive peak-to-peak distance in time. Taking intensity plot has its advantages over a regular space-time plot, since the turbid period seems quite broad to the naked eye from the space-time plot. The intensity graph, on the other hand, takes precise intensity values of the pixels and shows definite peaks in intensity.

(a) Effect of sample height on the period of oscillation

We constructed space-time plots and intensity graphs for the three samples heights, 1.8cm, 3.1cm and 8.1cm which are shown in [Fig 7.6] and [Fig 7.7] respectively.
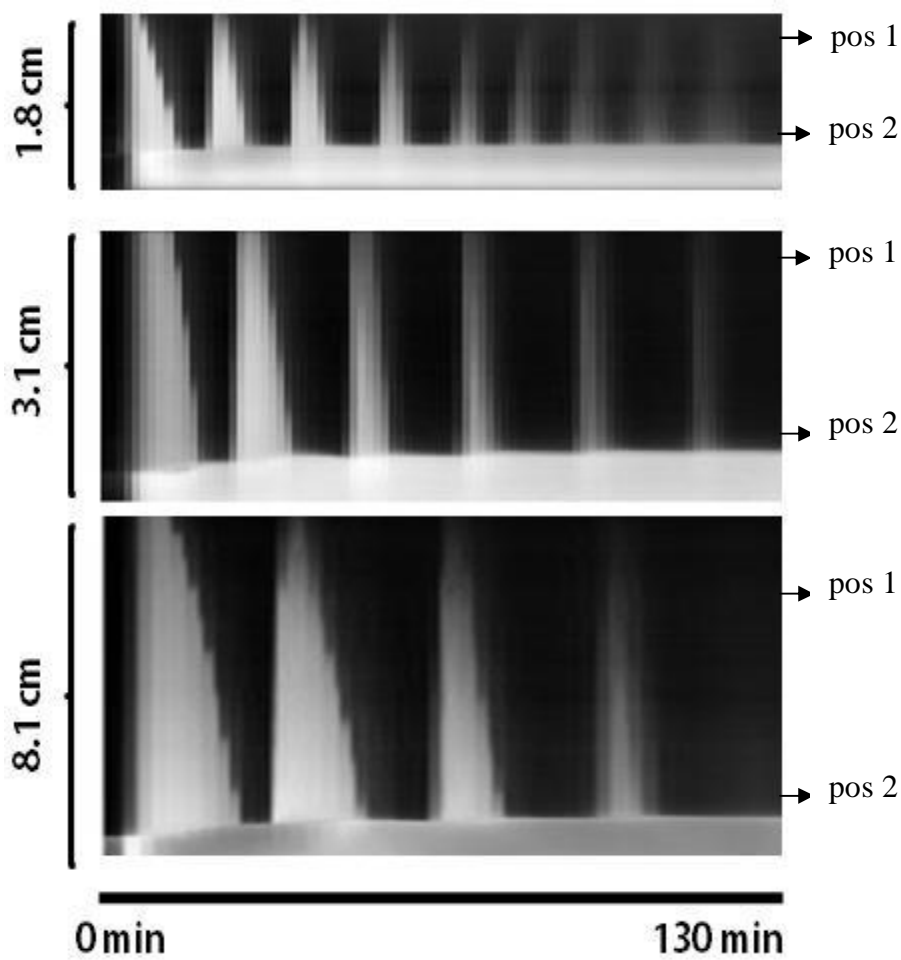

Fig 7.6

A comparison of space-time plots of different sample heights: 1.8cm, 3.1cm And 8.1cm, cooled at 4K/h. The samples oscillate out of phase. The period of oscillation is seen to increase with sample height. (pos1 and pos2 are the two positions at which intensity plots were taken to see the nature of oscillations at two heights in the same sample. See next figure)
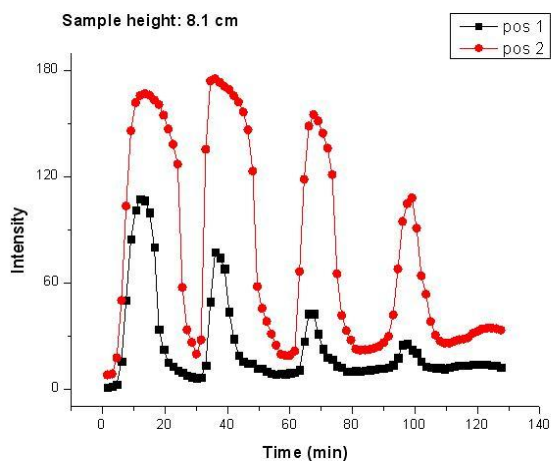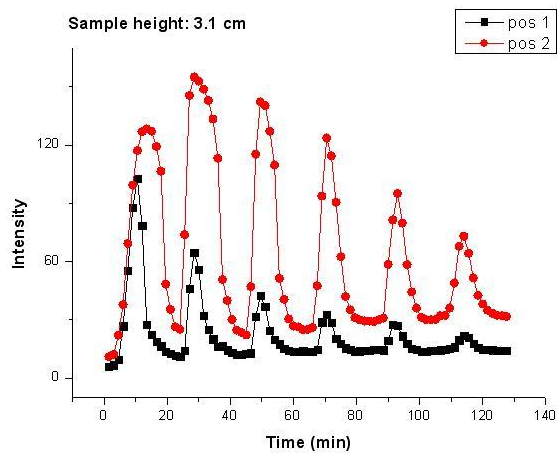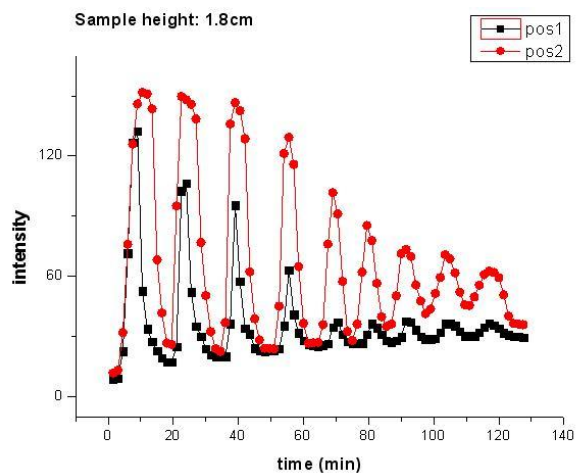
Fig 7.7

Intensity plots taken at two positions (pos1 and pos2) in each sample. The positions are marked in the previous figure.

We see that the peak-to-peak distance on the intensity graph is different for the three sample heights. The following graph, Fig [7.8], shows the period between each successive oscillation for all the three samples. The x axis, named "oscillation interval" can be understood as follows. For example, 1 on the axis refers to the period between the first and second intensity maxima; 2 refers to that between the 2nd and 3rd intensity maxima and so on. The periods taken by all the 3 samples for various intervals are shown on the y axis.
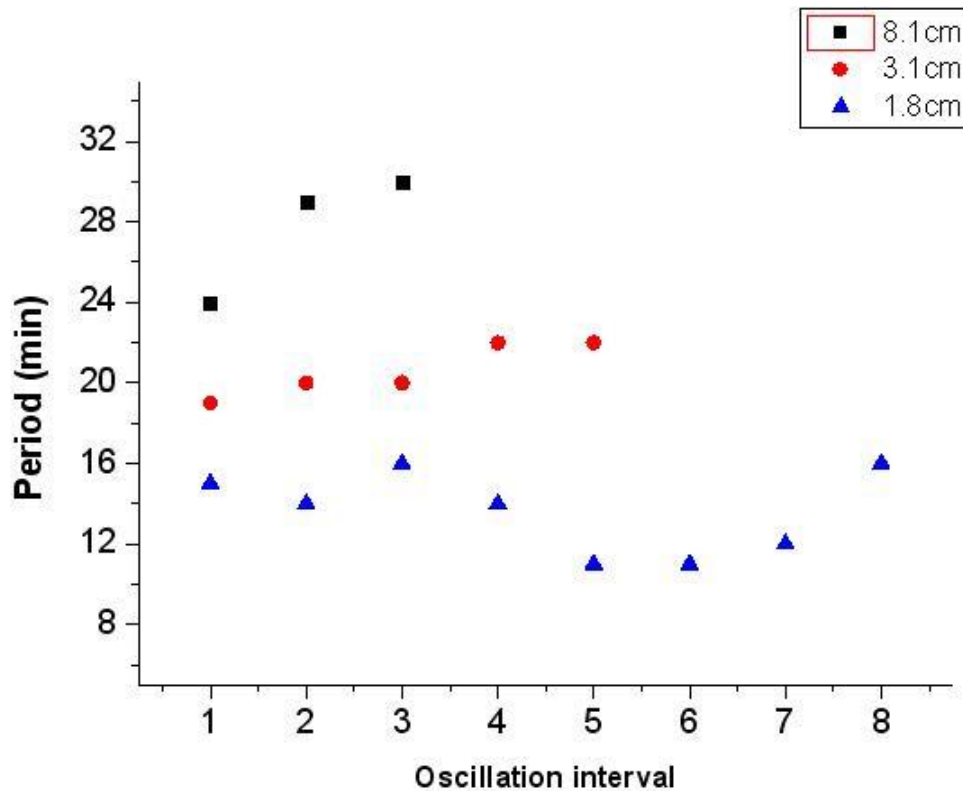

Fig 7.8

Graph showing the period between each successive oscillation for sample heights: 1.8cm, 3.1cm, 8.1cm, cooled at 4K/h. The periods increase with increasing sample height. Shows that sedimentation time determines the period.

For the smallest sample height of 1.8cm, we see that the periods centre around 14 minutes. For the sample height of 3.1cm, we have an average period of 20 minutes. For the 8.1cm sample, we see only 4 peaks. The time between the first two maxima is about 24 minutes, and that between the next peaks is approximately 30 minutes.

Later, we will go in detail examining the nature of oscillations, and discuss about why the periods change. But one thing becomes clear from the above analysis. The period of oscillations does depend on the sample height. Specifically, we see an increase of the period on increasing the sample height.

(b) Effect of cooling rate

We saw that at a cooling rate of 4K/h each sample oscillated at a different period. We wanted to know what the effect of changing the cooling rate might be, on the periods of oscillation. We now cool the set of samples at 8K/h, thus effectively doubling the cooling rate relative to the previous case. Images were captured at time intervals of 30s. Space-time plots of the system at select various times are shown below in [Fig 7.9].
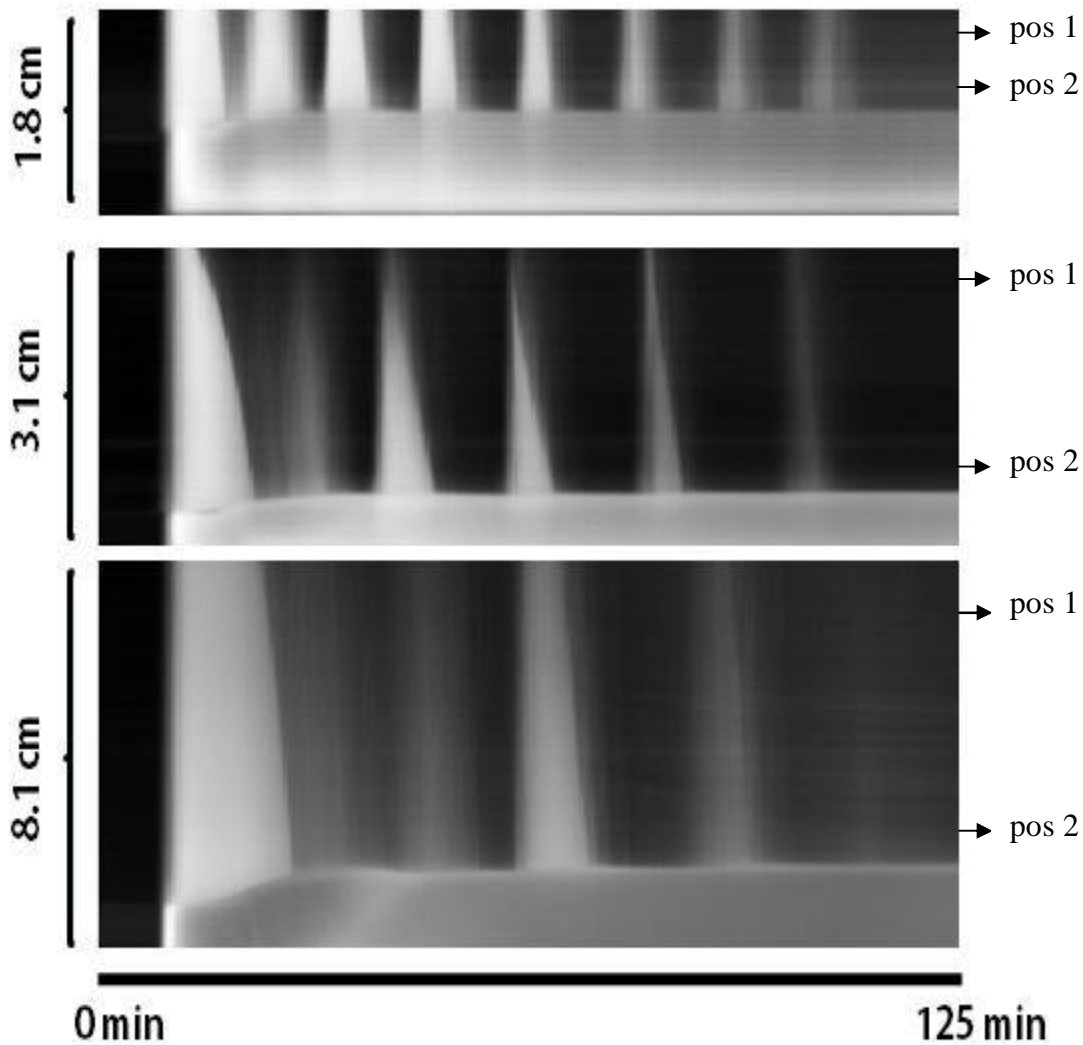

Fig 7.9

A comparison of space-time plots of different sample heights: 1.8cm, 3.1cm And 8.1cm, cooled at 8K/h. The samples oscillate out of phase. The period of oscillation is seen to increase with sample height. (pos1 and pos2 are the two positions at which intensity plots were taken to see the nature of oscillations at two heights in the same sample. See next figure)

We see that in this case too, the samples oscillate with different periods. The following figure, [Fig 7.10] shows the intensity plots for the 3 heights at a cooling rate of 8K/h
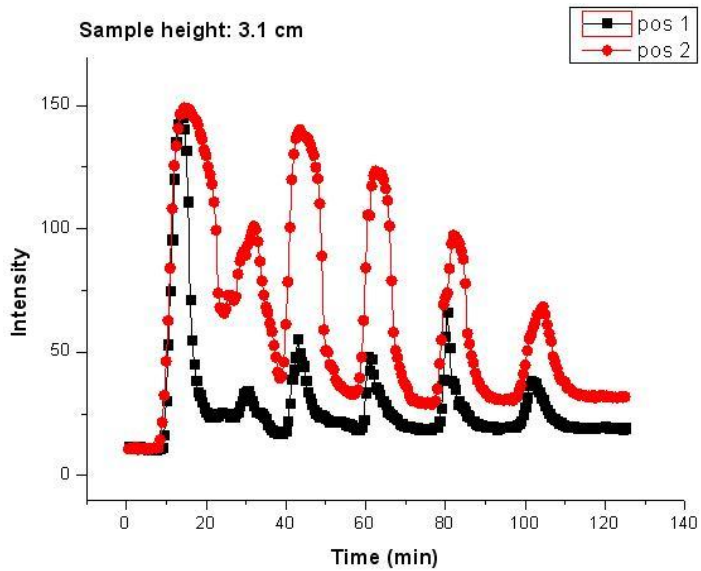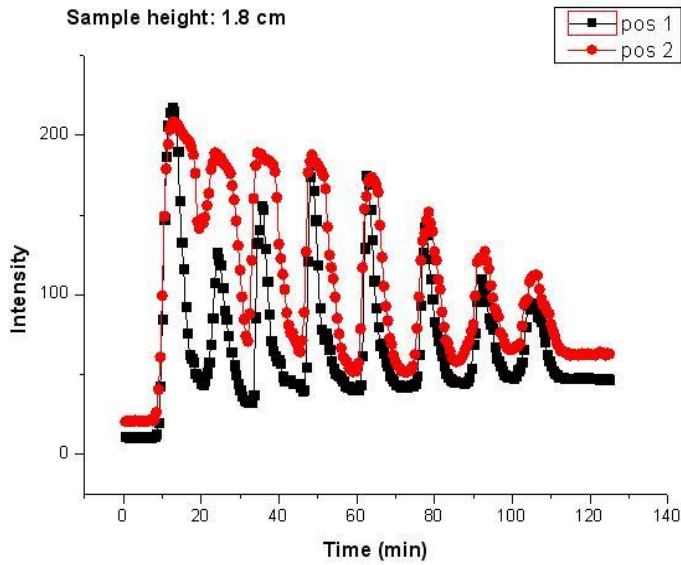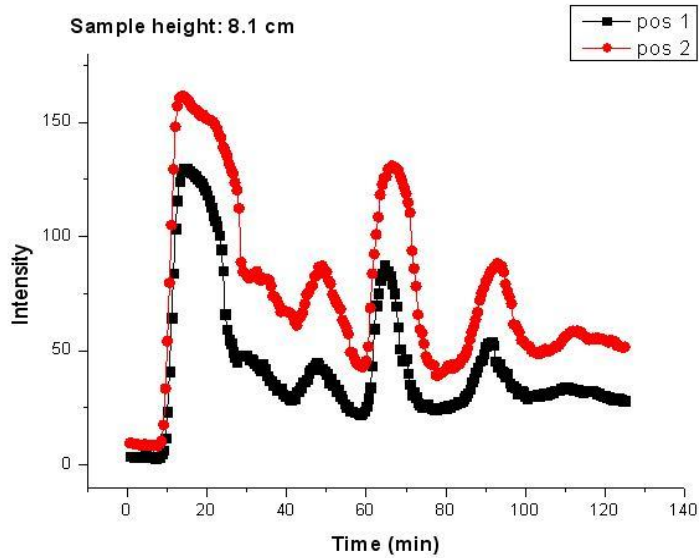
Fig 7.10

Intensity plots taken at two positions (pos1 and pos2) in each sample. The positions are marked in the previous figure.

We see that the periods increase with the sample height. The following graph, [Fig 7.11] shows the peak to peak distances between the successive maxima.
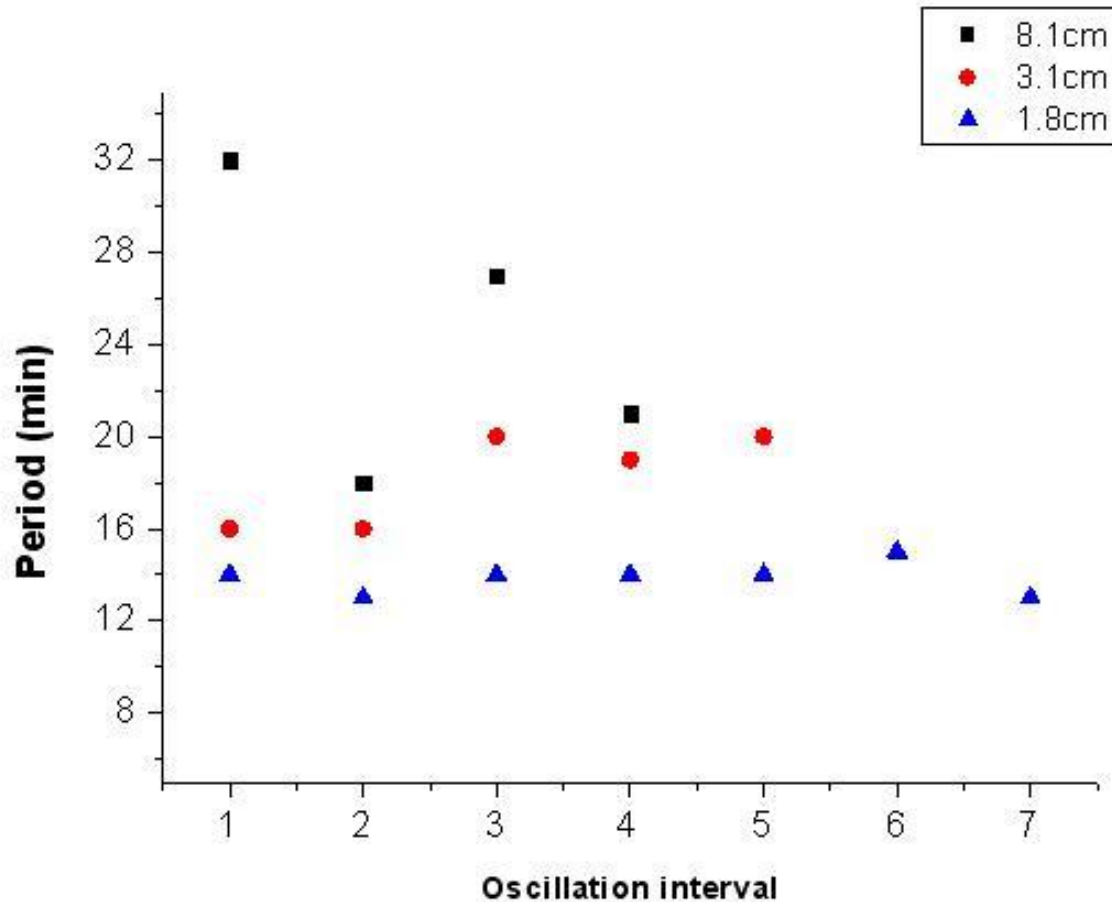
Fig 7.11

Graph showing the period between each successive oscillation for sample heights: 1.8cm, 3.1cm, 8.1cm, cooled at 8K/h. The periods increase with increasing sample height, again showing that sedimentation time determines the period.

8 oscillations can be discerned for the smallest sample height, 1.8cm. The average period centers around 14 minutes. For the sample height 3.1cm, we see 6 peaks, although the second peak has somewhat a lesser intensity than its neighbours. The first two oscillations intervals are around 16 minutes, although for the later oscillations the period increases to around 20 minutes.

For the highest sample height, things get complicated. The sample clearly shows oscillations, although the peaks are quite irregular and few. Although not much meaningful to define an average period, it's still possible to see that the distance between any two peaks is greater than the corresponding distances in the other two samples. The interval between the 3rd and the 4th peak, for example, is 27minutes.

We thus see that even though we doubled the cooling rate, the periods do not change significantly to the previous case. Comparing the graphs (previous two

comparison graphs), we find that the general characteristic still remains that the heights determine the period of oscillation.

(c) Effect of sample composition

To investigate the influence of sample composition, we lowered the polystyrene weight fraction from φ_{PS}= 8 wt% to φ_{PS}= 5 wt%. The heights were chosen so that it was closest to the set of heights we had for our previous experiments. Images were captures at 30s time intervals. Space-time plots of the system at select various times are shown below in [Fig 7.12].
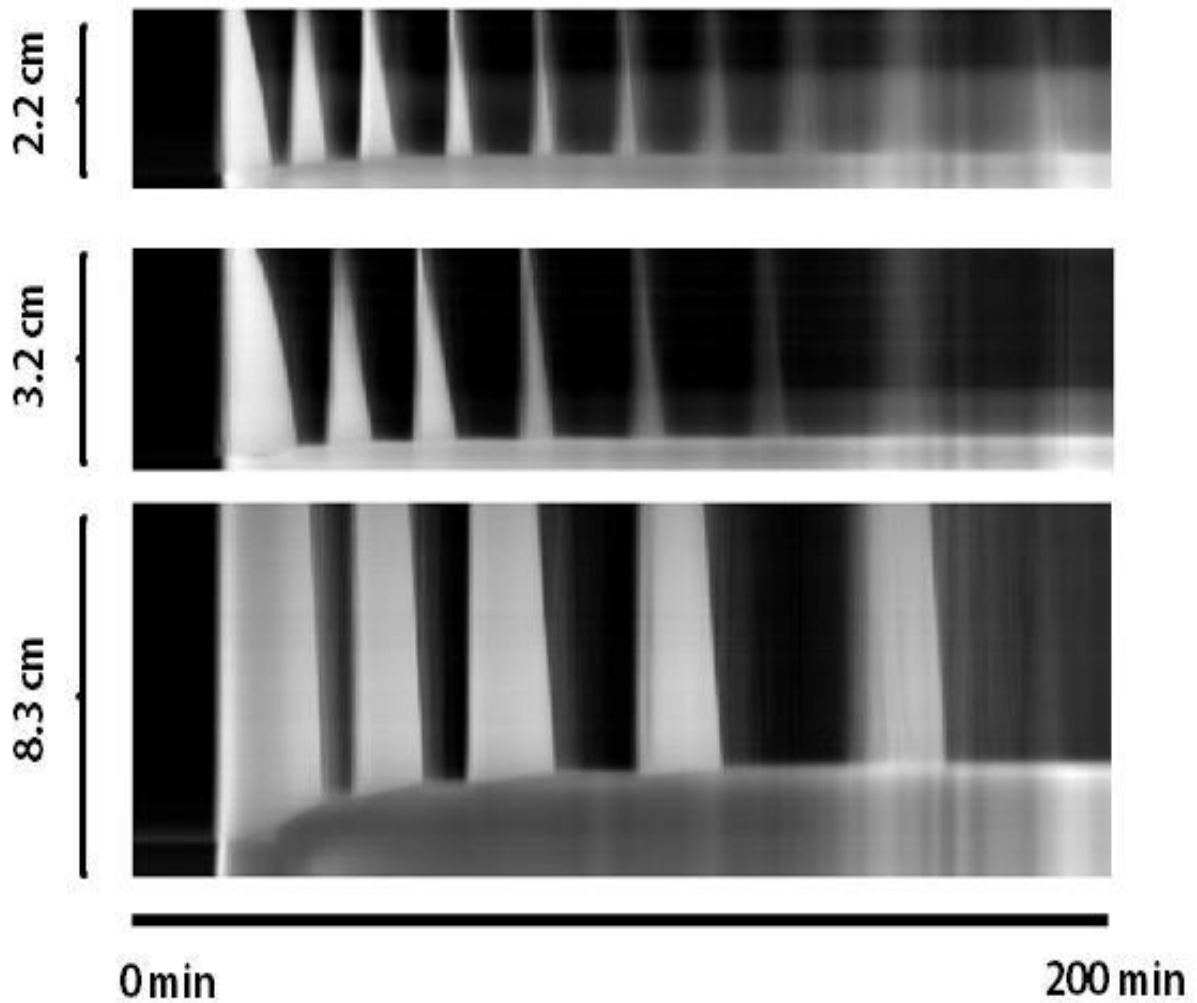

Fig 7.12

Space-time plots of three different heights: 2.2cm, 3.2cm, 8.3cm of the system PS (5 wt%) mixed in methylcyclohexane. The periods increase with sample height.

Here again, we see that the samples oscillate out of phase with each other. We can see that the period of oscillations increase as the sample height increases. For a sample height of 2.2 cm, an average peak to peak time distance is approximately 15 minutes. For the medium cell height of 3.2cm, taking the average of the initial 5 peak-to-peak distance yields approximately 20 minutes in the period. Again, it should be noted that the period changed towards the latter stages of the phase separation. This fact is considered in detail later, where we focus on the nature of oscillations and its different regimes. For the sample height at 8.3 cm, the average period is approximately 30 min.

Although we changed the composition of the sample, the behavior of the periods scaling with the sample height show remarkable similarities. For both compositions, the period of oscillations increases with increase in sample height.

We thus see that although the cooling rates and composition does have an effect on the period of oscillations, they are relatively weak compared to the effect of the height of the system on these oscillations. In all cases investigated with different compositions and cooling rates, it was always found that the period increase with increase in sample height.

Nature of oscillations:

In our discussions, we tried to understand the dominating parameter in determining the period of oscillations. Yet in our experiments we found that oscillations had two prominent natures. 1) Interface dominated oscillation and 2) Volume dominated oscillation, both of which will be explained shortly.

We found that in samples with relatively smaller heights, turbidity tends to emerge from the interface of the phases, and then proceed to fill the sample. We call this the interface dominated oscillation. [Fig 7.13] shows the sequential snapshots of a sample of polystyrene/methylcyclohexane mixture, with mass ratio 8:92, at a sample height of 1.8cm. The images span 2 minutes and we see that at first the upper phase is clear. The second image in the series shows turbidity emerging from the interface. The third image shows the progress of turbidity upwards, and the fourth image shows almost the whole upper phase being turbid.
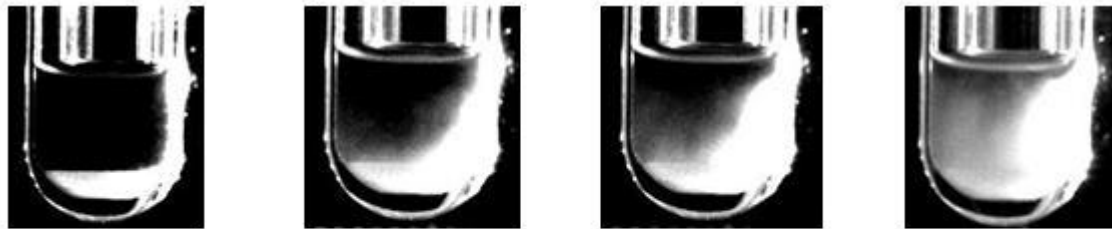
2 mins

.Fig 7.13. Sequential snapshots of PS/methylcyclohexane mixture (8:92 mass ratio), with sample height 1.8cm. First image shows a clear upper phase. Turbidity emerges from the interface in the second image, consequently proceeding upwards in the third image. The whole upper phase being turbid in the fourth image. The decreasing gradient of light from right end to left end of each image is due to the position of the two light sources relative to this sample cell, which are adjusted to give the best contrast possible.

In samples with relatively larger heights, the case is not the same. The turbidity tends to emerge almost uniformly throughout the volume of the sample. We call this the volume dominated oscillation. [Fig 7.14] shows the sequential snapshots of a sample of polystyrene/methylcyclohexane mixture, with mass ratio 8:92, at a sample height of 8.1cm. The images span 2 minutes and we see that at first the upper phase is clear. The second image in the series shows turbidity emerging simultaneously throughout the sample. The turbidity gets stronger as time progresses, shown in third image, and the fourth image shows the maximum turbidity throughout the sample. We see that as time progresses only the intensity of the turbidity gets stronger.
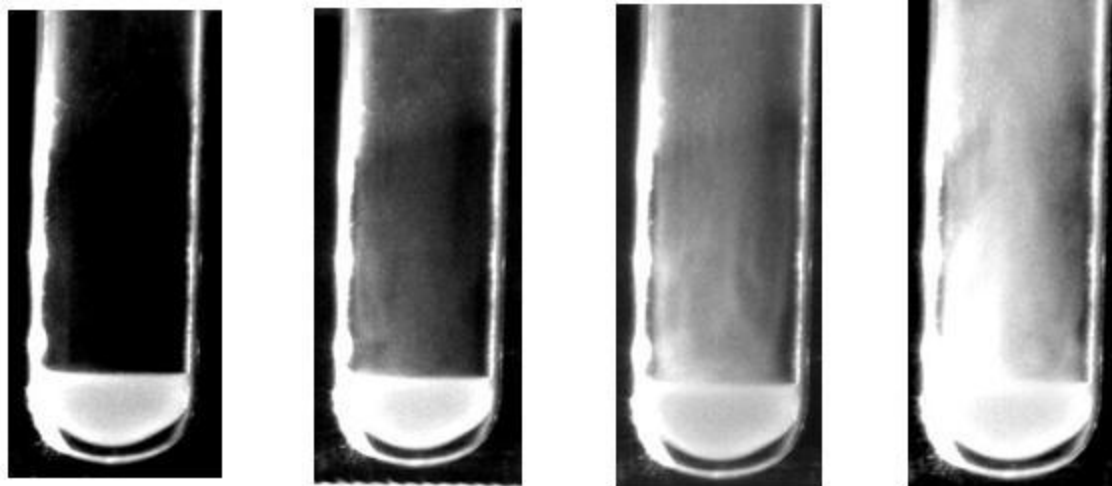
Fig 7.14. Sequential snapshots of PS/methylcyclohexane mixture (8:92 mass ratio), with sample height 8.1 cm. First image shows a clear upper phase. Turbidity emerges homogenously throughout the volume in the second image, consequently getting more intense in the third image. The turbidity reaches its maximum in the fourth image. The decreasing gradient of light from left end to right end of each image is due to the position of the two light sources relative to this sample cell, which are adjusted to give the best possible contrast.

Interface dominated oscillation.

We see that in some cases, mostly with the lower sample heights and lower cooling rates, oscillations start at the interface and the turbidity spreads increasingly upwards in the sample. We suggest that the reason is due to satellite droplets that emerge during the droplet coalescence with the macroscopic interface. During droplet coalescence at the interface, satellite droplets may be generated and transported into the upper phase by advection.

Satellite droplets have been directly observed by Arts et al [57-58] at the gas-liquid interface of a colloid-polymer system. Just before a droplet coalesces with its bulk phase, a thin gas film separates the droplet from its bulk phase. They observe that thermal capillary waves induce a breakup of the gas film and part of the gas phase is trapped in the bulk liquid phase. In this ultralow interfacial tension system, the droplet size and the fluctuations due to capillary waves are of the same order. Deformation and breakup of droplets at interfaces between liquids have been studied intensively [59-60]. In either case, a satellite droplet was pinched off the coalescing droplet. After coalescence of the main droplet, the satellite droplet followed in a coalescence cycle of its own.

Interface induced droplet formation may proceed as shown in [Fig 7.15]. A polystyrene rich droplet approaches the interface to merge with the polystyrene rich lower phase. As it merges at the interface, tiny droplets are formed. These satellite droplets are advected into the upper phase. Thus droplets larger than the critical nuclear size are formed without nucleation and phase separation proceeds via droplet growth rather than via nucleation.
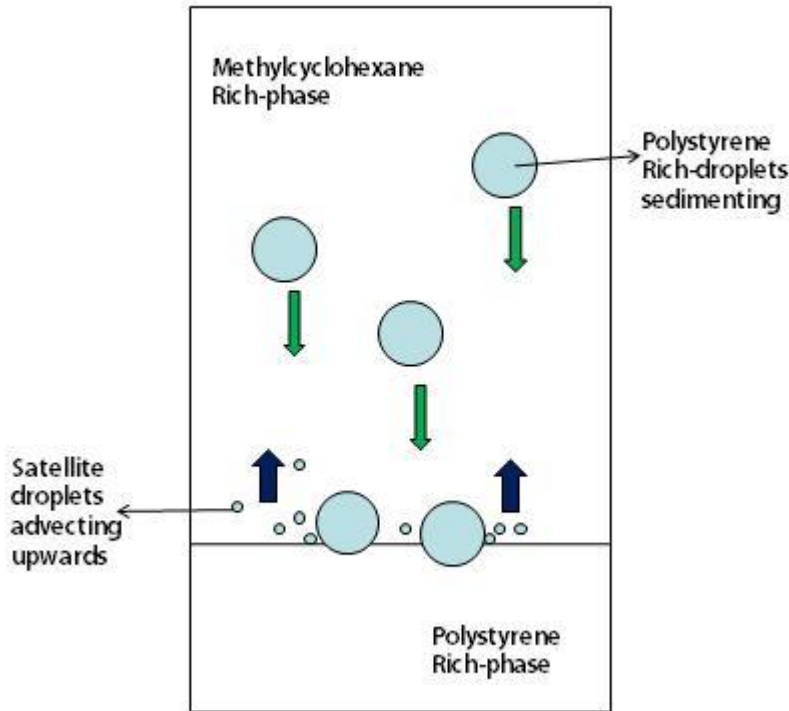

Fig. 7.15

Sketch showing the plausibility of interface dominated oscillations. PS rich droplets sediment and merge with the interface. The merging gives rise to satellite droplets, which are then advected upwards in the methylcyclohexane rich phase. These droplets then grow, coalesce and sediment, avoiding the need to cross the energy barrier for homogenous nucleation.

For an oscillation dominated by the effect of the macroscopic interface, it requires that most droplets are formed at the interface. To effectively reduce supersaturation in the bulk, satellite droplets should be distributed almost homogenously. Hence whether satellite droplets can influence or even determine the period of oscillation depends on the flow velocity of the medium. Two time scales gain importance in determining the nature of oscillations. (a) the time scale on which droplets are advected into the bulk phase, τ_{adv} and (b) the time scale of volume-controlled droplet nucleation and growth, τ_{nuc}.

When phase separation occurs, the droplets follow the flow field and thus act as tracer particles. We see in our experiments that in the relatively smaller sample heights (eg: 1.8cm), there is intense convection inside the fluid. Therefore the time scales associated with the advection of satellite droplets could be much lesser than the time scales needed for nucleation and growth of new droplets, ie, $\tau_{adv} < \tau_{nuc}$. Consequently in this case the satellite droplets are favorably advected upwards, and phase separation continues primarily by the coarsening of these droplets, and their subsequent sedimentation.

To estimate the time scales of advection, we used higher magnification to track individual droplets {Fig 7.16}. The images were taken at the top of the sample.
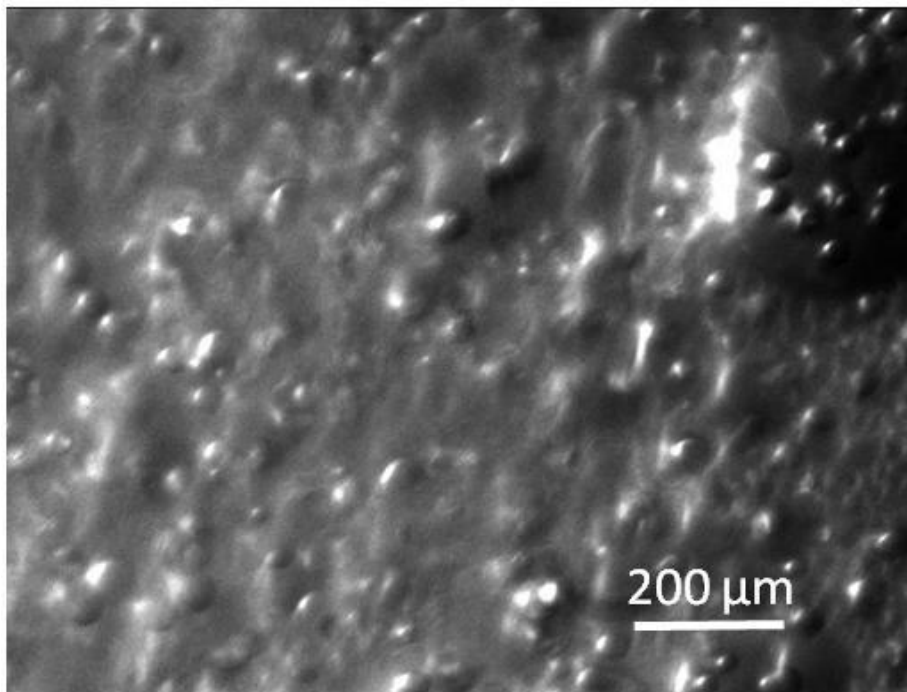
Fig 7.16
Image showing individual droplets at the beginning of an oscillation. Sample: PS(8wt%) mixed with methylcyclohexane. Height: 3.1cm. Cooled at 4K/h. Most droplets are advected upwards, although they do not follow a strictly straight path. Average velocities are calculated by tracking individual droplets.

Images were captured at 5frames/second, and the droplets were tracked and distances measured using ImageProPlus. The following velocity measurements {Fig 7.17} are from 30 droplets of the sample height 3.1 cm cooled at 4K/h, at the beginning of an oscillation.

Fig 7.17

Histoplot showing the velocity distributions of 30 droplets. The distribution peaks around 90μ m/s

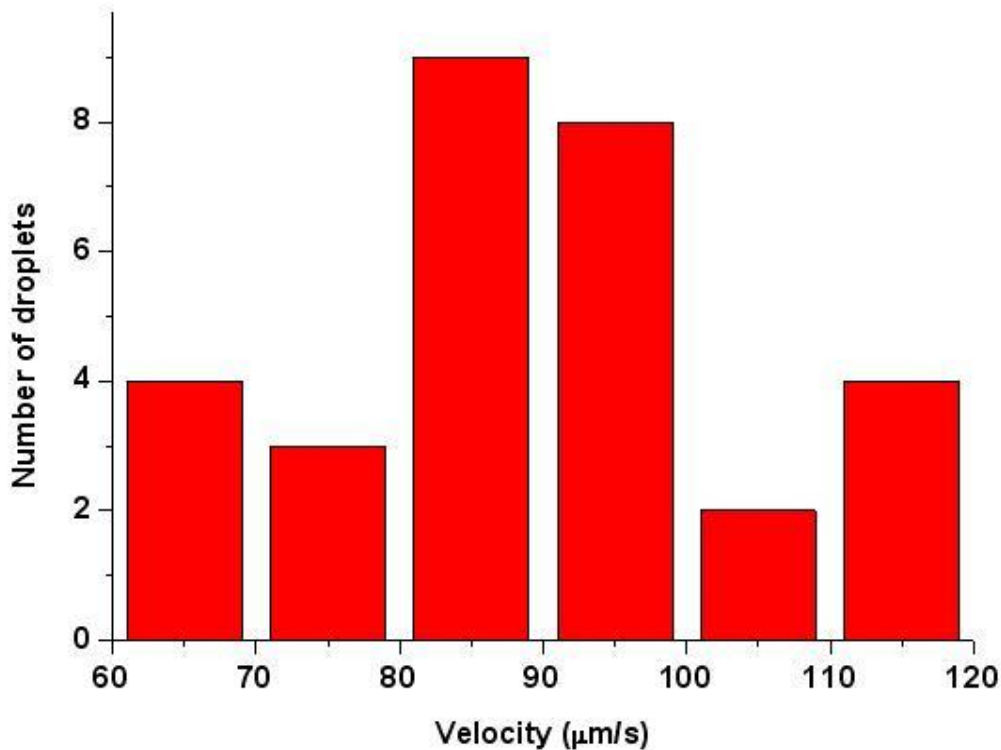Droplet velocity range between 60 and 120μm/s. The droplets did not follow a straight path for a long time, since it was under the convecting fluid. The measurements were made by tracking and measuring the path as long as the droplets followed an approximate straight line.

Taking a mean value of 90μm/s, we can calculate the time needed for the droplets to reach the top of the sample from the interface. For the total sample height of 3.1cm, the distance from the top of the sample to the interface, is 2.4cm. The time for the droplets to reach the top is then approximately 4.4 minutes.

Complimentarily, we can estimate the velocity of the advecting droplets from the low magnification experiments {see Fig 7.18}. The middle sample is the one with height 3.1 cm. We can calculate the time for the advecting "front" to start from the interface and reach the top, at the start of the oscillation. It's not strictly a front, since the convection distorts it and a "smoky" front is resulted as seen from the figure.
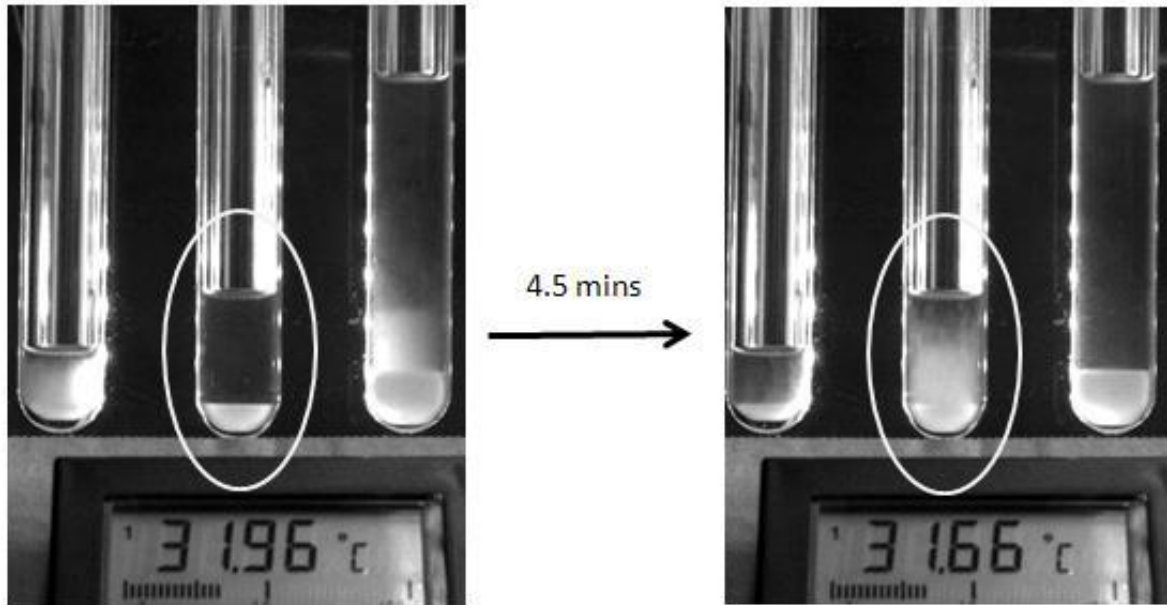
Fig 7.18
*Images taken 4.5mins apart, from an experiment with PS(8wt%) mixed with
methylcyclohexane. The first images shows the middle sample clear in the upper phase.
As the system is cooled, turbidity first appears near the interface and progresses
upwards. The second image shows the advected "smoke" of turbidity just reaching the top
of the sample (sample-air meniscus)*

Images were captured at 30sec interval, and the two images shown above are 9 frames apart.
This low magnification estimate of the velocity gives 4.5 minutes for the droplets to reach the top from the interface, which is in close agreement with the high magnification data.

The following space time plot [Fig 7.19] shows the first few oscillations of the 1.8cm sample cooled at 4K/h. Turbidity appears first near the interface (i) and later at the top (t). The average time difference between the appearance of turbidity at the interface and top is 2.4 (± 0.5) mins. The first clouding, however is homogenous throughout the sample. We will go through a discussion of this case later.
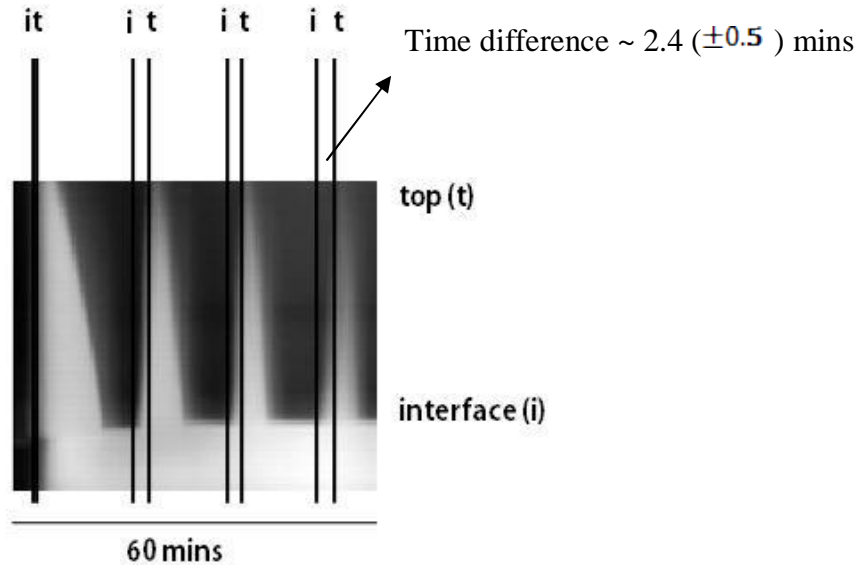
Fig 7.19

*Space-time plot showing the first few oscillations of the smaller
sample (1.8cm high) of PS (8wt%) mixed in methylcyclohexane. It shows
an example of interface dominated oscillation, where the turbidity first appears
at the interface and proceeds upwards. Parallel lines are drawn denoting the
instant at which turbidity appears at the interface (line 'i') and that at the top (line "t").
The average time difference between these instants is 2.4 (± 0.5) mins.*

Volume dominated oscillation:

For the longer sample heights (eg:8.1cm), and at relatively higher cooling rates (8K/h or higher), we see that during an oscillation, the whole sample gets turbid almost homogenously throughout the volume. Here also the droplets coalescing with the macroscopic interface give rise to satellite droplets. But here the droplets need to be advected to comparatively larger heights (~4 times high) to release supersaturation. Consequently the convection must be strong enough for this scenario. This does not seem to be the case in our experiments. We see that the whole sample gets turbid almost homogenously. Therefore the likely scenario is as follows. The sample is cooled down continuously, slowly increasing the supersaturation. The energy barrier for the nucleation of droplets throughout the sample is crossed. New nuclei are formed which then grow and coalesce. The droplets follow gravity and sediment and coalesce with the macroscopic interface. In this case $\tau_{adv} > \tau_{nuc}$.

The following [Fig 7.20] is a space-time plot of sample height 8.3 cm, with PS weight fraction φ_{PS}= 5 wt%, cooled at 8K/h.
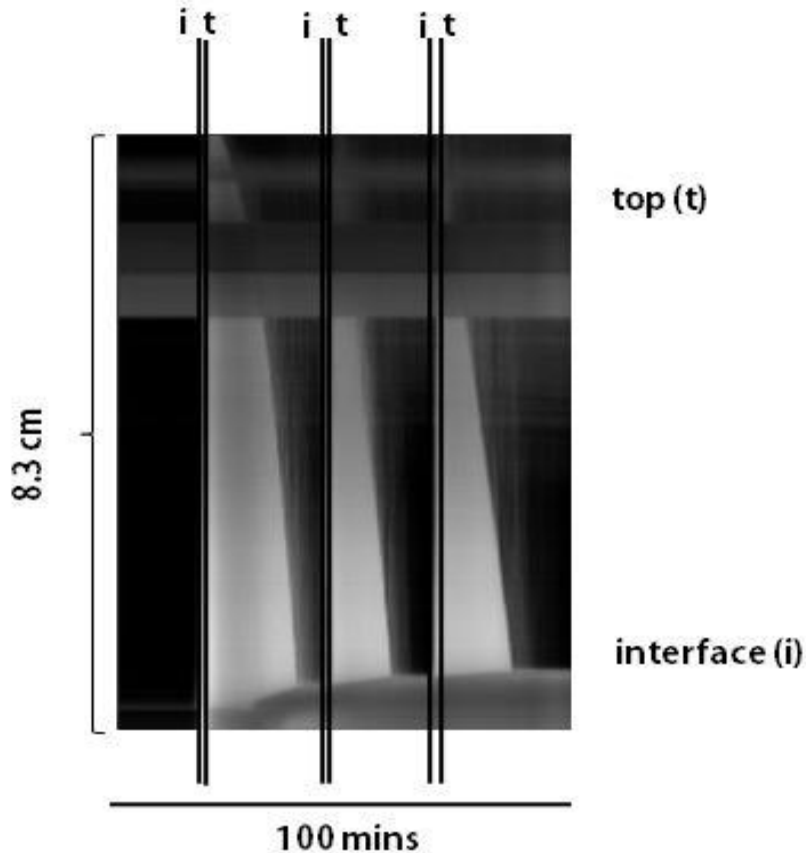
Fig 7.20

Space time plot of the first few oscillations of sample height 8.3cm, with PS weight fraction φ_{PS}= 5 wt%, cooled at 8K/h. Turbidity appears almost simultaneously at the interface and top. The average time difference between the two instants is less than 1min. Assuming the droplets were advected upwards from the interface, its velocity would be in the order of 1mm/s, which contradicts our experimental findings. The case illustrates an example of volume dominated oscillation, where homogenous nucleation, growth and coalescence happens throughout the sample.

We see that turbidity appears almost simultaneously at the interface and the top of the sample. The slight time difference is less than a minute. The turbidity cannot be caused by the droplets advected from the interface. If it were, then the droplets would need a velocity in the order of 1mm/s. But we have seen from that the velocity of the advecting droplets is in the order of 100 μm/s, which is an order of magnitude lesser.

Thus the sample chooses a volume-dominated oscillation or an interface dominated one depending on which mechanism is more favourable. The convection time scales compete with the rate of cooling the sample, which essentially determines the time scale for development of supersaturation and nucleation.

First clouding in the series of oscillations:

In our experiments, we first cool down the sample to approximately 0.5K below the phase transition temperature, and leave it at that constant temperature for 3 hours. As the sample crosses the binodal, all the three samples (which have different sample heights) phase separate simultaneously. The sample gets cleared up during this waiting period, forming a macroscopic interface between the lower polymer rich phase and the upper solvent rich phase. After this waiting time, the samples are cooled by a continuous temperature ramp. We see the first clouding (in the oscillation series, and not the first phase separation) simultaneously in all the samples, as can be seen in [Fig 7.21].

Fig 7.21
Image showing the simulataneous clouding of all the samples. This is the first turbidity in the oscillatory cycle. This is the only case, apart from the initial phase separation, where simultaneous turbidity is observed.

After the waiting time and the subsequent cooling, the droplets are formed which sediment as the time goes on. There is a well defined sedimentation front in all three samples, as shown in Fig 7.22

Fig 7.22
Figure shows well defined sedimentation front in all three samples.

The fact that there is a well defined sedimentation front hints that gravity is the dominant factor here. The convection seems not to be strong inside any of the three samples. This can be understood as follows. The system had been maintained at a constant temperature during the waiting time. Due to this thermal equilibrium between the sample and the water bath, there would be very little convection inside the sample. The sample thus is almost stationary. Once the continuous cooling starts after this waiting period, supersaturation develops with the temperature ramp, and the samples nucleate homogenously. The fact that all the three samples become turbid at the same temperature for the first oscillation can be understood as follows. Once the system is given sufficient waiting time after the initial phase separation, the equilibrium compositions of both phases would be reached in all three samples. The upper and lower phases of all the samples would therefore be identical. Only the absolute volumes would be the distinguishing factor between the three samples. Since all other parameters would remain constant, a change in the free energy of the system would be achieved only through a change in the temperature. Our water bath is maintained within a temperature homogeneity of 10 to 20 millikelvins. Therefore as the systems are cooled down together, we should expect a definite temperature at which sufficient supersaturation for nucleation is achieved in all three samples irrespective of their heights. In fact this is precisely what we observe in our experiments.

The first clouding in the oscillation series is special and different from the latter turbidities in the following way. Since we give enough time for the droplets during the first phase separation to sediment, there would not be sufficient droplets to create satellite droplets at the interface, at the start of this first oscillation. Therefore we should expect homogenous nucleation in all the samples, irrespective of their heights. This exclusive

homogenous nucleation in all samples makes the first clouding different from the rest. This also further supports the case of interface dominated oscillations exhibited in smaller samples, and relatively slower cooling rates, in the latter oscillations.

Sedimentation time, the determining factor for the period.

We saw that the period of oscillations primarily depended on the height of the sample, except for the first clouding where all samples become turbid simultaneously. We suggest that the difference in the periods at different heights is primarily due to the different time intervals that the droplets take to sediment. Assuming that the droplets are formed throughout the sample, the time they take to sediment would depend on the height of the sample. Therefore the shortest sample would clear off the turbidity first, the medium sample a bit later and the tallest sample taking the highest time. [Fig 7.23] shows the case where the lowest sample has its droplets sedimented, while the other two samples are still in its process of sedimentation.

Fig 7.23
Image showing sedimentation of droplets in the three samples. The first sample (1.8cm) has already finished with its sedimentation, while the sedimenting front can be seen for the other two samples (3.1cm and 8.1 cm). It can be understood that the sedimentation time increases with sample height.

We can estimate the sedimentation velocity of the droplets by measuring the velocity of the sedimenting front. The following graph [Fig 7.24] gives the front sedimentation

velocities of PS/methylcyclohexane (8:92 mass ratio) cooled at 4K/h, for the first clouding. The velocities are shown as the distance moved by the front per 90 seconds, since images were taken at an interval of 1.5mins. The initial time t=0 is defined as the time when all the samples are turbid homogenously. The front is then defined by the turbid line coinciding with sample-air meniscus.

Fig 7.24
Graph showing the front sedimentation velocities of PS/methylcyclohexane (8:92 mass ratio) cooled at 4K/h, for the first clouding in the three sample heights: 1.8cm, 3.1cm, 8.1cm. Velocities are shown as the distance moved by the front per 90 seconds, since images were taken at an interval of 1.5mins. The initial time t=0 is defined as the time when all the samples are turbid homogenously. The front is then defined by the turbid line coinciding with sample-air meniscus.
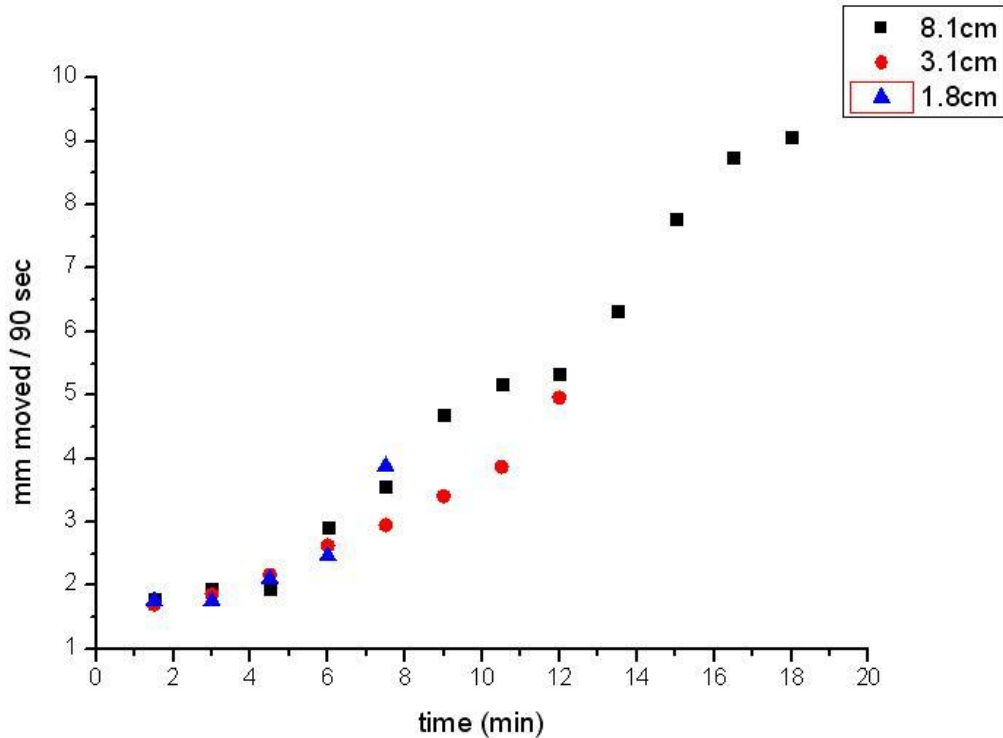
The triangles represent the sedimenting front velocities of the smallest sample (1.8cm), the circles that of 3.1cm and squares that of 8.1cm sample. We see that the smallest sample completes its sedimentation in approximately 8 minutes. The 3.1 cm sample takes about 12 minutes to sediment and the 8.1cm sample takes 20 minutes to sediment.

We also see that the sedimenting front does not hold a constant velocity, but rather accelerates in all three cases.

We also looked at higher magnification to track individual droplets, to measure their sedimenting velocities. The following histogram [Fig 7.25] shows the measured

velocities for 30 droplets, sedimenting during their first clouding in sample height of 3.1cm, cooled at 4K/h. The images were taken near the top of the sample, during the first minutes of appearance of turbidity.
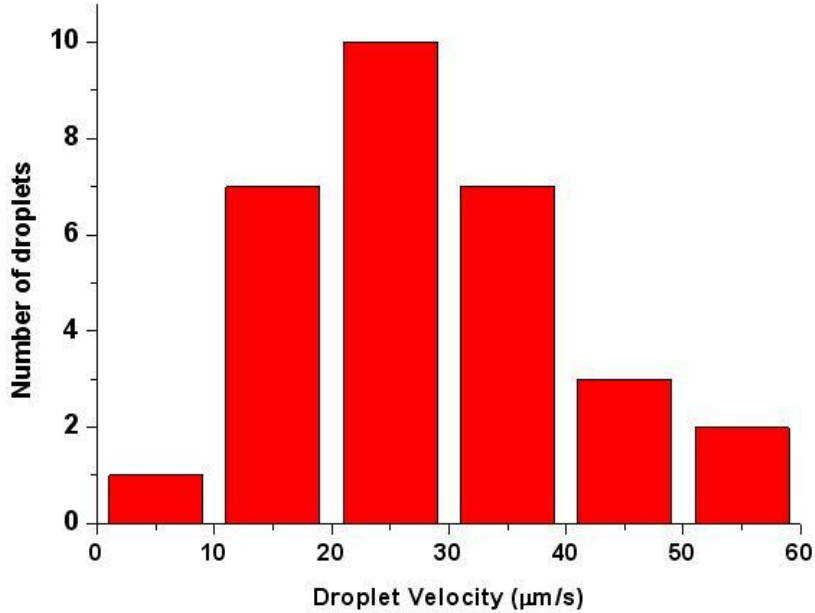

Fig 7.25
Histogram showing the velocity distribution of 30 droplets. The distribution peaks around 25µm/s.

Droplet velocities range from 15 to 60µm/s. The velocity peaks around a value of 25µm/s. This value is equal to 2.2mm/90sec. Comparing it with the values of sedimenting front velocity {Fig: 7.24}, we find that it is in the initial stage of sedimentation.

Since the shortest sample first clears off the droplets, it waits for supersaturation to develop to create further droplets. The continuous temperature ramp pushes the system towards supersaturation. During this period the sample remains clear. As soon as the sufficient supersaturation is achieved the shortest sample nucleates again and the phase separation continues through droplet growth and sedimentation. The cycle continues.

But for the higher samples, the system first needs to be cleared off the droplets to induce supersaturation. Therefore nucleation is not initiated until the droplets from the previous oscillation have been sedimented and cleared off the sample. Thus it follows that the second oscillation would be occurring first in the smallest sample, then in the medium sample and last in the highest sample. This is what we observe in our experiments. The next cycle of turbidity would also follow the same procedure. Therefore the time between two turbid periods would be the shortest in the shortest sample and the

longest in the longest sample. Sedimentation time thus determines the period of the system. [Fig 7.26] shows schematically this explanation.
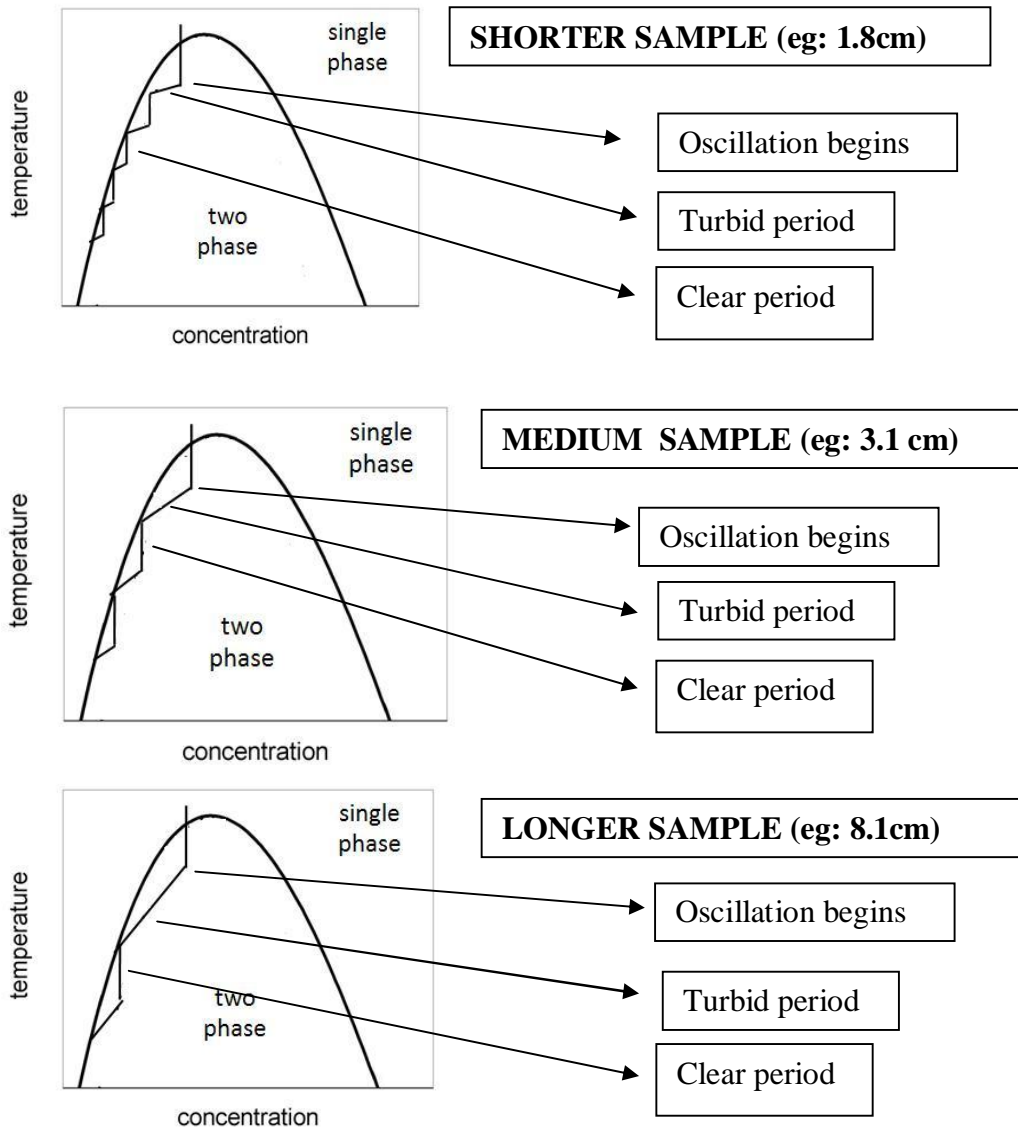
Fig 7.26.

All three samples are cooled simulataneously below the binodal. Nucleation occurs, and the sample tries to attain equilibrium concentration at any given temperature, given by the phase boundary. The lines which have slopes represent the turbid period, where the sample clears off the droplets by sedimentation. The smaller cell is represented by the smaller slopes, as it takes relatively less time for the droplets to sediment and reach equilibrium concentration. The cooling proceeds, and the vertical line represents the period when the sample is clear of turbidity. The cycle continues with the next nucleation and the subsequent sedimentation of the droplets. The larger sample is reperesented by a larger slope of the line denoting the turbid period, as it takes longer times to sediment in this sample.

The above case is described assuming that gravity is the only force affecting the motion of droplets. This is not the actual case though. We have already seen that convection is present in the samples. Thus there is a competition between the effects of convection and gravity. Assuming gravity to be dominant force when sedimentation occurs, the oscillation periods should scale with the sample height. This can be understood as follows. Assuming the droplets sediment with a constant terminal velocity through the sample, the time to sediment should then scale linearly with the height. Once the samples are cleared by sedimentation, the clear period should be of equal time for all samples irrespective of the height. The period then depends only on the turbid time. Thus the period should ideally scale with the height. But in reality this is not strictly the case. We saw that the sedimentation front does not have a constant velocity, but rather accelerates. This is because of the following. The size of the droplets does not remain a constant. As phase separation proceeds, the droplets collect material and grow and therefore they gradually increase their sedimentation velocities. Also, with every oscillation, the relative densities of the mixture changes, and so the sedimentation velocity would be slightly different with each oscillation.

Although convection does not strongly affect the sedimentation time, it influences the oscillation period through its effect on the advection of satellite droplets. Since satellite droplets are formed during coalescence of droplets at the interface, they reduce the energy barrier for phase separation to occur. They eliminate the need for nucleation of droplets through supersaturation. In smaller height systems, where they are capable of being advected almost homogenously throughout the sample, phase separation starts earlier than if it would have required nucleation. The following figure, [Fig 7.27], shows the scenario, how satellite droplets and convection affect the period.
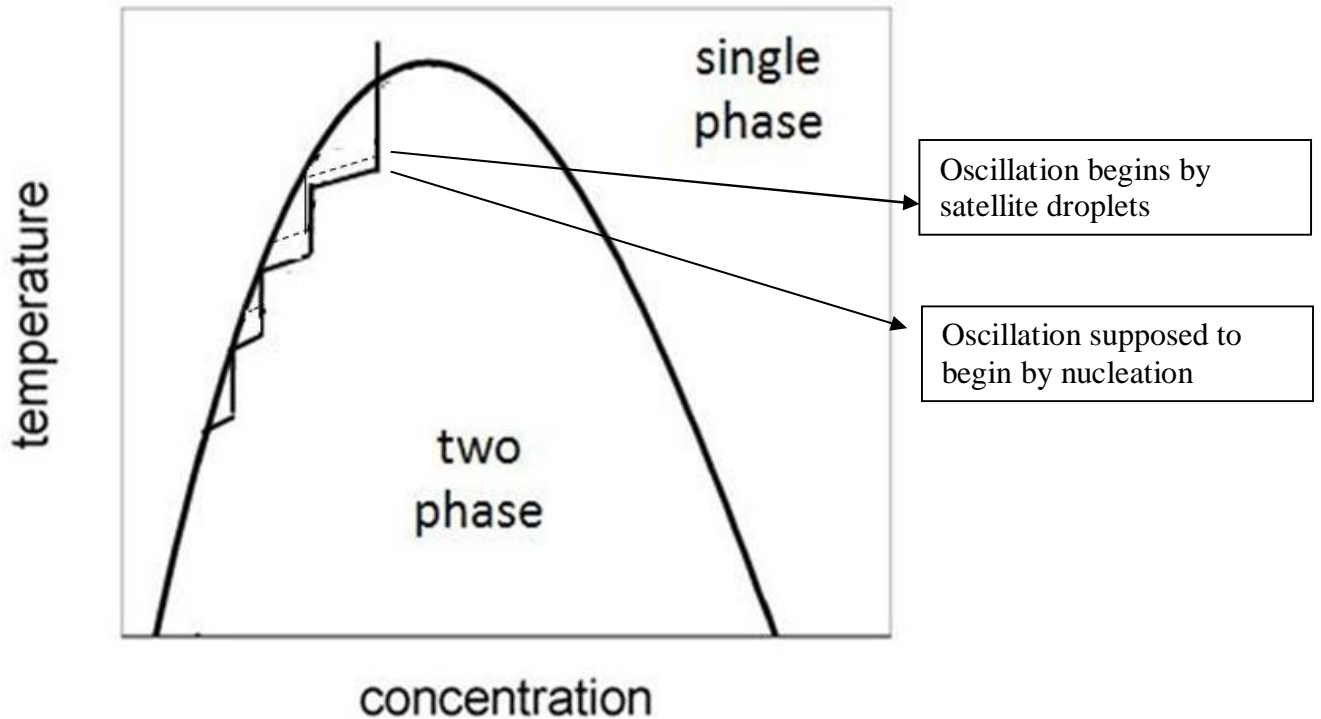
Fig 7.27.
Sketch describing the difference between oscillations generated by satellite droplets and that by nucleation. The dashed lines depict the case of oscillations initiated by satellite droplets. The clear lines depict the oscillations that would occur in the case of no satellite droplets present in the system. Phase separation would then proceed by nucleation, when the temperature is sufficient for creating supersaturation. The convection of satellite droplets from the interface upwards eliminates the necessity of nucleation, and phase separation can proceed through the growth and sedimentation. The energy barrier would be then lesser than that for nucleation.

Can oscillations be suppressed?

From the discussion we have yet had, it seems that a binary mixture undergoing phase separation by continuous temperature ramp must necessarily exhibit oscillations. Although phase separation can proceed through periodic nucleation or through the growth of satellite droplets, it seems inevitable that the process must have periods of turbidity and periods when the sample is clear. Does a possibility exist where phase separation can proceed without oscillations and yet exchange material between the two phases?

113

The following are space time plots [Fig 7.28] observed for a mixture of PS+methylcyclohexane (mass ratio 5:95), for 3 sample heights 2.2cm, 3.2cm and 8.3cm, and continuously cooled at 4K/h.
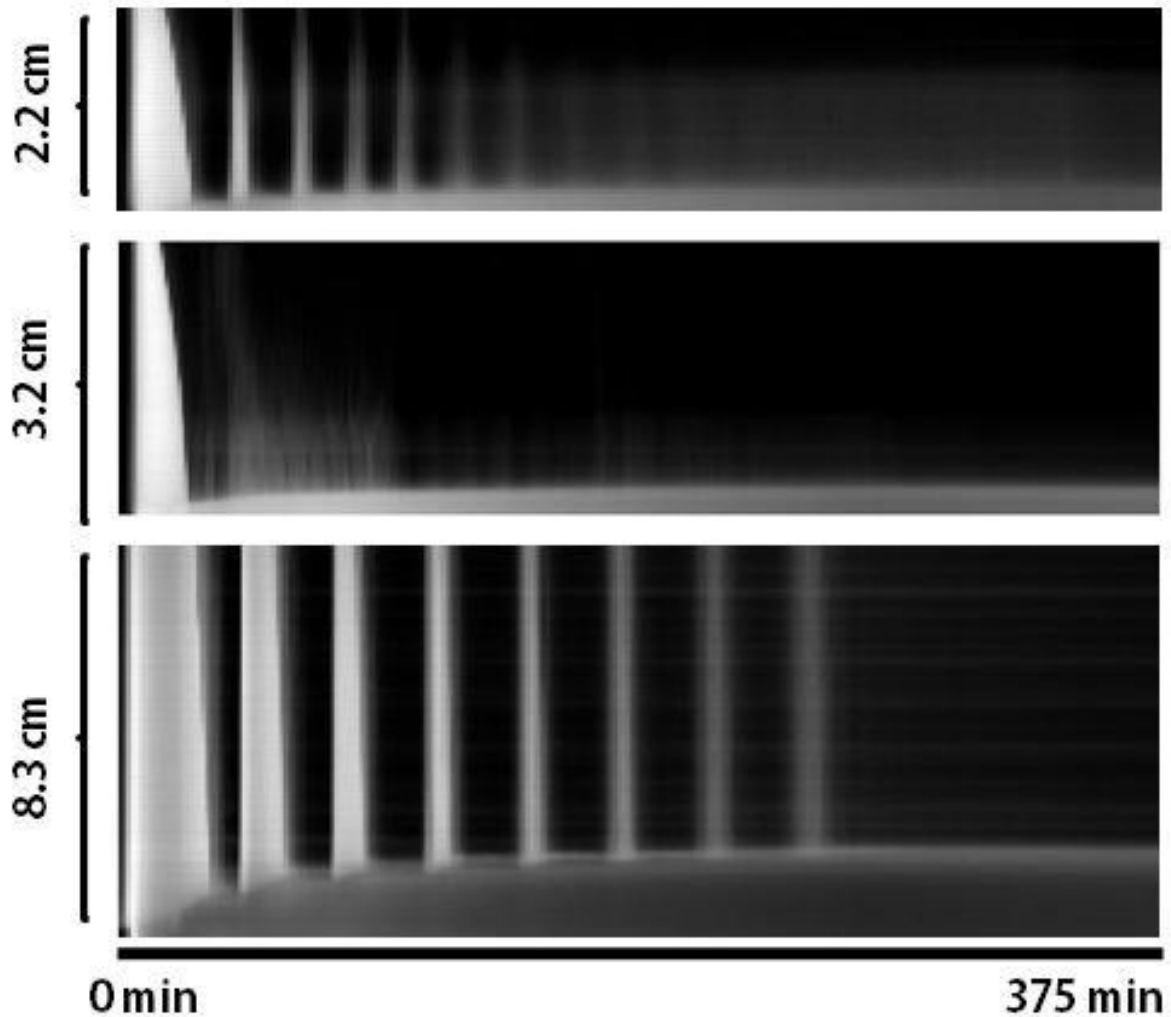
Fig 7.28
Space-time plots of three samples of PS(5%wt) mixed with methylcyclohexane in heights of 2.2cm, 3.2cm, 8.3cm. The system is cooled at 4K/h. Both the 2.2cm sample and the 8.3cm sample oscillate, but oscillations vanish in the 3.2cm cell. Only a faint continuous turbidity can be seen in this sample.

We see that although the smaller sample (2.2cm) and the large sample (8.3cm) have well defined periods of oscillation, the medium sample (3.2cm) does not show any definite signs of oscillation. There is turbidity, which in fact is necessary, signifying material exchange between the two phases, but no well defined behavior of oscillations is observed. This indeed is a special case.

We can understand the phenomenon exhibited by the medium sample as follows. The first oscillation is well defined in this sample and it is represented by a the very

114

bright area at the beginning of the space time plot. Thereafter two mechanisms operate on this system. Firstly, there is satellite droplets formed at the interface which are convected upwards. Secondly, the temperature of the sample is continuously varying, which in turn is changing the free energy of a system. Normally, if the convection is strong enough to make the system proceed with its phase separation by droplet growth, then it does so. Thereafter the system becomes clear after these droplets sediment. In general there is a silent period until the temperature ramp has reached sufficient value so as to cross the energy barrier either for volume dominated nucleation or growth of the next batch of satellite droplets. In the special case where the temperature difference (and therefore, time difference) is infinitesimally small between sedimentation of droplets and the growth of the next batch of satellite droplets, a silent period would become virtually absent. A constant turbidity would be observed in the sample, where sedimentation of grown droplets and the growth of new droplets take place simultaneously. In this special case, oscillations would vanish. The following figure, [Fig 7.29], demonstrates the pathway of such a phase separation.
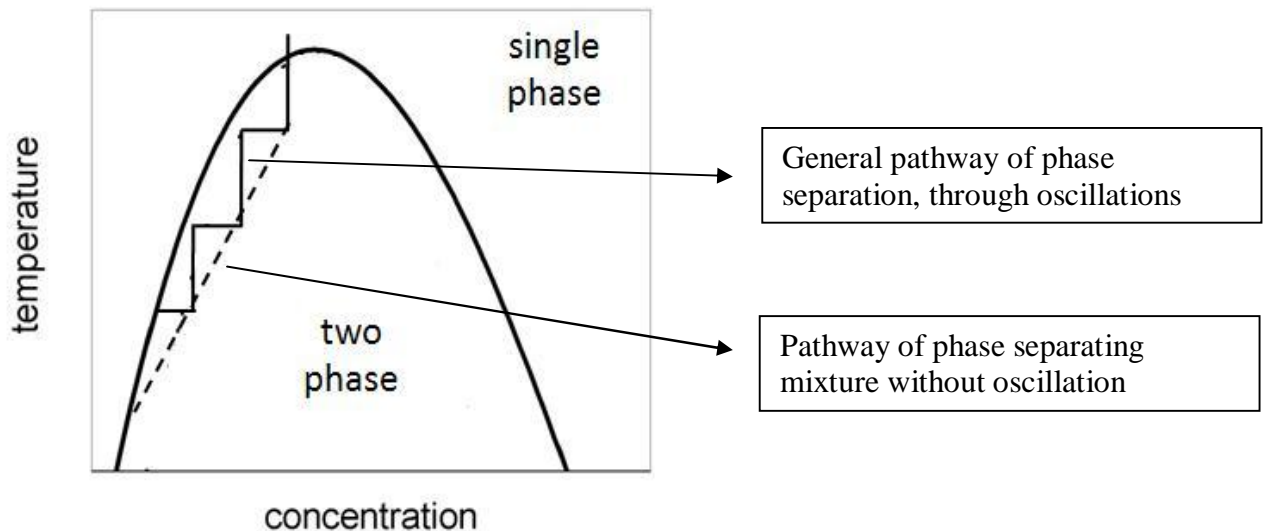
Fig 7.29.

Sketch showing the case of oscillation suppression. The solid lines show the general case of phase separation in a continuously cooled binary mixture, where well defined periods of turbidity are separated by periods when the sample is clear. The edges represent the start of an oscillation. Assuming fast sedimentation, the solid lines are drawn horizontally with no slope, for the sake of clarity. The dashed line shows the special case where satellite droplets are formed, convected throughout the sample, and they grow, and sediment. But as they sediment, the time scale of temperature ramp is such that it reaches sufficient energy barrier for the new batch of satellite droplets to be advected and grown. The process thus continues, keeping the sample continuously turbid without allowing the sample to have periods of clarity.

SUMMARY

This work focused mainly on two aspects of kinetics of phase separation in binary mixtures. In the first part, we studied the interplay of hydrodynamics and the phase separation of binary mixtures. A considerably flat container (a laterally extended geometry), at an aspect ratio of 14:1 (diameter: height) was chosen, so that any hydrodynamic instabilities, if they arise, could be tracked. Two binary mixtures were studied. One was a mixture of methanol and hexane, doped with 5% ethanol, which phase separated under cooling. The second was a mixture of butoxyethanol and water, doped with 2% decane, which phase separated under heating. The dopants were added to bring down the phase transition temperature around room temperature.

Although much work has been done already on classical hydrodynamic instabilities, not much has been done in the understanding of the coupling between phase separation and hydrodynamic instabilities. This work aimed at understanding the influence of phase separation in initiating any hydrodynamic instability, and also vice versa. Another aim was to understand the influence of the applied temperature protocol on the emergence of patterns characteristic to hydrodynamic instabilities.

On slowly cooling the system continuously, at specific cooling rates, patterns were observed in the first mixture, at the start of phase separation. They resembled the patterns observed in classical Rayleigh-Bénard instability, which arises when a liquid continuously is heated from below. To suppress this classical convection, the cooling setup was tuned such that the lower side of the sample always remained cooler by a few millikelvins, relative to the top. We found that the nature of patterns changed with different cooling rates, with stable patterns appearing for a specific cooling rate (1K/h). On the basis of the cooling protocol, we estimated a modified Rayleigh number for our system. We found that the estimated modified Rayleigh number is near the critical value for instability, for cooling rates between 0.5K/h and 1K/h. This is consistent with our experimental findings.

The origin of the patterns, in spite of the lower side being relatively colder with respect to the top, points to two possible reasons. 1) During phase separation droplets of either phases are formed, which releases a latent heat. Our microcalorimetry measurements show that the rise in temperature during the first phase separation is in the order of 10-20millikelvins, which in some cases is enough to reverse the applied temperature bias. Thus phase separation in itself initiates a hydrodynamic instability. 2) The second reason comes from the cooling protocol itself. The sample was cooled from above and below. At sufficiently high cooling rates, there are situations where the interior of the sample is relatively hotter than both top and bottom of the sample. This is sufficient to create an instability within the cell. Our experiments at higher cooling rates (5K/h and above) show complex patterns, which hints that there is enough convection even before phase separation occurs. Infact, theoretical work done by Dr.Hayase show that patterns could arise in a system without latent heat, with symmetrical cooling from top and bottom. The simulations also show that the patterns do not span the entire height

of the sample cell. This is again consistent with the cell sizes measured in our experiment.

The second mixture also showed patterns at specific heating rates, when it was continuously heated inducing phase separation. In this case though, the sample was turbid for a long time until patterns appeared. A meniscus was most probably formed before the patterns emerged. We attribute the reason of patterns in this case to Marangoni convection, which is present in systems with an interface, where local differences in surface tension give rise to an instability. Our estimates for the Rayleigh number also show a significantly lower number than that's required for RB-type instability.

In the first part of the work, therefore, we identify two different kinds of hydrodynamic instabilities in two different mixtures. Both are observed during, or after the first phase separation. Our patterns compare with the classical convection patterns, but here the origins are from phase separation and the cooling protocol.

In the second part of the work, we focused on the kinetics of phase separation in a polymer solution (polystyrene and methylcyclohexane), which is cooled continuously far down into the two phase region. Oscillations in turbidity, denoting material exchange between the phases are seen. Three processes contribute to the phase separation: Nucleation of droplets, their growth and coalescence, and their subsequent sedimentation. Experiments in low molecular binary mixtures had led to models of oscillation [43] which considered sedimentation time scales much faster than the time scales of nucleation and growth. The size and shape of the sample therefore did not matter in such situations. The oscillations in turbidity were volume-dominated. The present work aimed at understanding the influence of sedimentation time scales for polymer mixtures. Three heights of the sample with same composition were studied side by side. We found that periods increased with the sample height, thus showing that sedimentation time determines the period of oscillations in the polymer solutions. We experimented with different cooling rates and different compositions of the mixture, and we found that periods are still determined by the sample height, and therefore by sedimentation time.

We also see that turbidity emerges in two ways; either from the interface, or throughout the sample. We suggest that oscillations starting from the interface are due to satellite droplets that are formed on droplet coalescence at the interface. These satellite droplets are then advected to the top of the sample, and they grow, coalesce and sediment. This type of an oscillation wouldn't require the system to pass the energy barrier required for homogenous nucleation throughout the sample. This mechanism would work best in sample where the droplets could be effectively advected throughout the sample. In our experiments, we see more interface dominated oscillations in the smaller cells and lower cooling rates, where droplet advection is favourable. In larger samples and higher cooling rates, we mostly see that the whole sample becomes turbid homogenously, which requires the system to pass the energy barrier for homogenous nucleation.

Oscillations, in principle, occur since the system needs to pass an energy barrier for nucleation. The height of the barrier decreases with increasing supersaturation, which in turn is from the temperature ramp applied. This gives rise to a period where the system is clear, in between the turbid periods. At certain specific cooling rates, the system can follow a path such that the start of a turbid period coincides with the vanishing of the last turbid period, thus eliminating the clear periods. This means suppressions of oscillations altogether. In fact we experimentally present a case where, at a certain cooling rate, oscillations indeed vanish.

Thus we find through this work that the kinetics of phase separation in polymer solution is different from that of a low molecular system; sedimentation time scales become relevant, and therefore so does the shape and size of the sample. The role of interface in initiating turbid periods also become much more prominent in this system compared to that in low molecular mixtures.

In summary, some fundamental properties in the kinetics of phase separation in binary mixtures were studied. While the first part of the work described the close interplay of the first phase separation with hydrodynamic instabilities, the second part investigated the nature and determining factors of oscillations, when the system was cooled deep into the two phase region. Both cases show how the geometry of the cell can affect the kinetics of phase separation. This study leads to further fundamental understandings of the factors contributing to the kinetics of phase separation, and to the understandings of what can be controlled and tuned in practical cases.

REFERENCES

1. Gibbs, J.W., *Scientific Papers.* Scientific Papers. 1961, New York: Dover.
2. Atkins, P.W., de Paula, J., *Physical Chemistry.* 8 ed. Chapter 6. Vol. Chapter 6. 2006: Oxford University Press.
3. Hayase, Y., Kobayashi, M., Vollmer, D., Pleiner, H., Auernhammer, G. K., *Asymmetric oscillations during phase separation under continuous cooling: A simple model.* Journal of Chemical Physics, 2008. **129**(184109).
4. Vollmer, D., Vollmer, J., Wagner, A. J., *Oscillatory kinetics of phase separation in a binary mixture under constant heating.* PCCP, 2002. **4**: p. 1380-1385.
5. Cahn, J.W., *Theory of crystal growth and interface motion in crystalline materials.* Acta Met., 1960. **8**: p. 554.
6. Cahn, J.W., *On spinodal decomposition.* Acta Met., 1961. **9**: p. 795.
7. Cahn, J.W., *Coherent fluctuations and nucleation in isotropic solids.* Acta Met., 1962. **10**: p. 907.
8. Cahn, J.W., Hillig, W.B. and Sears, G.W., *The molecular mechanism of solidification.* Acta Met., 1964. **12**: p. 1421.
9. Hilliard, J.E.a.C., J.W., *On the Nature of the Interface Between a Solid Metal and Its Melt.* Acta Met., 1958. **6**: p. 772.
10. Hilliard, J.E., *Spinodal Decomposition, in Phase Transformations.* American Society of Metals, Metals Park,, 1970: p. 497.
11. Abraham, F.F., *Homogeneous nucleation theory.* 1974, New York: Academic Press.
12. Anisimov, M.P., *Nucleation: theory and experiment.* Russian Chemical Reviews, 2003. **72(7)**: p. 591-600.
13. Schmelzer, J.E., Fokin, Yuritsyn, Zanotto, *Nucleation Theory and Applications. Nucleation and Crystallization Kinetics in Silicate Glasses: Theory and Experiment.* 2005: Wiley-VCH Verlag GmbH & Co.
14. Auer, S. and D. Frenkel, Nature, 2001. **409**(1020).
15. Binder, K., J.Non Equilibr. Thermodynamics, 1998. **23**(1).
16. Chaikin, P.M. and T.C. Lubensky, *Principles of Condensed Matter Physics.* 2000, Cambridge: Cambridge University Press.
17. Palmans, R., Frank, A. J., J. Phys. Chem, 1991. **95**: p. 9438.
18. Rajh, T., Micic, O.I., Nozik, A. J., J. Phys. Chem, 1993. **97**: p. 11999.
19. Chou, Y. and W. Goldburg, Phys. Rev. A
1981. **23**: p. 858.
20. Knobler, N.-C.W.a.C.M., Phys. Rev. A, 1981(24): p. 3205.
21. Binder, K., Advances in Polymer Science, 1994. **112**: p. 181.
22. deGennes, P.G., *Scaling Concepts in Polymer Physics.* 1979, New York: Cornell University Press, Ithaca.

23.   Bansil, R., *Phase separation in polymer solutions and gels.* Journal de Physique IV, 1993. **3**: p. 225-235.

24.   Bray, A.J., Adv.Phys, 1994. **43**(357).

25.   Gunton, J.D., M. San Miguel, and P. Sahni, *Phase Transitions and Critical Phenomena*, ed. C. Domb and J.L. Lebowitz. Vol. 8. 1983, New York: Academic Press.

26.   Hohenberg, P.C. and B.I. Halperin, Rev.Mod.Phys, 1975. **49**(435).

27.   Tanaka, H., *Viscoelastic phase separation.* J.Phys: Condens. Matter, 2000. **12**: p. R207 - R264.

28.   Tanaka, H., Macromolecules, 1992. **25**.

29.   Tanaka, H., Phys. Rev. Lett., 1993. **71**.

30.   Tanaka, H. and T. Miura, Phys. Rev. Lett., 1993. **71**: p. 2244.

31.   Chandrasekhar, S., *Hydrodynamic and Hydromagnetic Stability.* 1981, New York: Dover Publications.

32.   Rayleigh, *On convective currents in a horizontal layer of fluid when the higher temperature is on the under side.* Phil. Mag., 1916. **32**: p. 529 - 546.

33.   Guyon, E., et al., *Physical Hydrodynamics.* 2001: Oxford University Press.

34.   Rapaport, D.C., *Hexagonal convection patterns in atomistically stimulated fields.* Phys. Rev. E., 2006. **73**(025301(R)): p. 1-4.

35.   Scriven, L.E., Sternling, C. V., *The Marangoni effects.* Nature, 1960. **187**: p. 186-188.

36.   Kahlweit, M., R. Strey, and G. Busse, *Weakly to strongly structured mixtures.* Phys. Rev. E., 1993. **47**(4197).

37.   Sam, E.M., et al., *Pattern formation in phase separating binary mixtures.* To be published... 2010.

38.   Landoldt-Boernstein.

39.   Yaws, C.L., *Chemical Properties Handbook.* 1999: McGraw-Hill.

40.   Hayase, Y., et al., *Cooling instability with latent heat effect.* to be published... 2010.

41.   Kendon, V.M., et al., *Inertial defects in three-dimensional spinodal decomposition of a symmetric binary fluid mixture: a lattice Boltzmann study.* J. Fluid Mech., 2001. **440**: p. 147 - 203.

42.   Puri, S., Physica A, 1996. **224**(101).

43.   Vollmer, J., G.K. Auernhammer, D. Vollmer, *Minimal Model for Phase Separation under Slow Cooling.* Phys. Rev. Lett., 2007. **98**(115701).

44.   Onuki, A., *Phase Transition Dynamics.* 2002, Cambridge: Cambridge University Press.

45.   Lifshitz, I. and V. Slyozov, J. Phys. Chem. Solids, 1961. **19**(1 - 2): p. 35.

46.   Glauber, R.J., J. Math. Phys. (NY), 1963. **4**(2): p. 294.

47.   Suzuki, M. and R. Kubo, J. Phys. Soc. Jpn., 1968. **24**(1): p. 51.

48.   Siggia, E.D., Phys. Rev. A, 1979. **20**(2): p. 595.

49.   Langer, J., Rev. Mod. Phys., 1980. **52**(1 - 28): p. 1.

50.   Doremus, R., *Rates of Phase Transformations.* 1985, New York: Academic Press.

51.   Metiu, H., K. Kitahara, and J. Ross, *Fluctuation Phenomena*, ed. W. Montroll and J. Lebowitz. 1987, Amsterdam: North Holland.

52. Auernhammer, G.K., Vollmer, D., *Oscillatory instabilities in phase separation of binary mixtures: Fixing the thermodynamic driving.* Journal of Chemical Physics, 2005. **123**(134511).

53. Cates, M.E., Vollmer, J., Wagner, A., Vollmer, D., *Phase separation in binary fluid mixtures with continuously ramped temperature.* Phil. Trans. R. Soc. Lond. A, 2003. **361**: p. 793-807.

54. Vollmer, D., R. Strey, and J. Vollmer, J. Chem. Phys, 1997. **107**(3619).

55. Vollmer, J., D. Vollmer, and R. Strey, J. Chem. Phys, 1997. **107**(3627).

56. Vollmer, J. and D. Vollmer, *Cascade nucleation in the phase separation of amphiphlic mixtures.* Faraday Discussions, 1999. **112**(51).

57. Aarts, D.G.A.L. and H.N.W. Lekkerkerker, *Droplet coalescence: drainage, film rupture and neck growth in ultralow interfacial tension systems.* J. Fluid Mech., 2008. **606**(275).

58. Aarts, D.G.A.L., S. M., and H.N.W. Lekkerkerker, *Direct visual observation of thermal capillary waves.* Science, 2004. **304**(847).

59. Zhang, F.H. and S.T. Thoroddsen, *Satellite generation during bubble coalescence.* Physics of Fluids, 2008. **20**(2).

60. Charles, G.E. and S.G. Mason, *The coalescence of liquid drops with flat liquid/liquid interfaces.* J. Coll. Interf. Sci. , 1960. **15**: p. 105 - 122.

" 'Tis not too late to seek a newer world.
Push off, and sitting well in order smite
The sounding furrows; for my purpose holds
To sail beyond the sunset, and the baths
Of all the western stars, until I die.
It may be that the gulfs will wash us down:
It may be we shall touch the Happy Isles,
And see the great Achilles, whom we knew.
Tho' much is taken, much abides; and tho'
We are not now that strength which in old days
Moved earth and heaven, that which we are, we are;
One equal temper of heroic hearts,
Made weak by time and fate, but strong in will
To strive, to seek, to find, and not to yield."

from "Ulysses"
by Alfred Lord Tennyson